DESIGN AND EXPERIMENTAL EVALUATION OF A DYNAMIC THERMAL DISTORTION GENERATOR FOR TURBOMACHINERY RESEARCH

by

Anthony Louis DiPietro Jr.

Thesis submitted to the Graduate Faculty of the

Virginia Polytechnic Institute and State University

in partial fulfillment of the requirements for the degree of

MASTER OF SCIENCE

in

Aerospace Engineering

APPROVED:

W.F.O'Brien, Jr. Co-Chairman

C.L. Yates Co-Chairman

B. Grossman

April, 1993

Blacksburg, Virginia

DESIGN AND EXPERIMENTAL EVALUATION OF A DYNAMIC THERMAL DISTORTION GENERATOR FOR TURBOMACHINERY RESEARCH

by

Anthony L. DiPietro Jr.

(ABSTRACT)

This thesis involves the design and experimental evaluation of a dynamic thermal distortion generator for turbomachinery research. The detailed design of a thermal distortion generator, its individual components, and its associated hardware was performed. Details of the preliminary design concepts and also the combustion test cell are discussed. Instruments and controls were developed and installed to regulate the distortion generator's operation and to obtain data. The complete geometry of the thermal distortion generator and the layout of the combustion test cell was established. Operating and safety procedures were also established.

A set of experiments was conducted to confirm the operation of the thermal distortion generator and to obtain experimental data. This data was used to visualize the dynamics of the thermal distortions produced and to show the temperature ramps produced by the generator. This data was used to verify that the distortion generator operated correctly and met all of the design constraints and requirements set forth.

III. ACKNOWLEDGEMENTS

The author wishes to express sincere gratitude to Dr. Joseph Schetz, of the Aerospace and Ocean Engineering Department at Virginia Polytechnic Institute and State University, who provided the opportunity to attend graduate school. The author expresses appreciation to the members of his graduate advisory committee for their support : Dr. W.F.O'Brien Jr., Co-chairman, Dr. C.L. Yates, Co-chairman, and Dr. B. Grossman. The support received from the Mechanical Engineering Department, which made the author's graduate study possible, is gratefully acknowledged. The author also wishes to extend thanks to Dr. L. Roe, of the Mechanical Engineering Department, who provided council during the early development stages of the combustion design concepts. Dr. Milt Davis, at the Arnold Engineering Development Center, provided assistance in the initial design concept phase that was greatly appreciated. Finally, the author wishes to thank Mr. Frank Caldwell, of the Mechanical Engineering Department's Instrument Shop, who provided invaluable assistance in developing the data gathering instrumentation and also helped to solve problems encountered with it.

IV. TABLE OF CONTENT

TABLE OF CONTENT (continued)

V. LIST OF FIGURES

LIST OF FIGURES (continued)

LIST OF FIGURES (continued)

LIST OF FIGURES (continued)

Page

LIST OF FIGURES (continued)

LIST OF FIGURES (continued)

VI. LIST OF TABLES

VII. NOMENCLATURE

A - Speed of sound

a - Area

C - Carbon atom

C_p - Constant specific heat

C_v - Variable specific heat

H - Hydrogen atom

h - Film coefficient

H - Height of duct

k - Thermal conductivity

L - Length of recirculation zone

$\dot{m}$ - Mass flow rate

$\dot{m}_{HOT}$ - Mass flow rate of hot air

$\dot{m}_{COLD}$ - Mass flow rate of cold air

M - Mach number

Me - Exit mach number

Mo - Free stream mach number

Nu - Nusselt number

N - Nitrogen atom

O - Oxygen atom

P - Power

Po - Total pressure

Pe - Exit static pressure

p - Static pressure

Pc - Combustion chamber pressure

Pr - Prandtl number

NOMENCLATURE (continued)

q- Heat transfer

R- Gas constant

Re- Reynolds number

s- Entropy

To- Total temperature

Tc- Combustion chamber temperature

T- Static temperature

T_{HOT}- Temperature of hot air

T_{COLD} Temperature of cold air

T_{MIX} - Temperature of mixture

T_{FIN} - Temperature of fin surface

ΔT - Local temperature minus ambient temperature

u- Viscosity

U- Internal energy

V- Volume

v- Velocity

v1- Velocity of approaching stream

v2- Velocity of flow past the wake

W- Width of wake

X- Length

Xo- Initial length

Φ - Equivalence Ratio

δ - Boundary layer thickness

τ - Ignition time

γ - Ratio of specific heats

ρ- Density

NOMENCLATURE (continued)

ACRONYMS

AEDC- Arnold Engineering Development Center

AIP- Aerodynamic Interface Plane

ARP- Aerospace Recommended Practice

ATM- Atmosphere

FSC- Flame Stabilization Criterion

JDAPS- Joint Dynamic Airbreathing Propulsion Simulations

NAPTC- Naval Air Propulsion Test Center

NASA- National Aeronautics and Space Administration

JANAF- Joint Army Navy Air Force Group

STANJAN- Stanford University JANAF Thermochemical Tables

STOL- Short Takeoff and Landing

VTOL- Vertical Takeoff and Landing

VIII. INTRODUCTION

Throughout an aircraft's flight envelope, the inlet and engine must remain aerodynamically compatible. This is to say that situations which lead to engine surge, compressor stall, or other malfunctioning of the propulsion system must be avoided or at least reduced to a tolerably low frequency of occurrence. Such situations are produced by a departure of the airflow, as delivered from the inlet to the engine, from the ideal of a flow that is uniform in pressure, temperature, gaseous content, and uniformly axial in direction. No real flow ever achieves this ideal however, in the pursuit of high intake pressure recovery for on-design operation, flows are sufficiently uniform so as to pose no compatibility problems.

It is of interest to recall a number of examples, from the many, in which incompatibility was revealed in flight test during the development of new prototype aircraft. The F-100, Fig. 1, with the J-57 engine, encountered engine surge in high G turns at 35,000 feet altitude and above. The aircraft had a pitot type inlet in the nose of the fuselage, the best form possible from a level performance aspect. The presumed cause of surge was a flow separation on the windward lip of the inlet when the aircraft was at an angle of attack in high G turns.

The Hunter, Fig. 2, a subsonic fighter aircraft, had inlets mounted on the wing root leading edge and gun ports under the nose of the fuselage. The aircraft had the RA-7 Avon engine and it was found that firing the guns, at high altitude, caused engine surge and at times flameout. At least three factors acting singly or in combination were identified as likely causes. First, the pressure wave from the expanding gases disturbed the intake flow. Second, the high temperature of the weapon gases raised the overall temperature of the inlet air. Third, the combustible nature of the weapon gases caused a

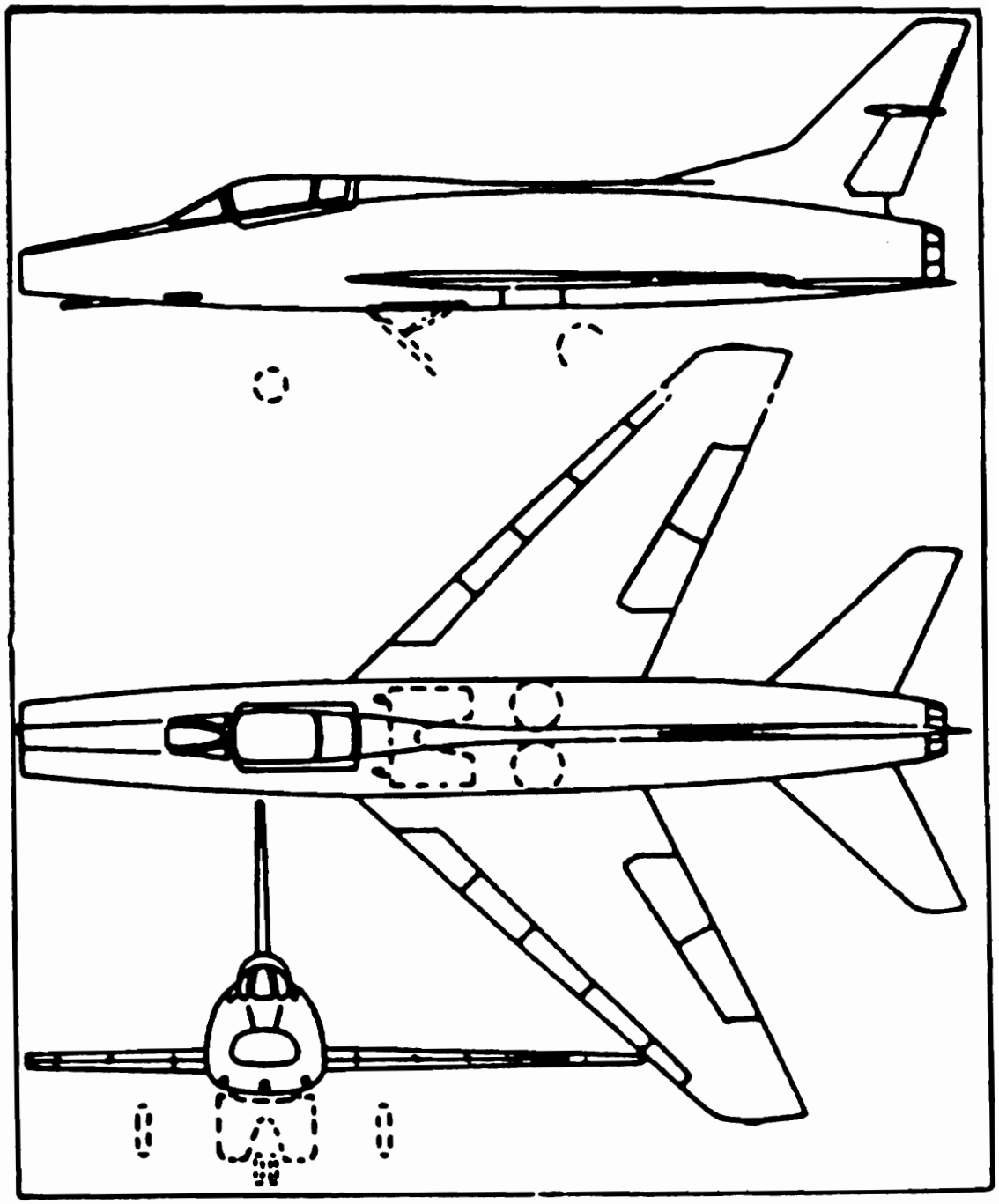

Figure 1. The North American F-100A Super Sabre Ref.(21)

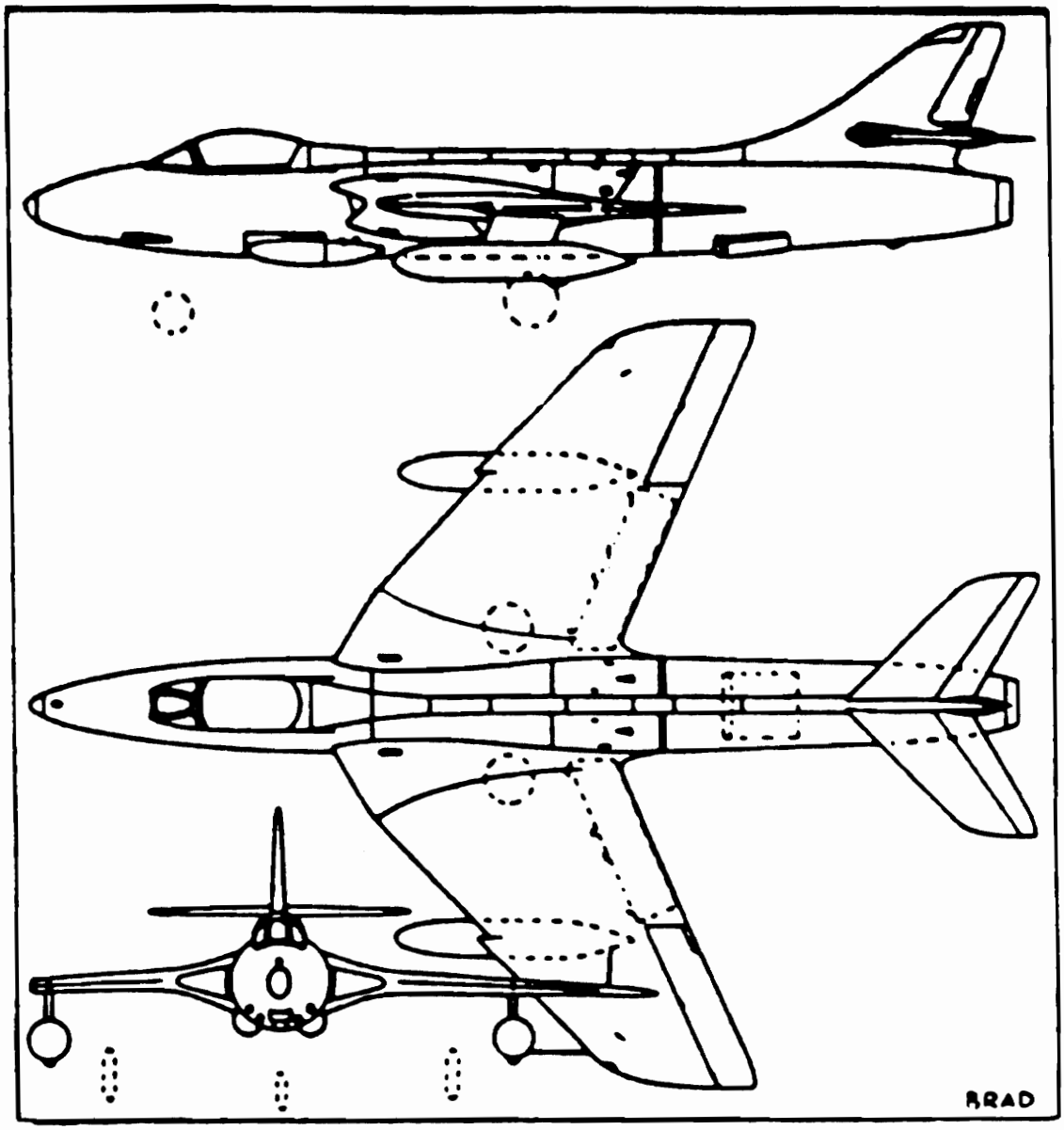

The Hawker Hunter F. Mk. 6.

Figure 2. The Hawker Hunter F. Mk. 6. Ref.(21)

transient overfueling of the engine. Arrangements for flow deflectors on the fuselage were of some value, but the main solution came from engine modifications. This meant increasing the margin between the stall line and the operating point, a permanent performance reducing change, and restrictive control of fueling during gun firing.

The A-10, Fig. 3, had twin turbofan engines mounted on the tail and a GAU-8/A 30mm "Gatling" gun mounted in the nose of the fuselage. Fan stall, followed by compressor surge, and engine flameout were found to occur when the aircraft was in rapid descent while firing the gun.

The main sources of temperature distortion for gas turbine engines are the ingestion of exhaust gases from armament firings such as guns, rockets, and missiles. Other sources include engine exhaust gas reingestion from VTOL/STOL aircraft, helicopters, thrust reversing operations, and hot steam ingestion from catapult launches from aircraft carriers. The following engine inlet effects will occur during the firing of armament or engine exhaust gas reingestion:

1) Increased inlet temperatures
2) Changed inlet pressure
3) Distorted inlet pressure and temperature profiles
4) Entry of combustibles into the engine
5) Reduced oxygen content in the gases entering the engine

The effect of temperature distortion, in terms of the entire compressor, is to effectively lower the surge line and to shift the operating point to the left, to a lower corrected rotor speed on the compressor map. Consider the exhaust flow of a 2.75 inch air to air rocket shown in Fig. 4. It has a combustion chamber pressure and temperature

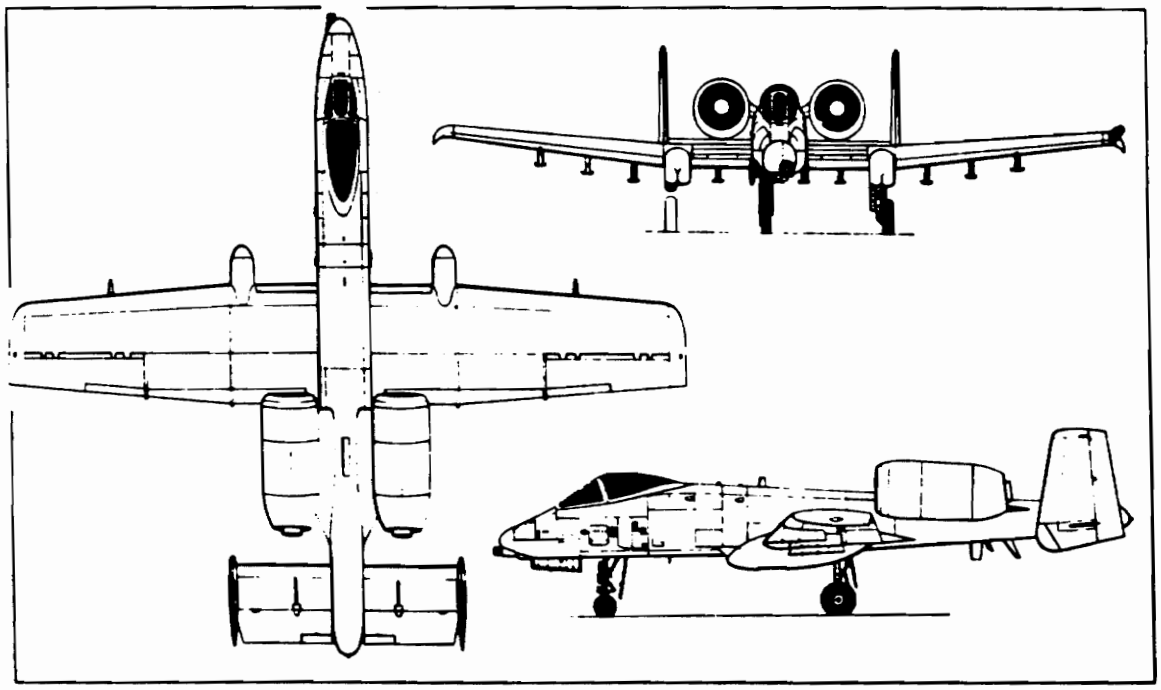

Figure 3. The A-10 Ref.(21)

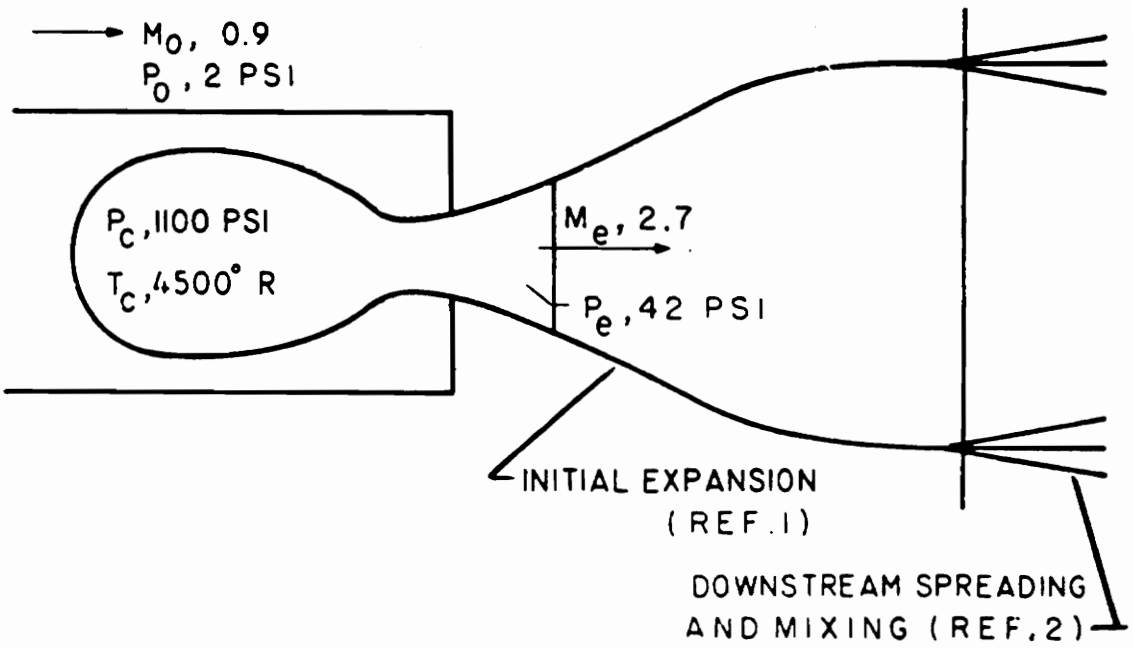

Figure 4. Exhaust Flow Of The 2.75 Inch Air To Air Rocket Ref.(2)

of 1100 psi and 4500 (R) respectively. It has a design exit Mach number of 2.7 and a design exit static pressure of 42 psi. Since this pressure is considerably above the ambient pressure at altitude, the exhaust plume will expand greatly upon leaving the nozzle. Fig. 5 shows the plume of a rocket launched from an aircraft moving at Mach 0.9 at an altitude of 45,000 feet. At the time shown, approximately 0.3 seconds after firing, the rocket is 60 feet in front of the launch station and is moving away at a velocity of 400 ft/sec. Contours of temperature are shown for the exhaust plume of a single rocket. These temperatures are expressed as the difference in the temperatures at various locations in the plume, and the ambient temperature. Thus if the location of the inlet relative to the launch station is known, temperature increments at the inlet can be estimated. For example, consider a one foot diameter inlet whose center line is 1.5 feet from the launch station. If this inlet is in the plane of the launch station, the average temperature of the incoming air is 200 degrees above the ambient. This temperature increment varies from 260 degrees on the inner wall of the inlet to 140 degrees of the outer wall. Fig. 6 shows an aircraft in the process of firing cannons. As the muzzle gases move out ahead of the inlet, they mix with the incoming air and the inlet temperature is increased. An additional factor is muzzle flash, a sudden burning or explosion of the gases in front of the guns. When this happens, the hot gases expand in front of the aircraft and enter the engine at greater than normal rates.

The evidence presented indicates that there is a need to study the phenomena of ingesting exhaust gases resulting from armament firings into gas turbine engines. It is clear, based upon past history, that armament and gas turbine engine exhaust gases, when ingested into a gas turbine engine, reduce the engine's performance and stability. Therefore, an understanding of how this phenomenon affects the engine's performance and stability would be valuable to gas turbine engine manufacturers as well as the aircraft manufacturer. The material contained in this thesis identifies an approach

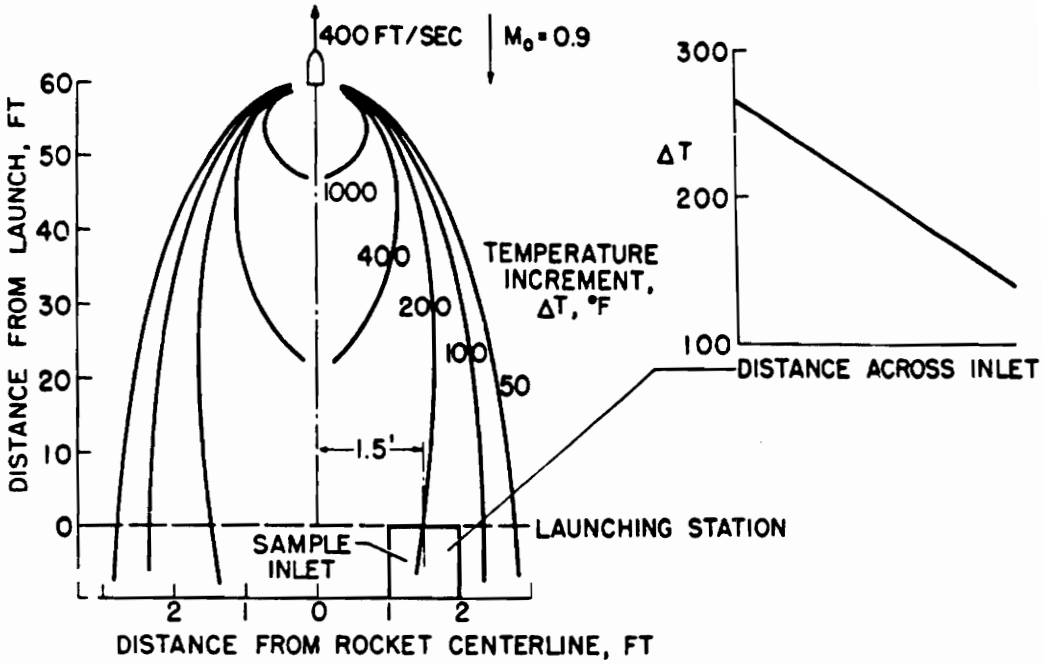

Figure 5. Exhaust Plume From The 2.75 Inch Air To Air Rocket Ref.(2)

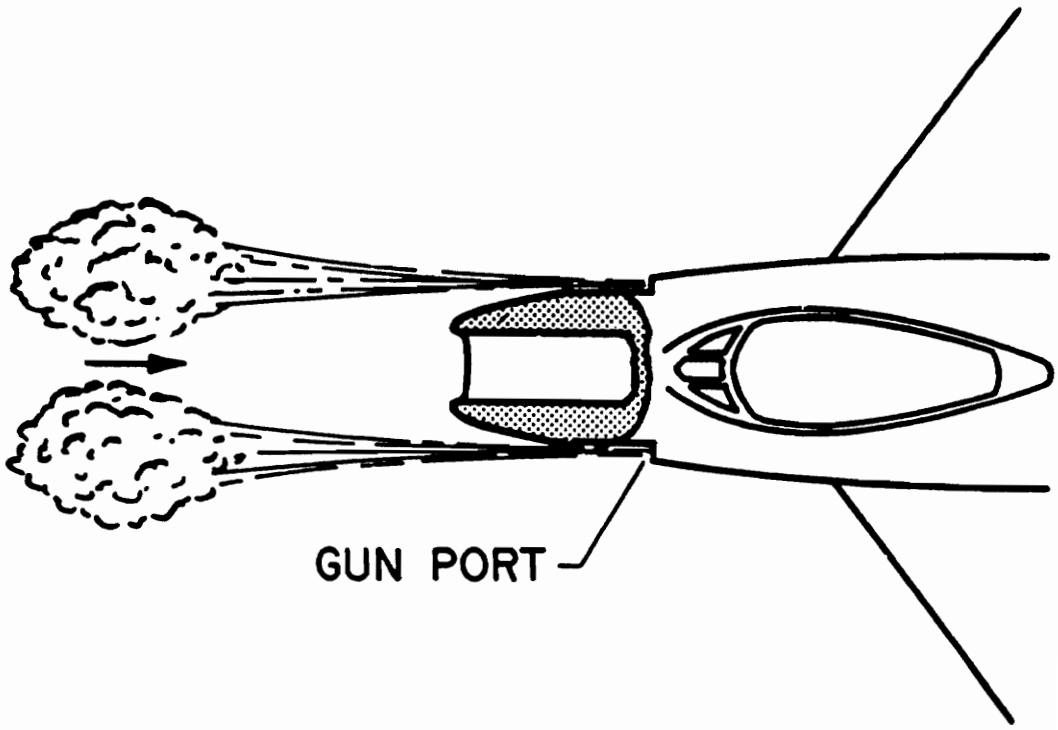

Figure 6. Cannon Blast Effect Ref.(2)

used to design, fabricate, and test a device to simulate temperature distortions associated with the ingestion phenomena. This device will be used for simulation of steady state and dynamic temperature distortions in turbine engine research and development experiments.

IX. LITERATURE REVIEW

The problem of engine stall or flameout due to rocket exhaust gas or gun gas ingestion into the aircraft engine has been recognized for years. The most deleterious case of hot gas ingestion was experienced during the early flight testing of an F2H aircraft. Temperature ramps up to 36,000 degrees F/sec, with peak temperatures of 1100 degrees (F) at engine inlets aligned with the flight path of air launched missiles (Sidewinder, Zuni, etc.), were documented. The minimum temperature ramp required to cause engine flameout in that case was approximately 4500 degrees F/sec. The temperature rise time for a single rocket firing was observed to be 0.1 to 0.2 seconds, while decay to ambient inlet temperature generally took 0.2 to 0.4 seconds. The rail launch method, for launching the missile from the aircraft, appeared to be a factor in the severe temperature ramps because of the very close proximity of the engine inlet to the missile's exhaust plume. Recent experimental studies of rocket exhaust gas ingestion by simulation in engine test cells revealed that the stall/flameout temperature ramp is different for each engine /inlet combination. Other phenomena associated with gas ingestion are supersonic inlet unstarts, temporary engine control anomalies, and deposition of solid rocket particulates on engine internal components.

A survey was conducted [1] to evaluate several rocket exhaust gas ingestion simulation techniques for the United States Air Force Arnold Engineering Development Center. Five different simulation techniques were examined and evaluated. The first simulator was constructed at the Naval Air Propulsion Test Center as shown in Fig.7. It was installed at the inlet of a J52-P-6A engine. It was designed to burn specially fabricated grains of rocket propellant in a boiler-plate motor capable of producing up to 30 lbm/s 13.6 (kg/s) exhaust gas flow for 0.1 second. The grains were designed and

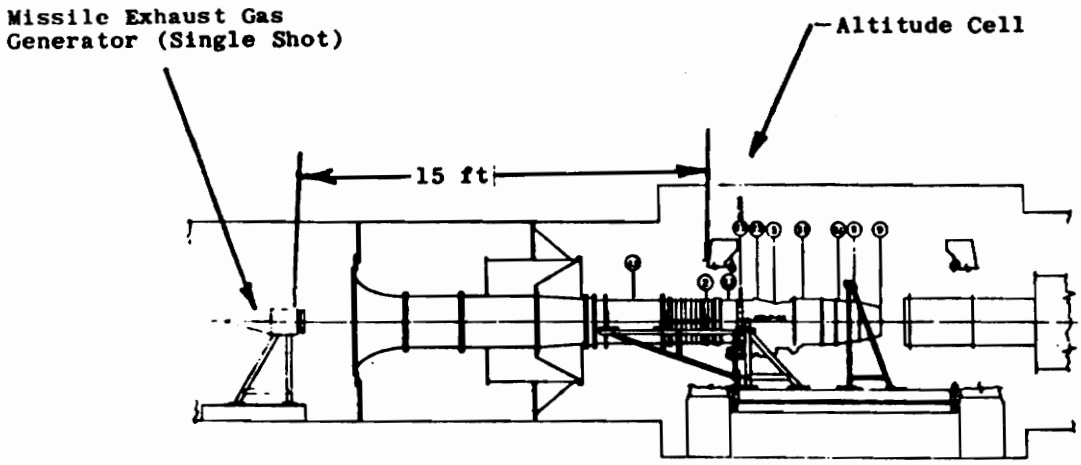

Figure 7. NAPTC Missile Exhaust Gas Simulator Ref.(1)

fabricated at the Naval Ordnance Station at Indian Head, Maryland and were made available with either double base (Zuni missile) or composite (Sparrow, Sidewinder) formulation. The simulator produced an excellent gas composition and temperature ramp similar to that encountered during the ingestion of rocket exhaust gases. However, the run time was short and the control of the temperature distortion produced was very poor. Also, the simulator could not produce controlled spatial temperature distortions. From a financial standpoint, this simulator was very expensive to operate. The second simulator examined was fabricated and operated at the NASA Lewis Research Center. It was a segmented hydrogen burner that was installed upstream of a turbofan engine. It was designed to produce a steady state spatial temperature distortion at the engine inlet. Fig.8 shows the hydrogen burner. High pressure compressor stalls were obtained at temperature ramps above 3000 degrees (F)/s. Fan stalls were not achieved because the hottest and most rapidly changing temperatures were ingested primarily by the core engine. This problem was inherent with the design of the hydrogen burner. The burner also had operational problems at the pressures and temperatures associated with high altitude flight conditions. Also, the correct gas composition was not simulated. The third simulator examined was a facility developed for the Arnold Engineering Development Center and Pratt and Whitney, at a Pratt and Whitney engine test cell. It is shown in Fig.9. The facility utilized a pivoting nozzle that discharged heated gaseous nitrogen into the wind tunnel flow towards an inlet/engine model. A tactical missile launch was simulated by sweeping the hot gas plume across the inlet. The gas composition and temperature ramp produced was poor. A rocket motor gas generator was recommended instead for full scale testing. The fourth simulator examined was constructed at the Arnold Engineering Development Center. It consisted of a turnstile mount that supported four solid rocket motors as indicated in Fig.10. The turnstile was mounted in front of the engine inlet

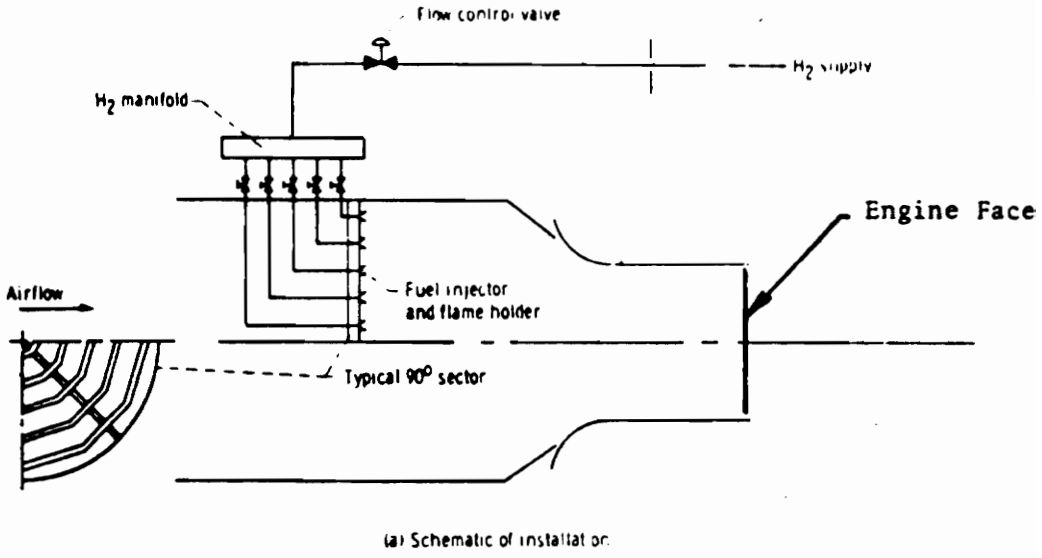

(a) Schematic of installation

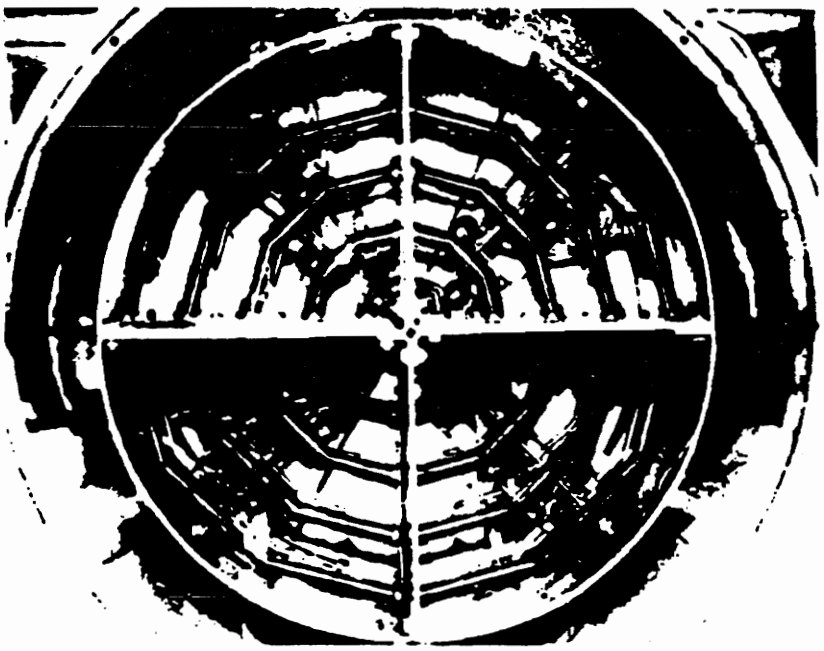

Figure 8. NASA's Hydrogen Burner Temperature Distortion Generator Ref.(1)

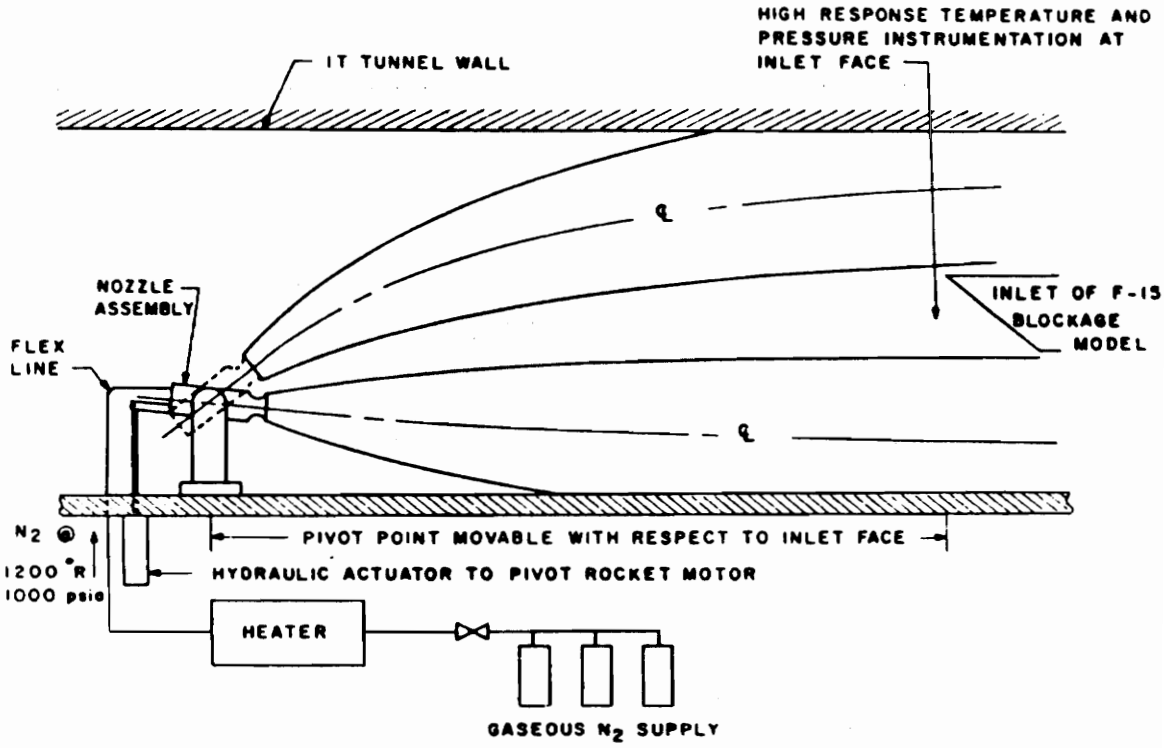

Figure 9. AEDC/Pratt & Whitney Pivoting Nozzle Distortion Generator Ref.(1)

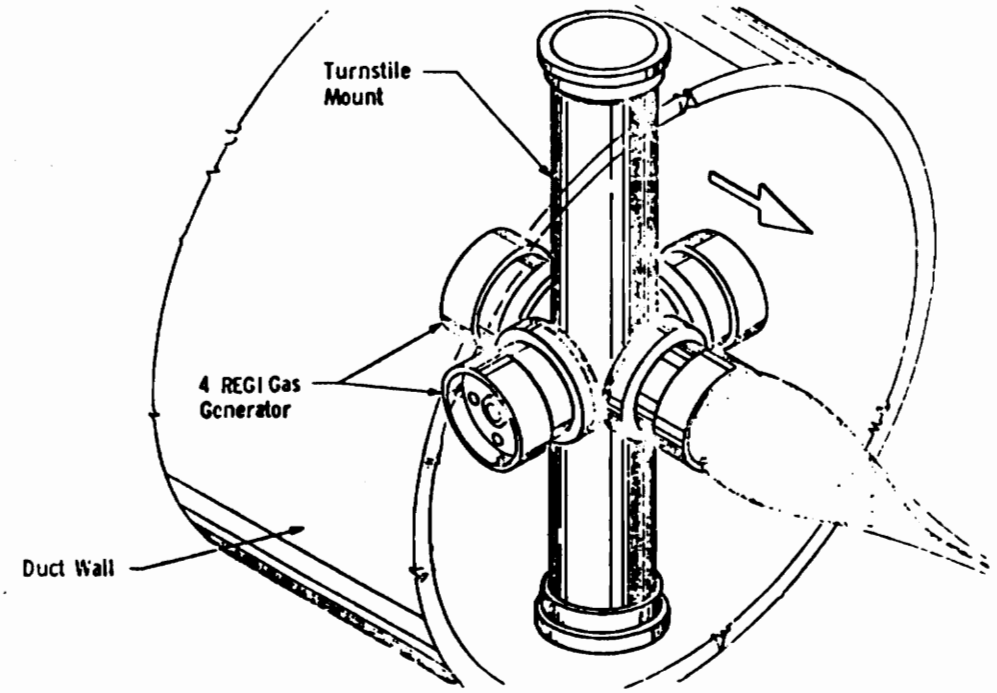

Figure 10. AEDC Turnstile Thermal Distortion Generator Ref.(1)

and allowed to rotate . The design was similar to the simulator constructed at the Naval Air Propulsion Test Center, except it allowed four rocket motors to burn instead of one. The problems associated with the simulator at the Naval Air Propulsion Test Center were encountered with this simulator. It produced a good temperature ramp and gas composition; however, the control of the temperature distortion was poor. It did not produce controllable spatial temperature distortion. The final simulator examined was an air jet distortion generator that was primarily used to produce pressure distortions for the Arnold Engineering Development Center. As indicated in Fig.11, it consisted of a circular rake mounted in front of the engine inlet. High pressure compressed air was injected into the oncoming free stream to locally reduce air velocities and create a region of low pressure. The system was converted to a hot gas injector with minor hardware modifications. This approach produced excellent spatial temperature distortions but was limited to a maximum temperature of 300 degrees (F).

Childs, Kochendorfer, Lubick, and Friedman [2] set out to determine the actual temperature and pressure profiles at the inlet of an aircraft flying at high altitudes, after the launching of an air to air rocket and the firing of cannons. Their investigation led to the identification of specific effects on the compressor and combustor, during the firing of armament at high altitudes. These results involved actual pressure and temperature increments measured at the inlet, during the firing of armament. Other results include pressure and temperature distortion effects on the compressor map and combustion stability limits during the ingestion of combustibles into the engine.

Walter and Shaw [3] tried to predict the F100 engine's response to circumferential pressure and temperature distortion. They conducted several steady state distortion experiments on an actual F100 turbofan engine. Data included engine response to

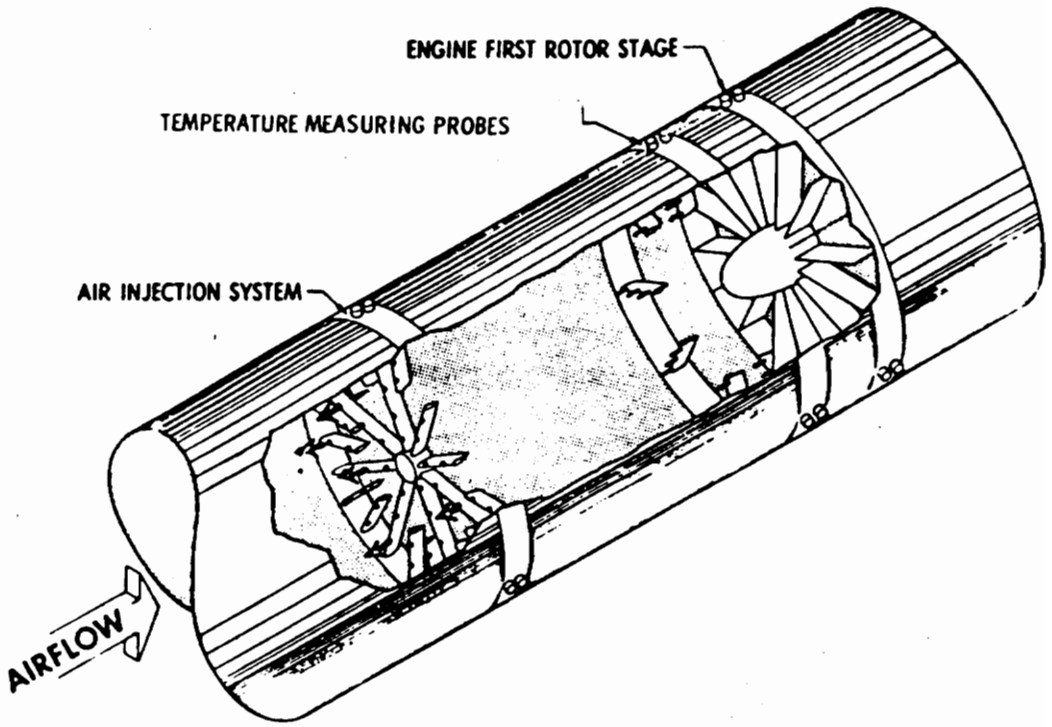

Figure 11. AEDC Airjet Thermal Distortion Generator Ref.(1)

spatial pressure, temperature, and combined pressure and temperature distortions on the engine's performance and stability.

Braithwaite, Garber, and Mehalic at the NASA Lewis Research Center [4] quantified steady state pressure, temperature, and combined pressure and temperature distortions with a simplified parallel compressor theory mathematical model. They obtained steady state pressure, temperature, and combined pressure and temperature distortion data on a General Electric J-85 eight stage turbojet engine. From the data, and with the aid of parallel compressor theory, they derived the theoretical performance of the J-85, when subjected to pressure and temperature distortions.

The Society of Automotive Engineers, Inc. [5] laid out the guidelines for gas turbine engine inlet flow distortion research in their Aerospace Recommended Practice ARP 1420. Details about instrumentation and measuring devices, that should be utilized during experiments, are outlined in this document.

The Society of Automotive Engineers Aerospace Resource Document [6] discussed the inlet temperature distortion problem. It also discussed some of the past and present temperature distortion work. It indicated that the sources of temperature distortion that are of concern are weapon wake ingestion, STOL/VTOL hot gas reingestion, thrust reverser exhaust ingestion, and steam ingestion. Helicopter flight tests were conducted with a CH-47 and YUH-61A to determine the effect of reingesting hot exhaust gases. Inlet temperatures of 610 (R) were reached and resulted in a decrease in horsepower. Understanding of reingestion during hover was gained by testing a 1/15th scale model. Primary design variables were nozzle area, inboard blade geometry, and engine location. Based on these tests, an optimum design was chosen for full-scale production aircraft. A recent helicopter engine, the T-700, was subjected to temperature distortion. Part of the test consisted of placing an engine inlet temperature sensor in the

inlet. When the sensor detects either hot or cold distorted flow, a control will adjust the fuel flow and vary the geometry accordingly and change the compressor surge margin.

Hot gas reingestion in the AV-8B V/STOL aircraft is within the tolerance of the compression system. However, the proposed use of plenum chamber burning in the fan duct will increase the temperature of any ingested gas. The airframe and engine manufacturers have conducted rig and full-scale tests of various nozzle, inlet, and mechanical deflector designs in an attempt to reduce the levels of gas reingestion. Laboratory test data has usually been produced by the NASA Lewis hydrogen-fueled temperature distortion generator.

X. PURPOSE OF RESEARCH

A literature search and review has indicated that extensive work and research has been conducted on steady state temperature distortions. Much of this work was conducted during the early development of the gas turbine engine. The primary reason for these efforts was to obtain crucial information about the performance of axial flow fans and compressors subjected to circumferential, spatial, thermal distortions. This information aided gas turbine engine manufacturers when designing high performance gas turbine engines for military applications. Also, the information was required to develop and verify computer codes that would predict the performance and stage characteristics of axial flow fans and compressors throughout their entire operating range. As technology advanced, fans and compressors were being designed with finite element compressor design codes and stronger materials. This allowed faster blade tip speeds that reached the transonic and supersonic regimes. Again, steady state thermal distortion work and research was conducted on these advanced fan and compressor designs. Computer codes were also developed to predict the performance characteristics of these transonic and supersonic fans and compressors throughout their entire operating range.

A problem with the steady state thermal distortion work and computer code development is that the phenomena of ingesting rocket exhaust gas, the reingestion of gas turbine engine exhaust gas, and the pressure distortions resulting from rapid maneuvers are not steady state. The thermal distortion patterns produced at the face of the fan or compressor of a gas turbine engine during exhaust gas ingestion are unsteady or time varying. Also, the chemical composition of the ingested gas is very different from that of air. Therefore, there are regions of the fan or compressor that have air flowing through, and there are other regions that have a foreign gas flowing through at a significantly higher

temperature. The consequence of the presence of this foreign gas, at a significantly higher temperature, is that the compressible aerodynamics are changed locally on the fan or compressor where the foreign gas is present. This may cause the fan or compressor blade to stall. The engineering field of transonic and supersonic fan and compressor component design and analysis lacks the crucial experimental information regarding unsteady temperature distortions. Due to the lack of information, mathematical models and computer codes cannot be developed and verified to accurately predict the performance characteristics of transonic or supersonic fans and compressors subjected to unsteady thermal distortions. This research project is directed toward developing an experimental technique to obtain data that can verify mathematical models and computer codes of this particular type. It will identify an approach that can be taken to obtain dynamic thermal distortion experimental data.

XI. Initial Design Concepts and Analysis

In this section, the initial design concepts are discussed in detail along with a design analysis for each concept.

The first approach taken to developing the initial design concepts was to perform an energy balance analysis. The energy balance analysis gave information as to how much energy was necessary to achieve the desired temperature rise for all of the design concepts. Assumptions were made about the airstream in which the thermal distortion generator would operate. Assumptions were also made about the temperature increase required to stall and eventually surge the fan or compressor, and about the diameter of the inlet duct. These assumptions were based upon measured results from wind tunnel tests at AEDC and at NASA Lewis as well as cited references in the bibliography section of this thesis. The assumptions are:

1) The inlet duct has a 46 cm (18 inch) diameter.
2) The temperature increment required to stall the fan or compressor, is approximately 250 degrees.
3) The airstream is uniform.
4) The velocity of the airstream, in the inlet duct of a transonic fan or compressor, is approximately 183 m/s (600 ft/s).
5) Reference conditions are sea level conditions.

With this information, the conservation of mass principle, and the First Law of Thermodynamics, the energy balance was performed as shown in Fig. 12.

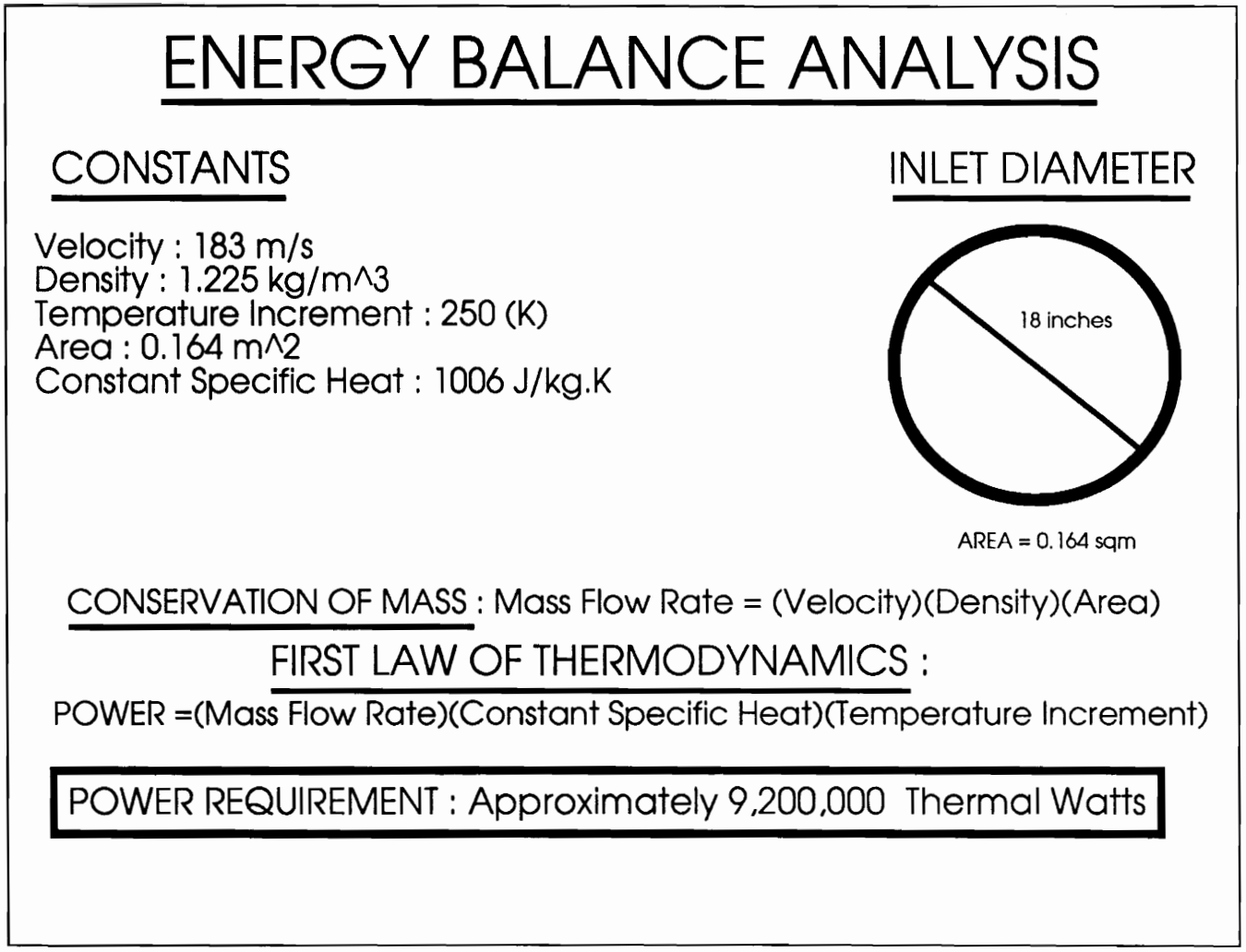

Figure 12. Energy Balance Analysis

Two different design concepts were considered for the thermal distortion generator. One was an electrical distortion generator that used an electric current to achieve the temperature rise. The second was a chemical distortion generator that used the combustion of a gaseous fuel to achieve the temperature rise. A design constraint for both types, was the requirement that the design had to be circular for mounting to or in the inlet duct of a fan or compressor. The primary design requirement for the distortion generator was that it be subdivided into sectors that could operate independently of each other. This ability allowed the option of distorting either a sector of the inlet or the entire inlet. A final design requirement was that the distortion generator had to produce an unsteady distortion pattern that was as uniform as possible.

The Electrical Heater Design Concept

An electrical heater design concept was considered. Figure 13 shows the initial design concept for the electrical heater. It consists of a hollow steel cylinder, 46 cm in diameter and 61 cm in length, that is subdivided into four quadrants by use of steel plates. Occupying each quadrant are fins made of tungsten that are capable of being heated to approximately 1500 degrees (K). These fins are positioned in the quadrants such that the airflow streamlines run parallel to the fin flat surface. The heater operates by passing a high electrical current through each fin, at a specified frequency. The temperature rise is achieved by heat convection from the hot fin surface to the air. Each quadrant is wired on a separate circuit thus, an operator can operate as many quadrants as desired, in or out of

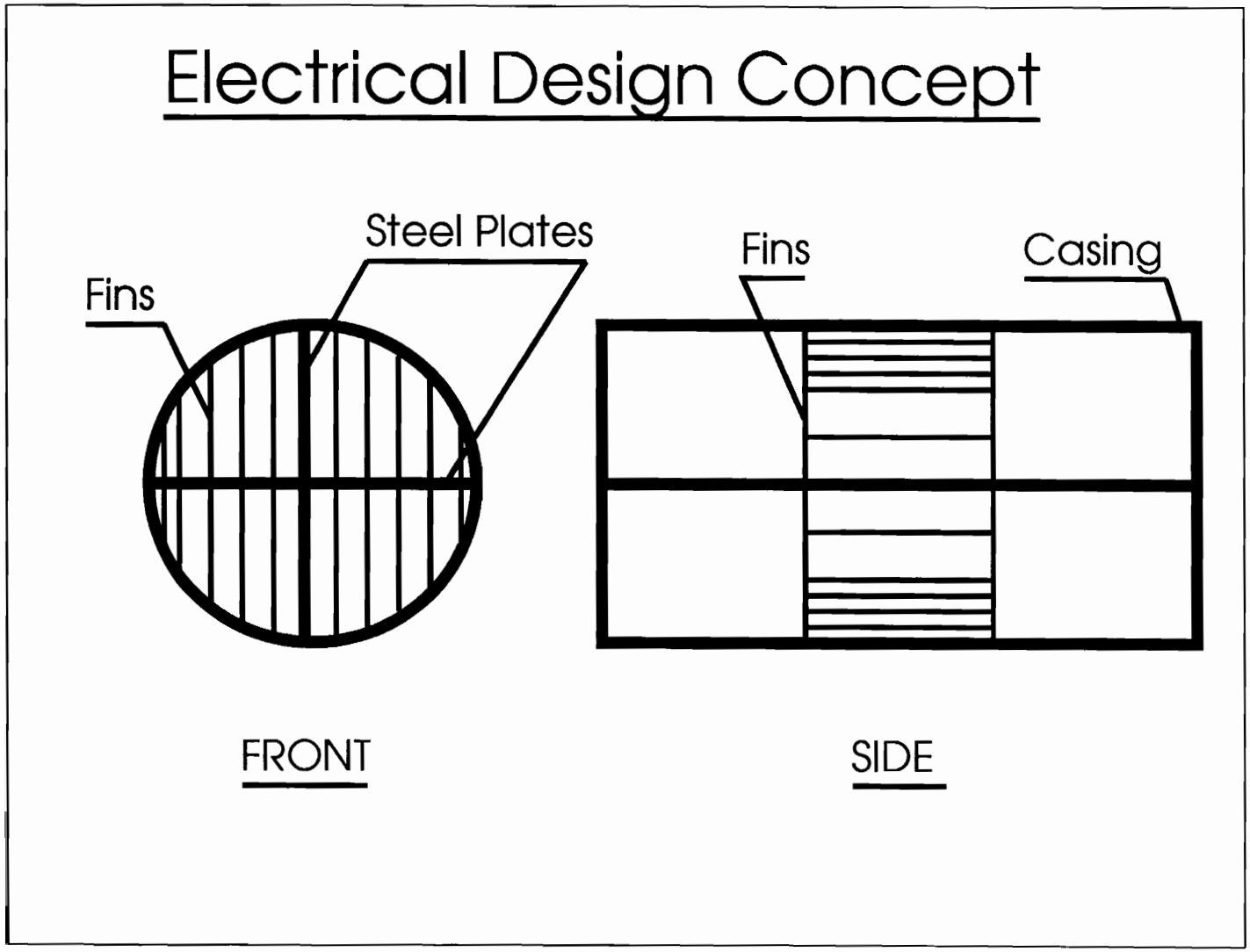

Figure 13. Electrical Design Concept

phase with each other. A disadvantage of this design is the high inlet blockage and pressure losses associated with the fins. A heat transfer analysis is performed in Fig. 14. The properties and parameters for air at standard pressure and temperature necessary for the analysis are indicated. The fin surface temperature is assumed to be 1500 (K). Figure 15 is a plot of the fin surface area verses the energy transfer from the heat transfer analysis. All of the properties and parameters for air and the fin surface temperature remained constant while the fin surface area was varied. Figure 15 indicates that as the fin surface area increases the amount of energy that can be transferred from the fin to the air stream also increases. A problem with increasing the fin surface area is that the wetted area also increases. Therefore, losses in total pressure associated with skin friction will increase. A design that required more than approximately 0.5 sqm of fin surface area would be considered unreasonable for this particular application. More than this amount would be unreasonable because the losses in total pressure would be significant. Figure 15 indicates the amount of fin surface area at 1500 (K) necessary to transfer a certain amount of energy. The trend indicates that to transfer the amount of energy determined in the energy balance analysis would require fin surface area that would be much greater that 0.5 sqm. Operating the fins at a higher temperature is not an option due to the material's maximum temperature limit. It was also predicted that the convection heat transfer rate of the fins would be to slow to produce a high frequency cycle. It was concluded that the fins would be unreliable. Selection of this type of design also precludes the possibility of conducting any kind of foreign gas research, since no combustion gases are produced. Finally, another disadvantage noted with this type of a design is the large and heavy equipment necessary to operate the fins at high temperatures. This equipment would not allow the heater to be compact and would be burdensome by occupying space in the test cell.

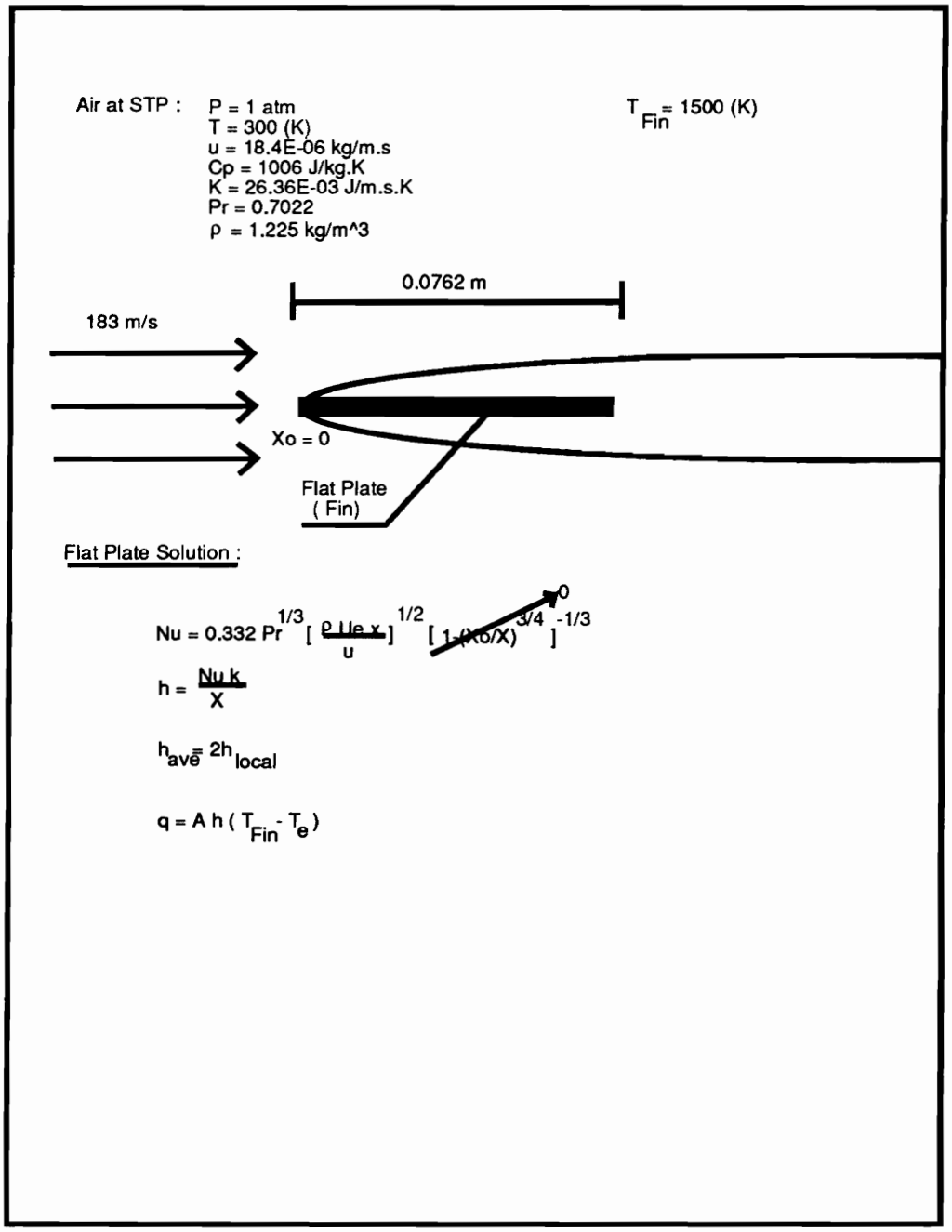

Figure 14. Heat Transfer Analysis

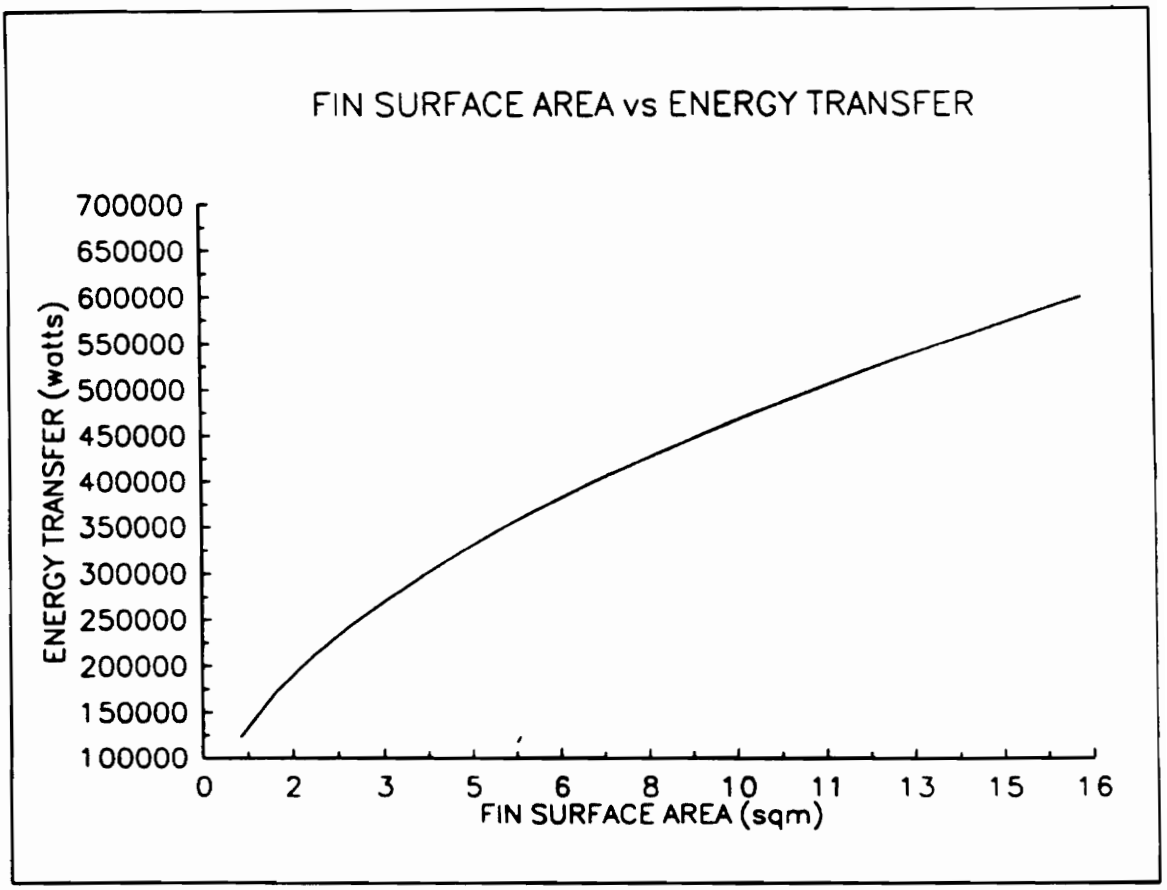

Figure 15. Fin Surface Area vs Energy Transfer

The Chemical/Combustion Burner Design Concepts

A chemical thermal distortion generator that used the combustion of a gaseous fuel to achieve the temperature rise was also considered as a design concept. A combustor-type thermal distortion generator seemed favorable due to the high energy release associated with the combustion of a small amount of fuel. Three gaseous fuels were considered as candidates to fuel the combustor: hydrogen, methane, and propane. By performing an energy balance analysis with the heats of formation, continuity, the first law of thermodynamics, and the stated assumptions, the energy release and fuel requirement of each fuel was determined for each specified temperature increment. The analysis and results are summarized and shown in Fig. 16 and Fig. 17. Hydrogen seemed the most promising candidate due to its high energy release and the fact that it had the lowest fuel requirement out of all the fuel candidates. However, gaseous hydrogen is difficult to contain and leaks through pipes and valves that normally do not leak for other gases. Also, gaseous hydrogen is very easy to ignite and would have produced a potentially hazardous situation inside the test cell. For these reasons, it was discarded as a fuel candidate. Methane had the lowest energy release and consequently, the highest fuel requirement. Methane was an appealing candidate for the combustor fuel because it was already in service in the test cell for operating gas heaters. The necessary plumbing could have been easily added to tap the gas supply line and draw the fuel. A disadvantage of the methane fuel candidate is its low pressure and flow rate in a commercial gas line. Since methane has the highest fuel flow rate requirement, it was predicted that high pressure compressors, turbopumps, and storage tanks would be necessary to bring the methane up to pressure to get the required mass flow rate. Propane was considered the most favorable fuel candidate. Its fuel flow requirement is less than for methane, and liquid propane could

		Heats of Formation (kcal/gm.mole)
Possible Fuels :	Propane C_3H_8	24.8
	Methane $C H_4$	17.9
	Hydrogen H_2	52.0

Conservation of Mass : $\dot{m} = \rho V A$

Area = 0.166 m^2

Velocity = 183 m/s

Rho = 1.225 kg/m^3

$\dot{m}$ = 37.2 kg/s

$\dot{m}$ = 9.3 kg/s per quadrant

First Law of Thermodynamics : $P = \dot{m}\, Cp\, \Delta T$

$P = (37.2 \text{ kg/s})(1006 \text{ J/kg.K})(\Delta T)$

Energy Release : 1 kcal = 4.18E+3 J

Hydrogen H_2 = (52.0 ~~kcal/gm.mole~~)(1000 ~~gm~~/kg)(4.18E+3 J/~~kcal~~) = 217360000 J/kg

Methane CH_4 = (17.9 ~~kcal/gm.mole~~)(1000 ~~gm~~/kg)(4.18E+3 J/~~kcal~~) = 74822000 J/kg

Propane C_3H_8=(24.8 ~~kcal/gm.mole~~)(1000 ~~gm~~/kg)(4.18E+3) J/~~kcal~~) = 103664000 J/kg

Fuel Requirement

ΔT(K)	Hydrogen (H_2) gm/s	Methane (CH_4) gm/s	Propane (C_3H_8) gm/s
100	17.2	50.0	36.1
200	34.4	100.0	72.2
300	51.7	150.0	108.3
400	68.9	200.0	144.4
500	86.0	250.1	180.5
600	103.3	300.1	216.6
700	120.5	350.1	252.7
800	137.7	400.1	288.8

Figure 16. Fuel Requirements

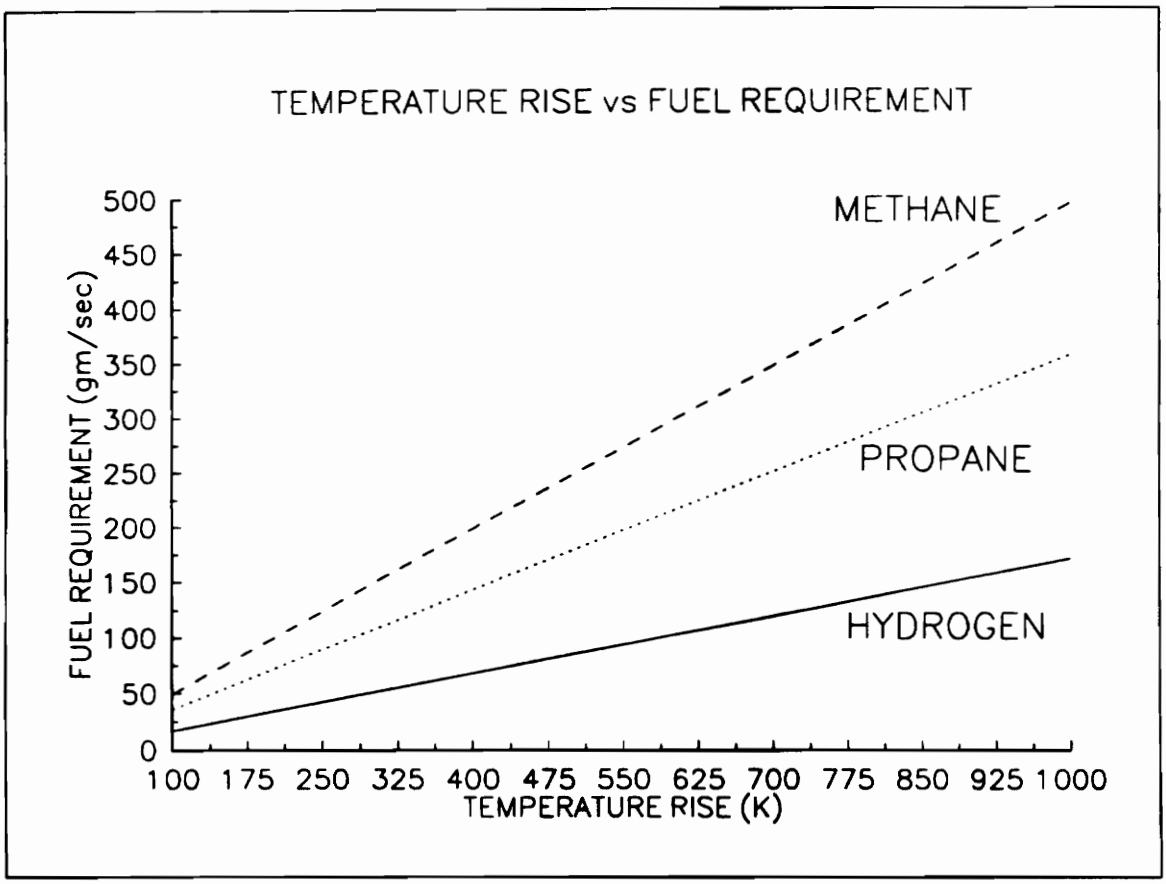

Figure 17. Temperature Rise vs Fuel Requirement

be easily stored in a small high pressure tank outside the test cell for delivery to the combustor. The required mass flow of propane is greater than for hydrogen but it is considered safer to use. For these reasons, propane was selected as the fuel for the combustor.

The External Combustion Design Concept

Two types of combustors were considered. The external combustion design concept, shown in Fig. 18, seemed preferable over an internal combustion design concept because combustion occurred external to the thermal distortion generator. This provided the advantage of controlling the combustion reaction independent of the internal flow conditions. The distortion generator consists of a hollow 61 cm steel cylinder, 46 cm in diameter, that is subdivided into four quadrants by use of steel plates. A channeling pipe runs from each of the quadrants to a separate pressure vessel containing compressed air. Each pressure vessel is heated by an external propane burner. The distortion generator operates by being mounted to the inlet of the fan or compressor. The low pressure in the inlet duct, produced by the fan or compressor, causes air to flow through the 46 cm diameter cylinder. At that time, a valve on the pressure vessel, is opened and closed at a specified frequency to allow the discharge of hot air into a quadrant. The mixing of the injected hot air, with the moving free stream, produces the temperature rise. The pressure vessels are constantly replenished with air by a high pressure compressor. An advantage of using this type of a design for a thermal distortion generator is that the propane burners can be ignited and allowed to burn continuously. They are easily regulated by a fuel regulator valve. Also, the operation of these four burners are independent of the distortion generator. A problem with this type of a design is the large volumes of hot air required to

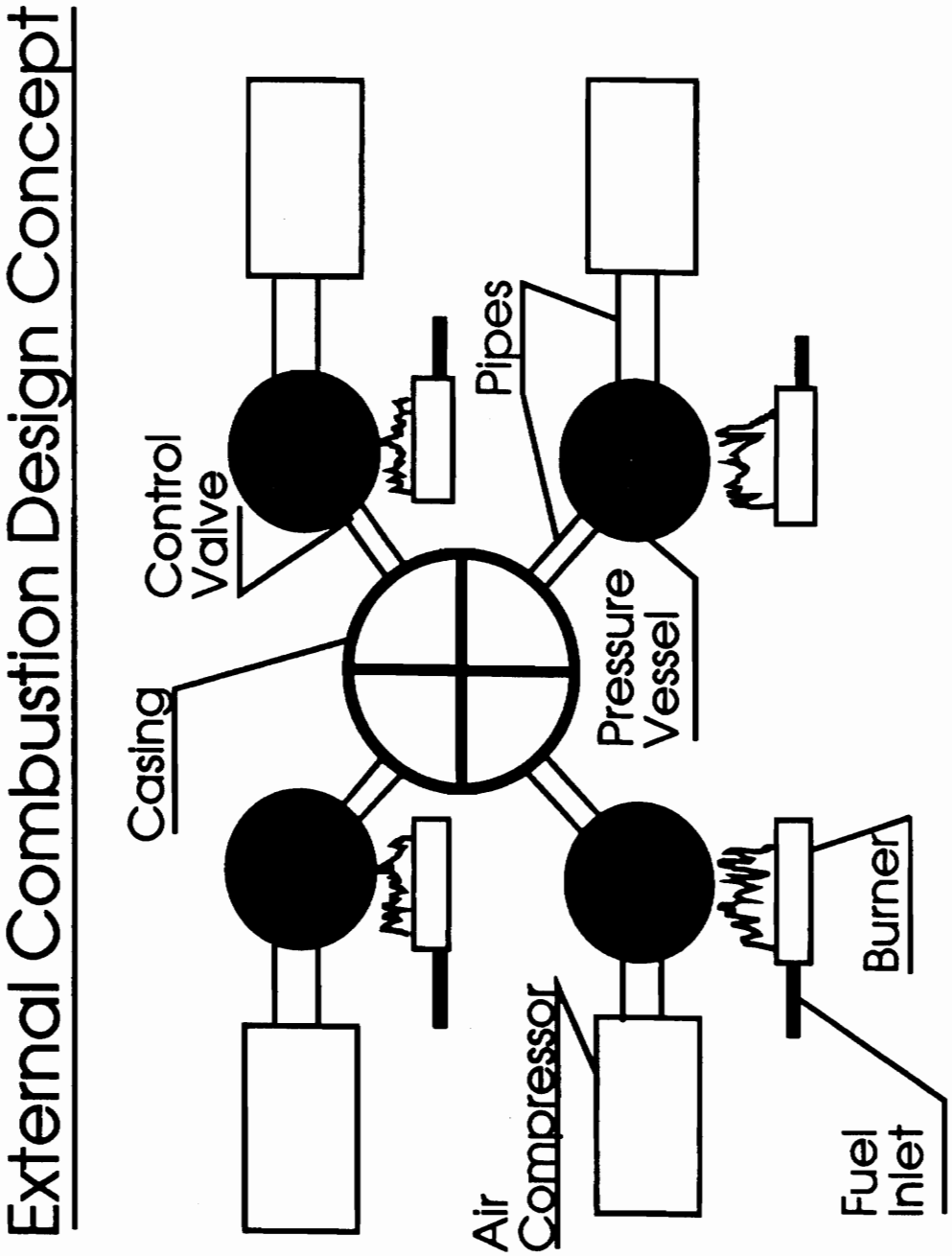

Figure 18. External Combustion Design Concept

mix with the free stream air to achieve the necessary temperature rise. Figure 19 indicates a mass averaging analysis utilized to determine the amount of hot air required to mix with the free stream to achieve the desired temperature rise. The results of this analysis are plotted in Fig. 20.

It was concluded that the external combustion design was not practical due to its complexity, the large volumes of hot air required to achieve the temperature rise, and the necessary hardware associated with its operation. Also, there are thermal losses associated with the design. The thermal losses occur from the transmission of energy from the combustion gases to the air inside the pressure vessel. The hot air, inside the pressure vessel, has to then transmit the energy to the free stream air flowing through the quadrant. There is also a considerable amount of energy loss from heat transfer through the channeling pipes and the pressure vessels to the ambient surroundings. For these reasons, external combustion design concepts were discarded and internal combustion design concepts were considered.

The Internal Combustion Design Concepts

The Hot Air Balloon /Afterburner Design Concept

The internal combustion design concept was considered more efficient because combustion occurred directly in a duct where the free stream air was flowing. The energy release was directly into the air stream in which energy was to be added to achieve a temperature rise. The internal combustion design concept was also judged to be smaller, compact, and less complex than the external combustion design concept Another advantage to using an internal combustion design for the thermal distortion generator was the fact that the internal combustion design also produced a foreign gas in addition to the

MASS AVERAGE ANALYSIS

$$T_{mix} = \frac{\int T\,d\dot{m}}{\int d\dot{m}} = \frac{(T_{hot})(\dot{m}_{hot}) + (T_{cold})(\dot{m}_{cold})}{(\dot{m}_{hot}) + (\dot{m}_{cold})}$$

$$T_{mix} = \frac{(T_{hot}) + \alpha(T_{cold})}{1 + \alpha}$$

$$\alpha = \frac{(\dot{m}_{cold})}{(\dot{m}_{hot})}$$

Figure 19. Mass Average Analysis

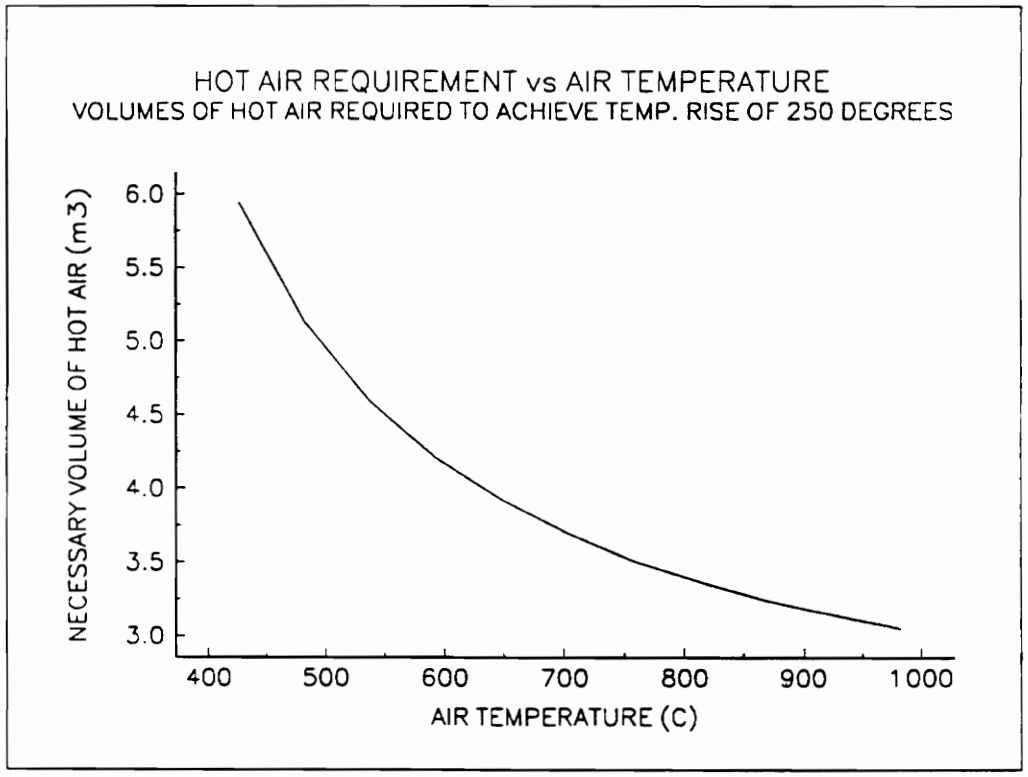

Figure 20. Hot Air Requirement vs Air Temperature

pocket of hot air. Unlike the electrical and external combustion design concepts that produced just pockets of hot air, the internal combustion design better simulated the ingestion of rocket or gas turbine engine exhaust gases.

The first internal combustion thermal distortion generator design concept considered is shown in Fig. 21. It consists of a hollow 61 cm steel cylinder, 46 cm in diameter, that is subdivided into four quadrants by use of steel plates. Fifteen cm into each quadrant is a manifold , 20 cm long with 2 mm diameter holes drilled all the way around its perimeter and throughout its length. At the end of the manifold is a set of concentric rings that have a circular cross section. The diameter of the cross section is 1cm. In the centers of these concentric rings is a solid circular cone that has a base diameter of 1 cm. The centers of these concentric rings and the cone base are aligned in the quadrant. Directly behind the concentric rings, mounted through the quadrant wall, is an ignition plug. This design concept is modeled after a burner that is used to inflate hot air balloons on the ground. The design is also similar to an afterburner of a gas turbine engine. The manifold functions as a fuel injection system, the concentric rings and cone function as a flameholder, and the ignition plug initiates the combustion reaction for each heating cycle. Air flows into a quadrant. Fuel is injected circumferentially into the airstream, perpendicular to the airflow streamlines, by the fuel injector system. The fuel and air mix as they flow over and into the wakes of the rings and cone. The ignition plug ignites the fuel air mixture and combustion occurs. The hot combustion gases and air exit the combustor in the rear. The four quadrants are independent of each other. Thus, a controller can operate as many quadrants as desired. The unsteady thermal distortion pattern is produced by injecting the fuel at a specified frequency. The function of the injector manifold is to inject fuel equally around the quadrant perimeter into the airstream. The function of the flame holder is to produce a turbulent wake that enhances fuel and air

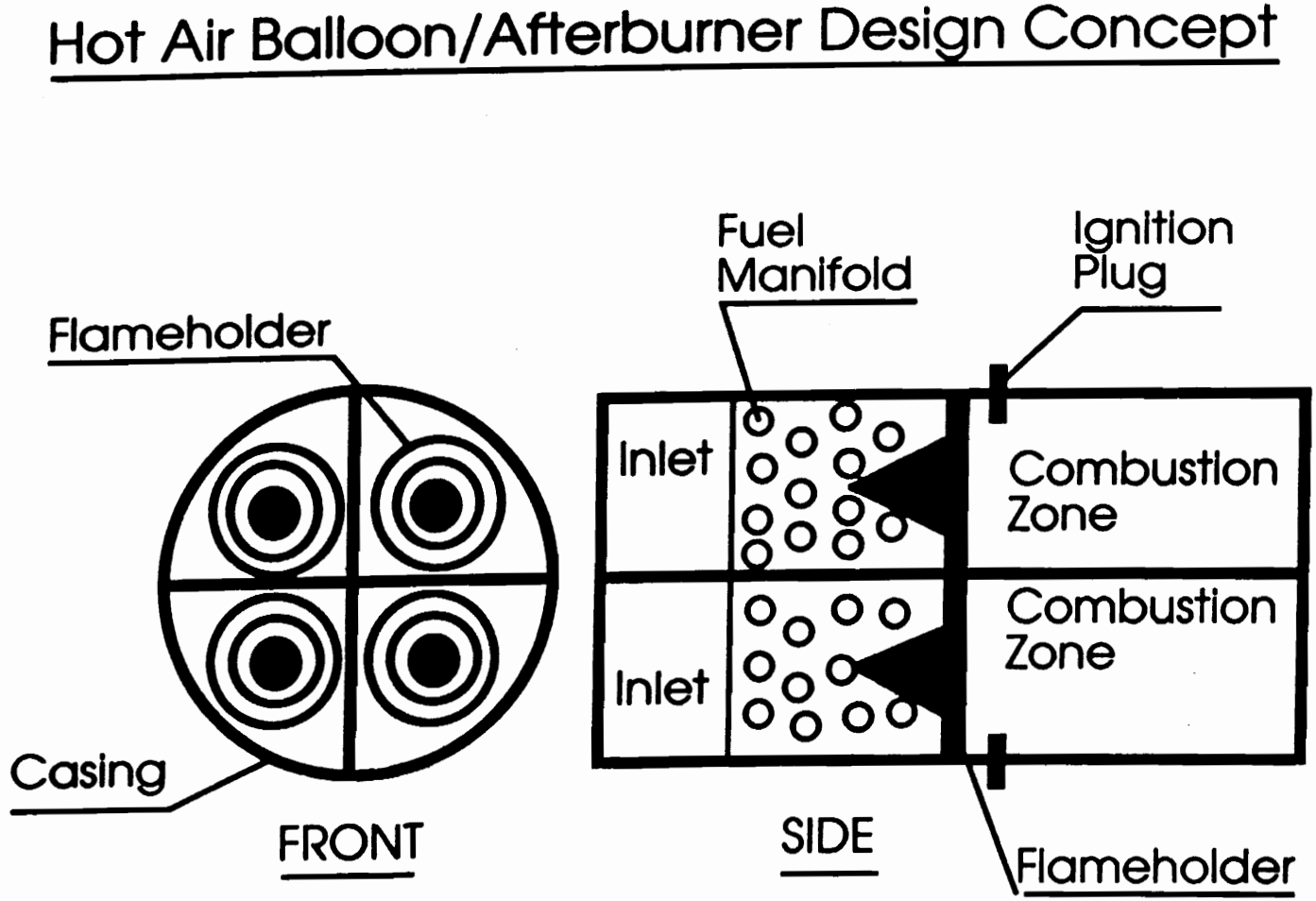

Figure 21. Hot Air Balloon/Afterburner Design Concept

mixing. Also, the wake of the flame holder produces a recirculating zone, Fig. 22 , where burning material recirculates. This recirculating zone of burning material functions as a continuous source of ignition for the combustion reaction to stabilize on the flame holder, preventing flame blow out. The ignition plug produces a continuous spark that initiates the combustion reaction during each cycle. The flame holder stabilizes the combustion reaction for the duration of the heating cycle. The geometry of the flame holder is based upon experimental research performed on flame holders in Ref (9). A problem with this type of a design is that the production and stabilization of a combustion reaction in a high velocity airstream requires an equivalence ratio very close to unity. Ignition is not possible for equivalence ratios less than approximately 0.8. A mass balance indicated that a flow rate of 9.3 kg/sec would flowing through the duct. The equivalence ratio indicated that to achieve a stoichometric fuel-to-air ratio with this mass of air required the injection of 0.596 kg/sec of fuel as indicated in Fig. 23. This combustion reaction was analyzed in Fig. 24 using STANJAN which is a thermal chemistry combustion analysis program. STANJAN is the Stanford University JANAF Thermochemical Tables computer program. STANJAN predicted that the combustion of propane and air at an equivalence ratio of 1 would produce a flame temperature of approximately 2267.0 (K). This level of temperature is high for distortion research would damage the jet engine research fan or compressor. Another disadvantage associated with this type of a design is that it requires restrictive control of the duct conditions to operate correctly. Afterburners do not have this many problems because the air temperatures are high to enhance fuel evaporation and ignition. Also, the amount of oxygen entering an afterburner is low from having been consumed in the main combustor of the engine. Therefore, less fuel is required to achieve a level of stoichometry in an afterburner.

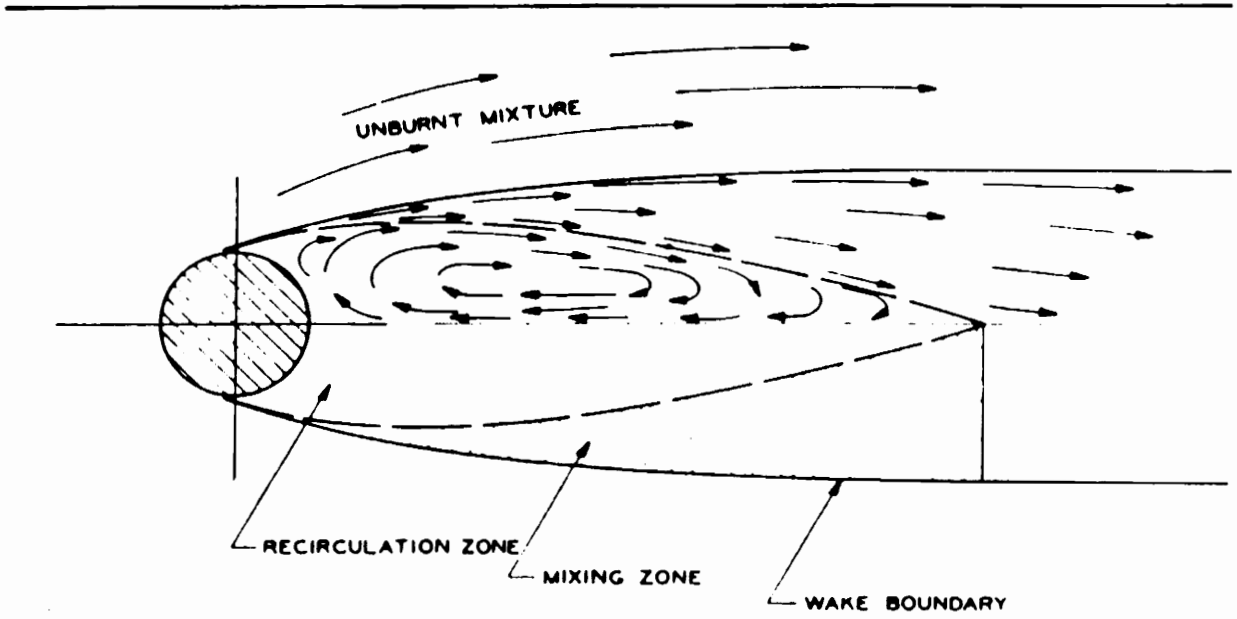

Flame stabilization region of a circular cylinder used as a bluff-body flameholder.

Figure 22. Flame Stabilization Region Of A Circular Cylinder Ref(9)

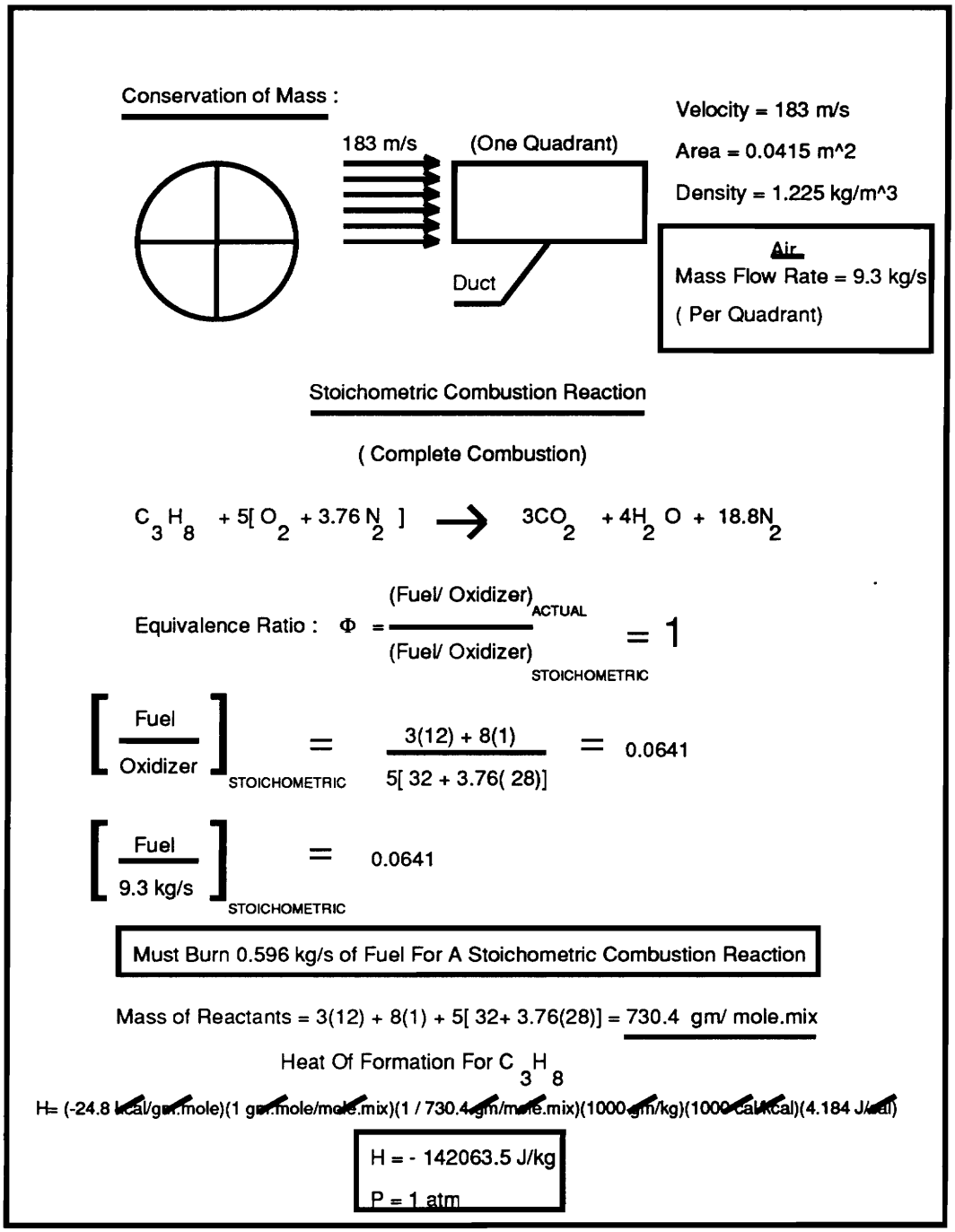

Figure 23. Afterburner Design Concept Stoichometry Analysis

```
Computed properties

Independent        population          element
   atom                                potential
     C          3.00000000E+00         -2.1198E+01
     H          8.00000000E+00         -1.2787E+01
     O          1.00000000E+01         -1.7174E+01
     N          3.76000000E+01         -1.3843E+01

Products at T =   2267.09 K    P =  1.000E+00 atmospheres

 species         mol fraction     mol fraction     mass fraction       mols*
                 in the phase      in mixture       in mixture

phase  1:  molal mass =   28.062 kg/kmol
 C                .68200E-16       .68200E-16       .29190E-16     1.77594E-15
 CH4              .29223E-16       .29223E-16       .16707E-16     7.60984E-16
 CO               .12498E-01       .12498E-01       .12475E-01     3.25447E-01
 CO2              .10271E+00       .10271E+00       .16108E+00     2.67455E+00
 C3H8             .38905E-47       .38905E-47       .61135E-47     1.01309E-46
 H                .46807E-03       .46807E-03       .16813E-04     1.21885E-02
 HO               .32037E-02       .32037E-02       .19416E-02     8.34247E-02
 H2               .33326E-02       .33326E-02       .23942E-03     8.67815E-02
 H2O              .14844E+00       .14844E+00       .95299E-01     3.86541E+00
 N                .22715E-07       .22715E-07       .11339E-07     5.91510E-07
 NO               .24630E-02       .24630E-02       .26338E-02     6.41378E-02
 NO2              .44149E-06       .44149E-06       .72383E-06     1.14966E-05
 N2               .72073E+00       .72073E+00       .71948E+00     1.87679E+01
 O                .31029E-03       .31029E-03       .17691E-03     8.07996E-03
 O2               .58442E-02       .58442E-02       .66641E-02     1.52185E-01

* Species mols for the atom populations in mols.

Mixture properties:   molal mass =   28.062 kg/kmol
   T =  2267.09 K          P = 1.0133E+05 Pa     V = 6.6291E+00 m**3/kg
   U = -.8138E+06 J/kg     H = -.1421E+06 J/kg   S =  .9701E+04 J/kg-K

Made    7 (T,P) iterations;   28 equilibrium iterations; v 3.89   IBM-PC


Sound speed (isentropic) =   889.8 m/s
```

Figure 24. STANJAN Combustion Analysis For Afterburner Design

The Source Burner Design Concept

The hot air balloon/afterburner design concept was not discarded but was modified for study to the source burner design concept shown in Fig. 25. It consists of a hollow 61 cm steel circular cylinder, 46 cm in diameter, that is subdivided into four quadrants with steel plates. Occupying the front of each quadrant is a centerbody that contains a fuel injector. Directly behind the centerbody is a hollow circular steel deflection cone that has an ignition plug mounted in its vertex. The burner operates by injecting the fuel from the end and into the wake of the centerbody. The fuel mixes with air and reaches the stagnation point on the deflection cone where the ignition plug is operating. Combustion occurs and the cone deflects the combustion gases into the airstream flowing through the duct. Unlike the hot air balloon/afterburner design concept, no flame holder was necessary to stabilize the combustion reaction. The combustion reaction would originate in a relatively closed and sheltered region where fuel residence times were long. This sheltered region was in the recirculation zone in the wake of the centerbody. This allowed adequate time for the fuel and air to mix before hitting the ignition plug on the stagnation point of the deflector cone. The centerbody itself acted as a flame holder. Analysis indicated that this particular design had a mixing problem. The problem was associated with the combustion gas penetration into the high velocity airstream. Fig. 26 is a conceptual sketch that shows the velocity vector triangles of the fluid mechanics associated with the mixing process. It indicates that the velocity components, of the combustion gases, are much less than the velocity of the airstream flowing through the duct. The relative velocity vector indicates small penetration into the airstream. Using conservation of mass, the design was altered by allowing some diffusion just before the injection of the hot combustion gases. This was accomplished by gradually increasing the

Source Burner Design Concept

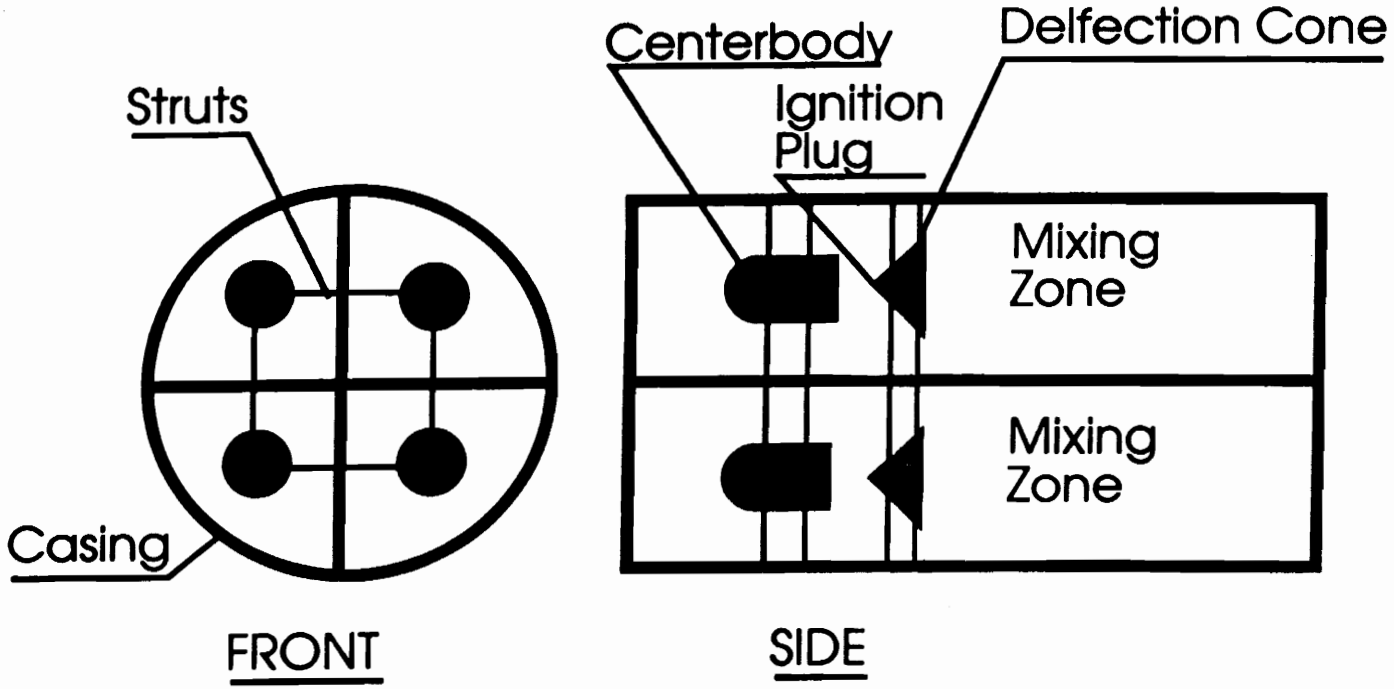

Figure 25. Source Burner Design Concept

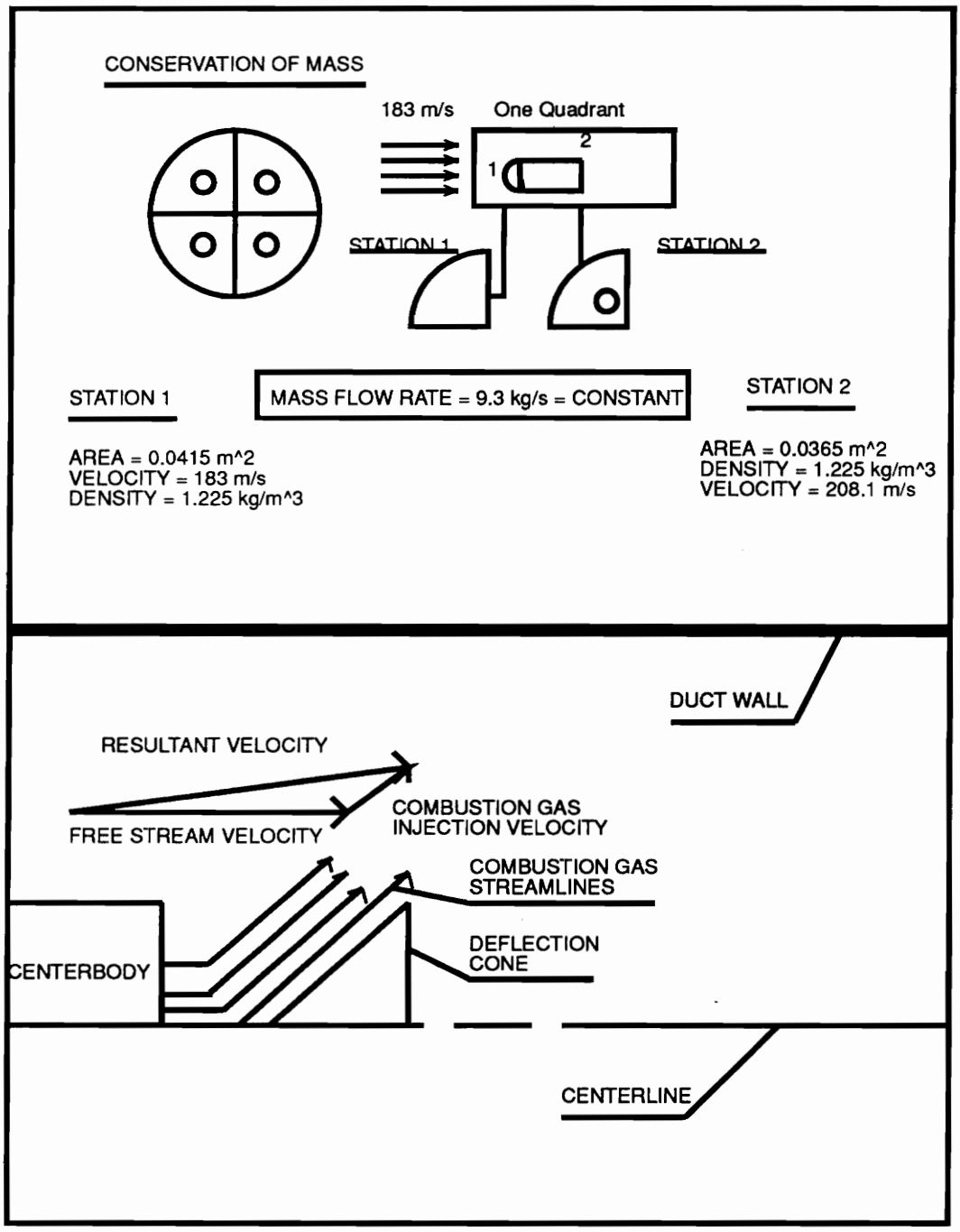

Figure 26. Velocity Triangles For Source Burner Design (conceptual)

cross sectional area, as the flow traveled through the duct, from the duct entrance up to the location where the combustion gases were injected. Fig. 27 shows the source burner redesigned. However, analysis still indicated that the velocity of the airstream flowing through the duct, was much greater than the velocity of the combustion gases. The fuel injector was modified to allow the mixing of some air with the fuel before it was injected into the wake of the centerbody. This would allow the fuel to burn faster, and it would also allow the fuel to be injected at a higher velocity. Unlike before, the fuel could not be injected at a higher velocity because it needed time to mix with air. Also, the flame speed of the combustion reaction was lower than the fuel injection velocity. This would cause the flame to extinguish before it left the deflection cone surface. These modifications led to the final and successful design concept.

The Final Design Concept

The final design concept is shown in Fig. 28. It consisted of a hollow steel cylinder, 91 cm in length and 46 cm in diameter, that was subdivided into four quadrants with steel plates. The thermal distortion generator was fabricated into two parts. The burner section, which constituted the front portion of the distortion generator, and the mixer section that composed the rear of the distortion generator. Occupying each quadrant in the burner section was a cylindrical centerbody that contained a fuel and air injector. An ignition plug, that produced a continuous spark, was mounted directly in front of the injectors, normal to the centerbody surface. Each quadrant was independent of the other; thus, the operator could control each quadrant as desired, in or out of phase with the others. The unsteady thermal distortion pattern was produced by injecting the fuel at a specified frequency. This was achieved by using computerized electronic solenoid valves that were

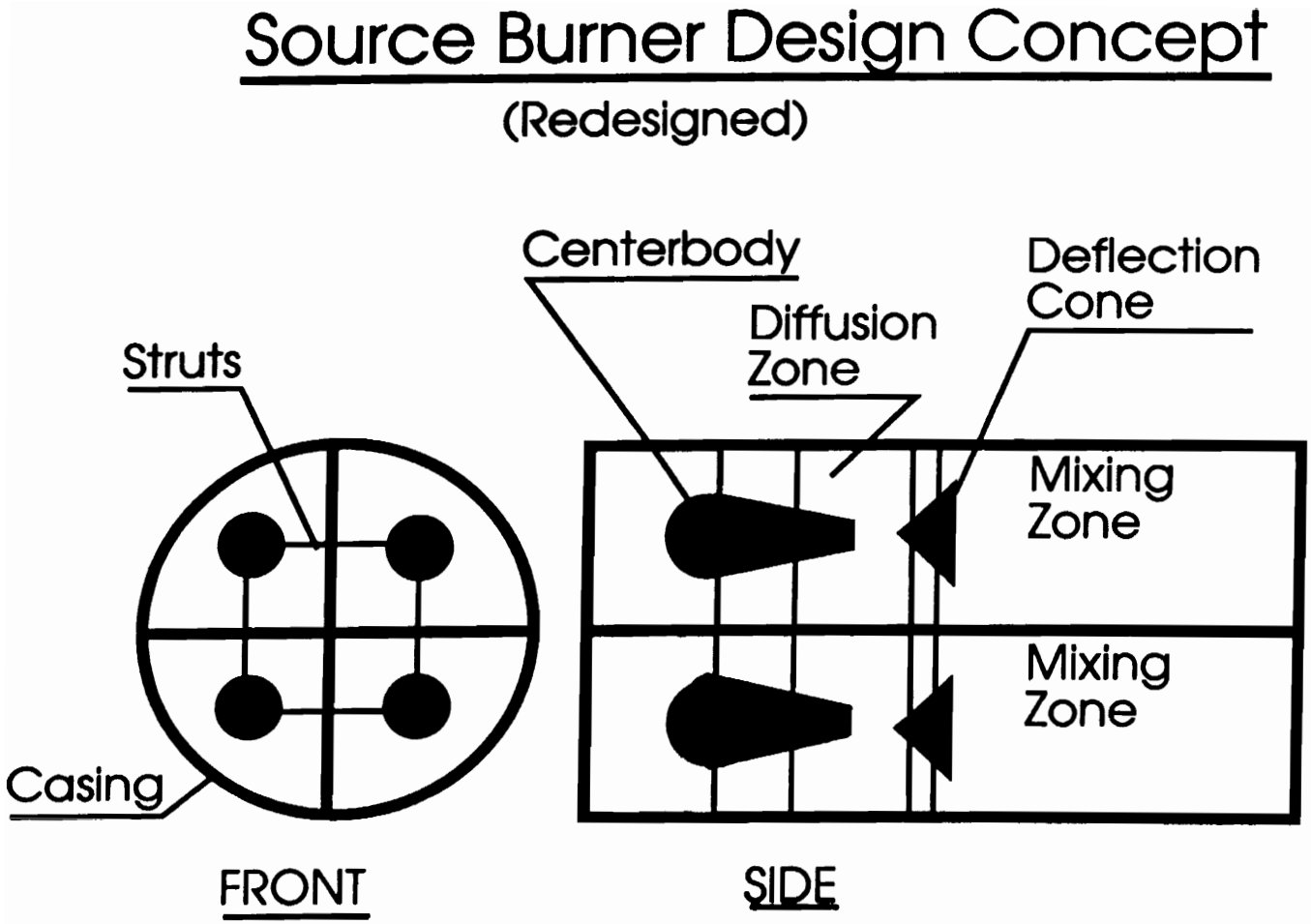

Figure 27. Source Burner Redesigned

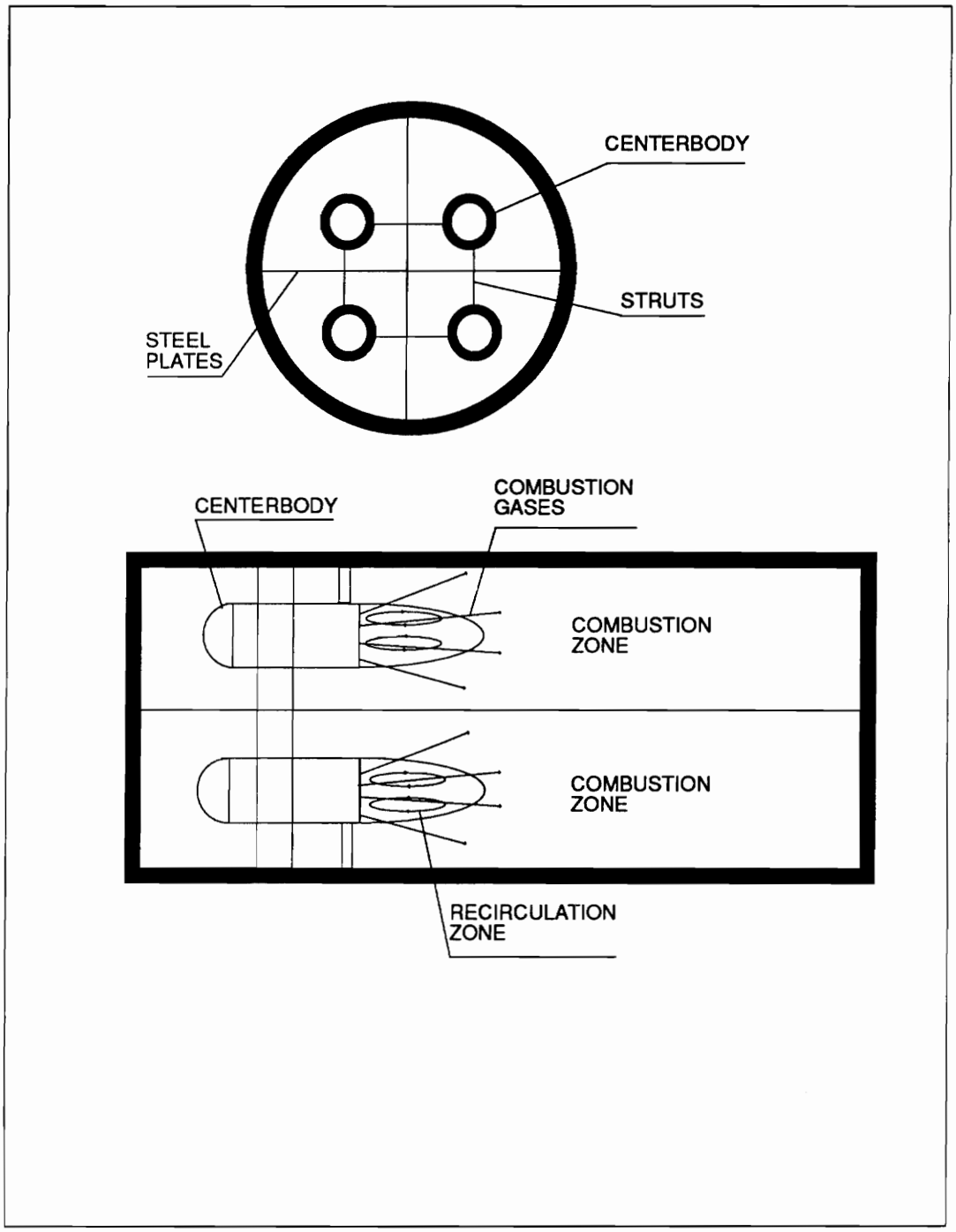

Figure 28. Final Design Concept

located external to the distortion generator in the fuel supply line. The combustion process occurred by injecting a fuel and air mixture into the wake of the centerbody from a relatively closed and sheltered region, where pressures were low and fuel residence times were high. The ignition plug which produced a continuous spark, would then ignite the fuel and air mixture trapped in the recirculating zone of the wake. This recirculating zone of burning material would then act as a continuous source of ignition to stabilize the combustion reaction behind the centerbody and to ignite the large quantities of fuel and air that were injected by the injector. The hot combustion gases entered the mixer section and mixed with the external flow. A uniform temperature rise of the airstream was achieved at the exit of the mixer. All four quadrants have their own centerbody, injector, ignition plug, and mixer. Thus all four quadrants can be independently controlled. This meets all of the design constraints and requirements for the thermal distortion generator.

XII. Final Design Concept Component Design and Analysis

The Outer Casing

The outer casing of the thermal distortion generator is shown in Fig. 29. It consists of two steel circular cylinders, 46 cm in diameter. The wall thickness, for both cylinders, is 5 mm. One cylinder is 30 cm in length and subdivided into four quadrants by use of steel plates. These plates have a thickness of 5 mm and are also 30 cm in length. The second cylinder is 61 cm in length and subdivided into four quadrants with steel plates. These plates are also 5 mm thick but 61 cm in length. The two cylinders have a flanges on both ends that allow them to be fastened together with four 6 mm bolts. When fastened together, the steel plates in both cylinders are aligned, as shown. Looking from either end of the assembly, the view is as indicated. The distortion generator is fabricated into two separate pieces for maintenance. It can be disassembled for routine cleaning and changing of the spark plugs.

The Fuel/Air Injector Nozzle Design

Fig. 30 shows the fuel and air injector nozzle. It consists of a hollow 2 cm steel, circular, right elbow with a threaded male and female end. Attached to the male end, of the elbow, is a circular diffuser that is 4 cm in length has an exit diameter of 2.5 cm. The contour of the inside wall of the diffuser is a gradual slope that increases the diameter from 2 cm, at the attached end, to 2.5 cm at the opened end. Mounted to the outside of the diffuser is a strut that supports a solid circular cone. This cone has a base diameter of 2 cm and an altitude of 3.5 cm. These dimensions produce a cone half angle of 16

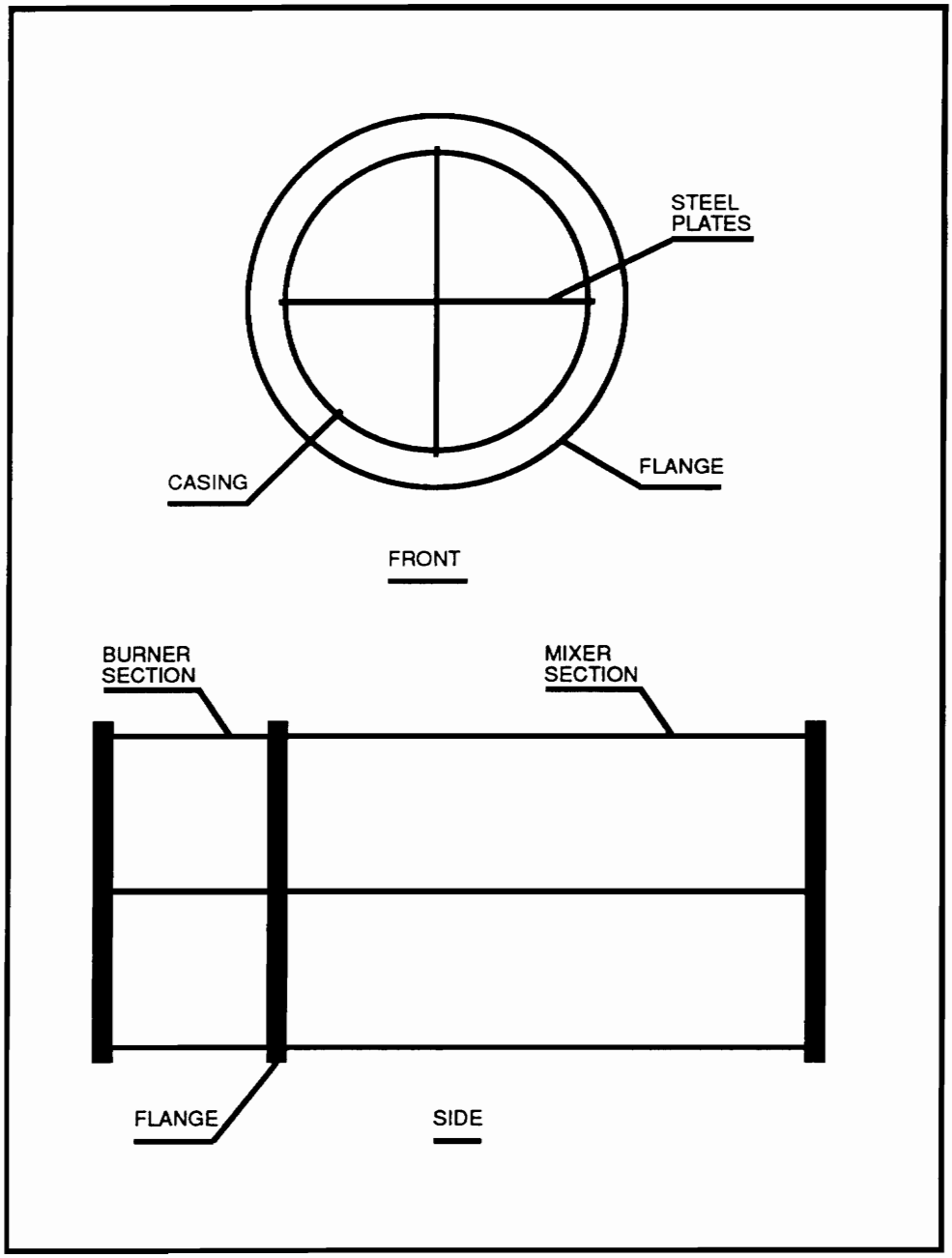

Figure 29. The Outer Casing

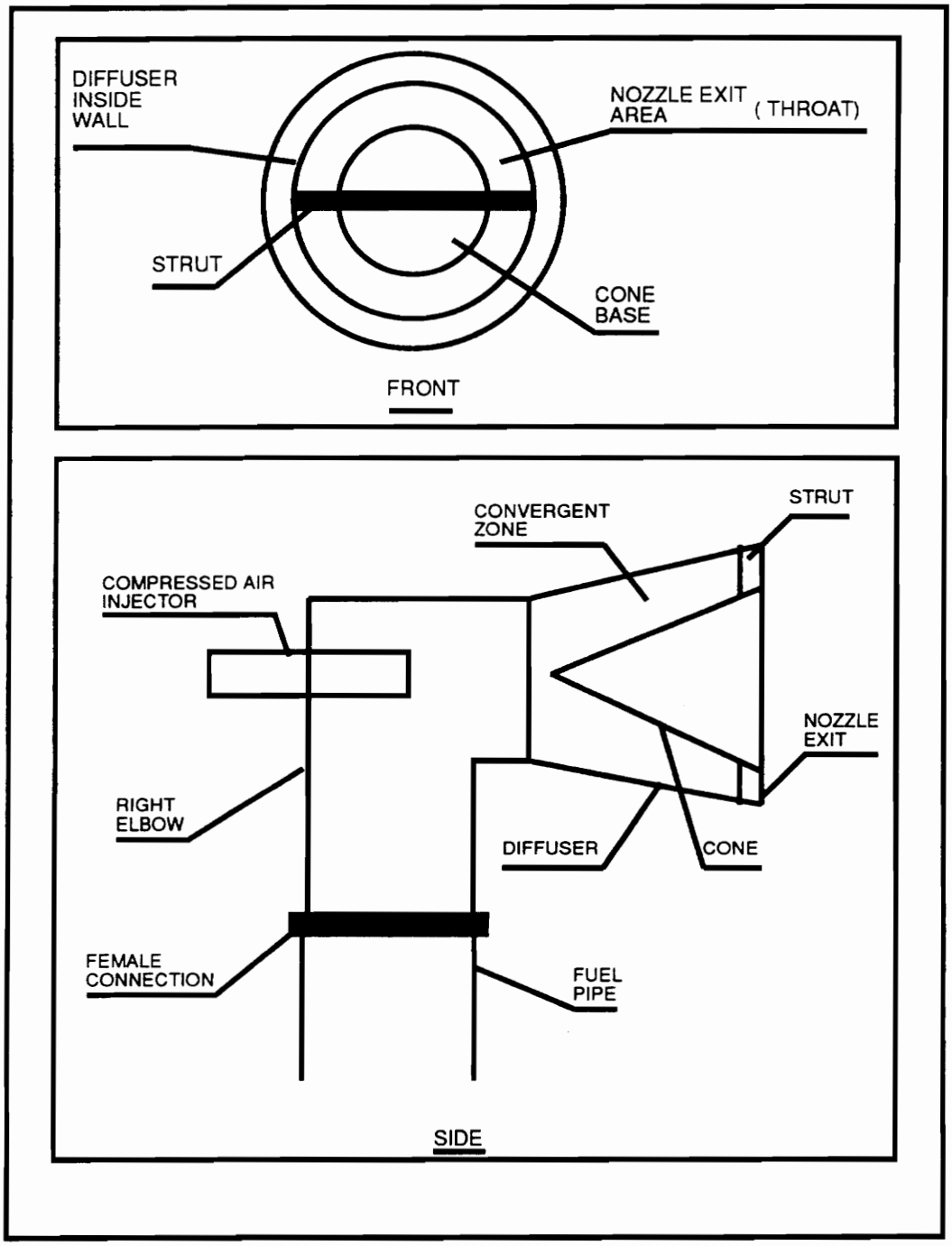

Figure 30. The Fuel/Air Injector Nozzle

degrees. The cone is positioned inside the diffuser such that its vertex points towards the 2 cm diameter opening. The centers of the cone base, the 2.5 cm diameter opening, and the 2 cm diameter opening all lie on the same centerline as shown. The presence of a cone, with these dimensions inside this particular diffuser, produces a convergent nozzle. A 4 cm long, 1 cm diameter steel tube is positioned inside the elbow. It is positioned in the bend of the elbow such that the center of the tube coincides with the centers of the cone and the two circular openings in the diffuser. The tube extends 2 cm into the elbow. On the female end of the elbow, a 2 cm diameter black iron pipe, is attached. The fuel enters the elbow from the 2 cm diameter black iron pipe. When the fuel reaches the bend, air is injected into the fuel by the 4 cm long, 1 cm diameter tube. The fuel and air begin to mix as they leave the elbow and enter the nozzle. The fuel and air mixture is then accelerated to a high velocity in the convergent section of the nozzle. The flow chokes at the throat, and then exits the nozzle at an angle of 16 degrees. The choking mass flow rate is 82.87 gm/sec.

The Centerbody Design

Figure 31 shows the centerbody geometry that contain the fuel/air injector nozzle and ignition plug. The aerodynamics and flow patterns of the centerbody are shown in Fig. 32. The centerbody is a hollow, stainless steel, circular cylinder, 8cm in diameter and 25 cm in length. The wall thickness of this cylinder is 2 mm. Closing one end of this cylinder is a solid aluminum semisphere that has a 4 cm radius. On the inside of the cylinder,

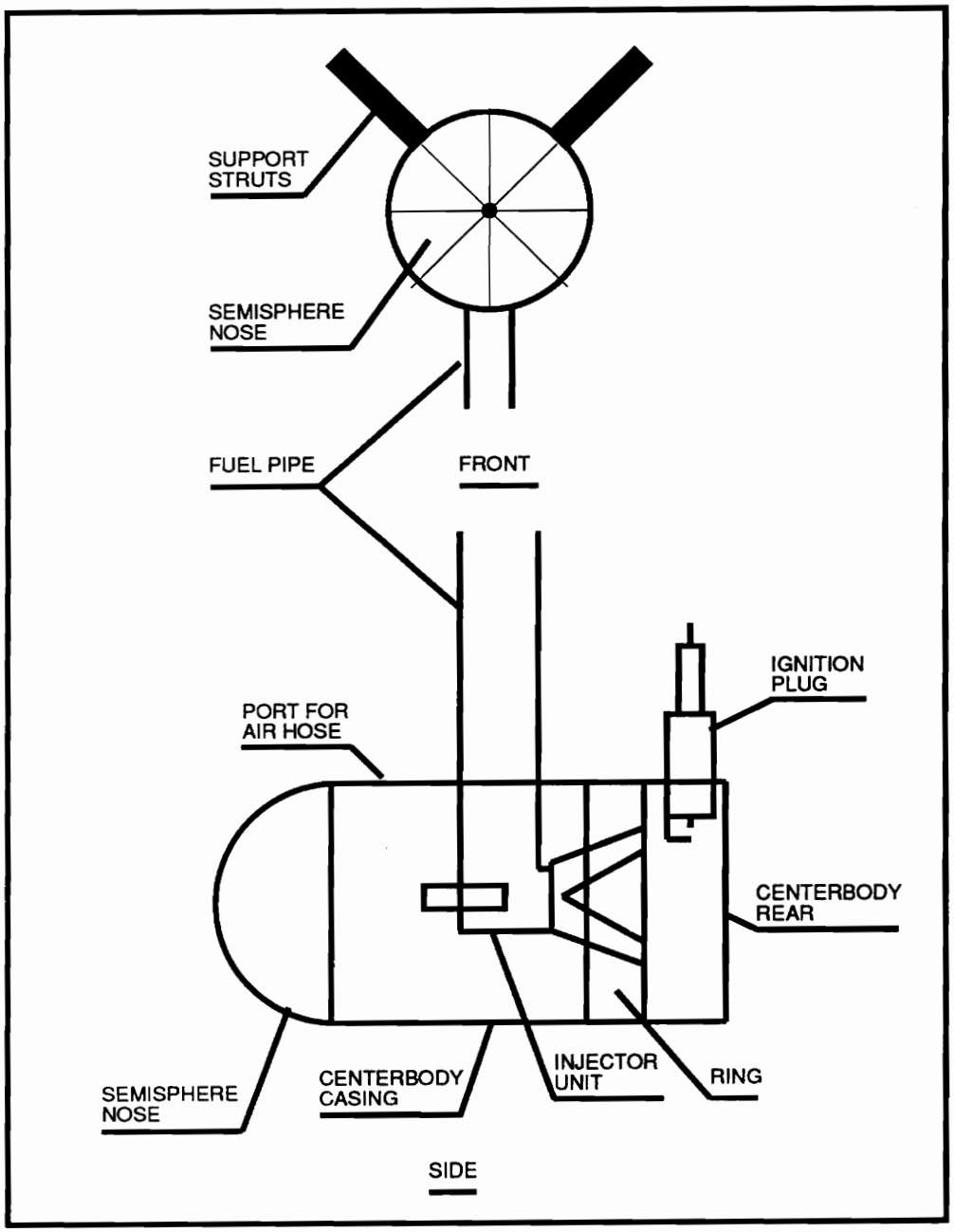

Figure 31. Centerbody Design

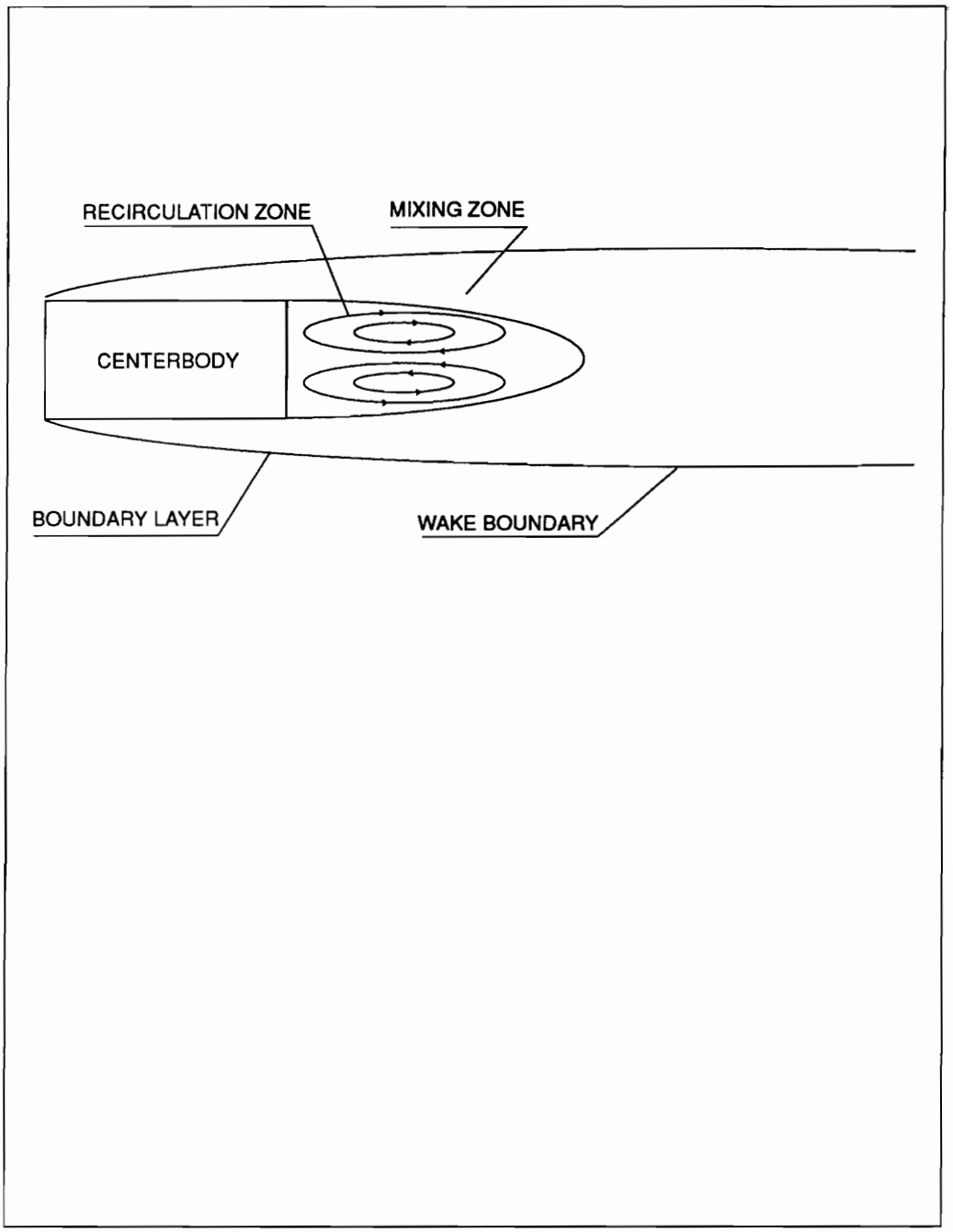

Figure 32. Centerbody Aerodynamics

2.5 cm from the open end, is a steel ring. This ring has a thickness of 2.5 cm and an inside diameter of 5 cm. The injector nozzle is mounted to the inside diameter of this ring such that the nozzle exit faces the open end of the cylinder. Also, the nozzle exit and the ring surface, facing the open end of the cylinder, are in the same plane. A spark plug is mounted perpendicular to the cylinder surface, 2 mm from the open end. Figure 31 shows the spark plug's position relative to the cylinder. The plug is positioned such that its electrodes extend into the recirculation zone of the wake of the centerbody.

The length of the recirculation zone necessary for stable combustion was determined by applying the Flame Stabilization Criterion to the design in Ref (9). The Flame Stabilization Criterion (FSC) is a theoretical boundary layer analysis that ensures stable combustion in a moving air stream, for a given bluff body geometry and duct flow conditions. It determines the length of the recirculation zone necessary to stabilize a combustion reaction in a moving airstream. It relates the length of a recirculation zone necessary for stable combustion to the geometry of the bluff body being used as a flame holder, the geometry of the duct containing the moving airstream, the velocity of the air stream, and the ignition time of the fuel being burned. The Flame Stabilization Criterion is typically used by gas turbine engine manufacturers when designing and analyzing gas turbine engine combustors and afterburners. The details of the analysis, with the Flame Stabilization Criterion, are displayed in Fig. 33.

A 2.5 cm diameter hole is drilled into the cylinder such that its center is 10 cm from the rear of the centerbody. This hole allows the black iron pipe to pass through the cylinder surface and attach to the female end of the elbow. Another hole is drilled into the cylinder surface that is 2 cm in diameter. It is positioned such that its center is 20 cm from the rear of the centerbody. This hole allows a rubber hose to pass through the cylinder surface and attach to the end of the 1 cm diameter tube. This hose will deliver a constant

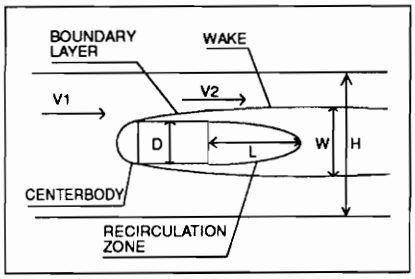

H - Height of the duct.

W - Width of the wake.

L - Length of the recirculation zone. (Necessary for Ignition)

V1 - Velocity of the approaching stream.

V2 - Velocity of the flow past the wake.

τ - Ignition time.

FLAME STABILIZATION CRITERION :

$$\frac{V2\tau}{L} = 1$$

$$\frac{V1\tau}{H} = \left[\frac{V1}{V2}\right]\left[\frac{L}{W}\right]\left[\frac{W}{H}\right]\left[\frac{V2\tau}{L}\right]^{1}$$

KNOWN VARIABLES	UNKNOWN VARIABLE
H = 0.23 m	L
W = 0.080713 m	
V1 = 183 m/s	
V2 = 208 m/s	
τ = 2.7E-4 s	

Solve For The Recirculation Zone Length Necessary For Ignition By Imposing The Flame Stabilization Criterion

2.7E-4 s = L/ 208 m/s

L = 0.05616 m
L = 5.616 cm

Figure 33. Flame Stabilization Criterion

flow rate of compressed air to the nozzle. The holes are drilled such that the centers of both holes, and the center of the spark plug, are on the same line as shown. Attached to the cylinder outside wall are two steel rectangular struts that are 5 mm thick and 13 cm in length. The struts are 6 cm in width. The struts are positioned as indicated in Fig. 31. Each strut is 135 degrees from the centerline of the holes drilled in the cylinder surface. This geometry positions the struts at a right angle to each other. These struts support the centerbodies in the quadrants of the burner section

The Complete Assembly

Fig. 34 shows the complete assembly of the experimental thermal distortion generator. The four centerbodies are mounted in the quadrants of the burner section. The steel struts hold the centerbodies in position. The tips of all the semispheres of the centerbodies are in the same plane as the burner inlet. Three holes are drilled on the same line that is at 45 degrees in each quadrant in the outer casing. The first hole is 2 cm in diameter and its center sits 5 cm from the burner inlet. The second and third holes are both 2.5 cm in diameter and their centers sit at 15 and 25 cm from the burner inlet. The first hole allows a rubber air hose to run and attach to the injector nozzle in each of the quadrants. The second hole allows the fuel pipe to attach to each injector nozzle. The third hole is to allow an ignition wire to be attached to each spark plug on the centerbody.

The Ignition System

The ignition system that was designed and developed for the thermal distortion generator is an electronic ignition system. It consists of two 12 volt power supplies, a

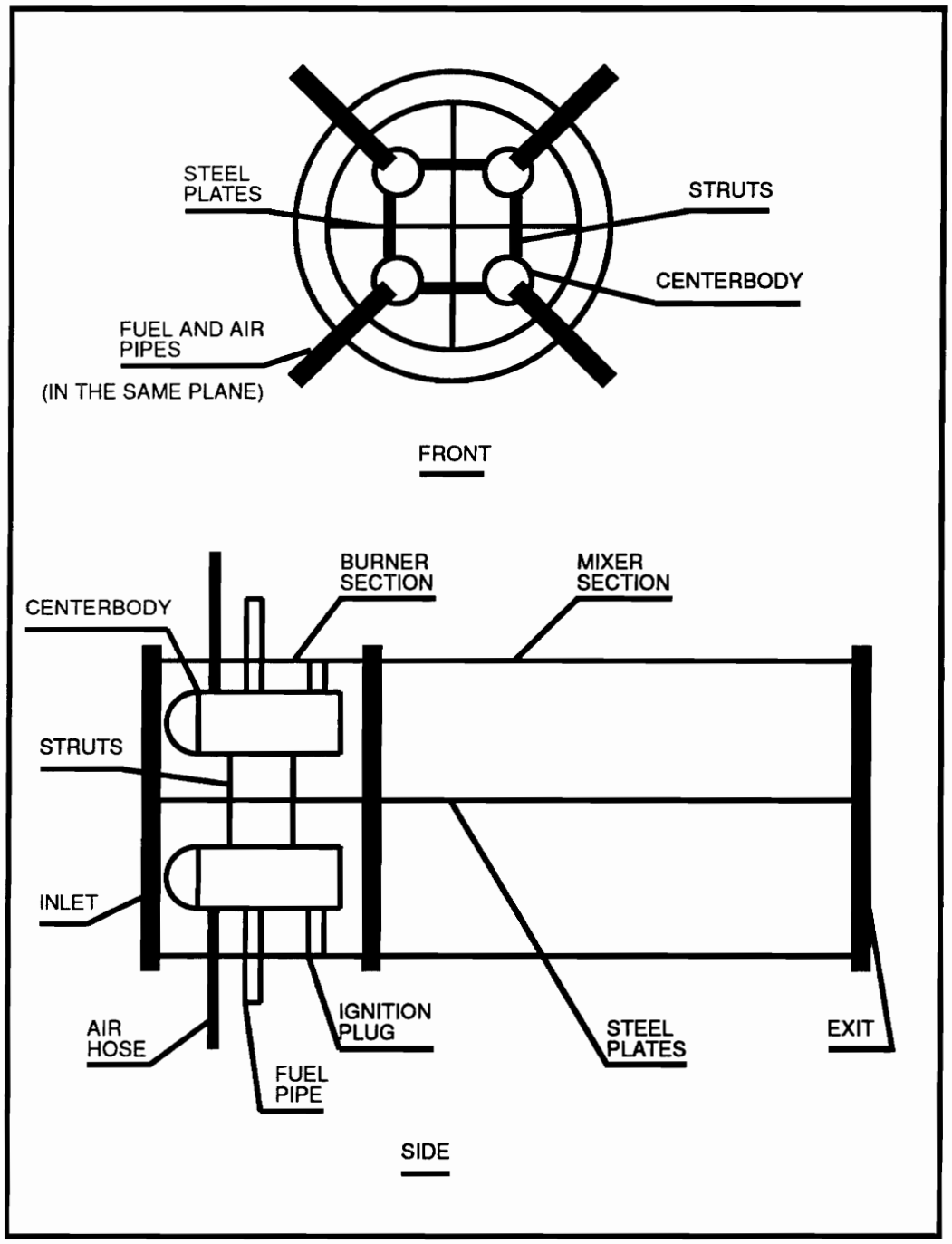

Figure 34. The Complete Assembly

signal generator, four capacitive discharge ignitors, and four automobile 12 volt ignition coils. The specifications of all the components are provided in Appendix F. A wiring diagram of the electrical circuit that was designed, developed, and put into operation for the distortion generator is shown in Fig. 35. The circuit is designed to operate four individual spark plugs off of a common ground. The circuit produces a continuous spark in the gap of four independent spark plugs. The two 12-volt power supplies provide power for the charging of four capacitive discharge ignitors. The signal generator replaces what would normally be a set of ignition points on an automobile, by producing an alternating current. This alternating signal causes the capacitive discharge ignitor to discharge its capacitor bank. The current enters the primary side of the ignition coil where the voltage is stepped up to 49,500 volts by the secondary windings. This produces a spark. All the negative leads from the two power supplies, the capacitive discharge ignitors, and the low side of the ignition coils are tied together as a common ground. This allows four ignition plugs to operate off of a common ground. This common ground is the outer casing of the thermal distortion generator.

Fuel Delivery and Control

The propane fuel is stored in two 1.5 kg cylinders and delivered from the tanks to the burner by 2 cm diameter black iron pipes. A left handed thread brass nipple attaches directly to the valves on each of the propane tanks. This brass nipple is 0.6 cm in diameter and attaches to a 0.6 cm to 2 cm reducer. The 2 cm end of the reducer attaches to the center of a 2 cm tee junction. From the tee junction, the necessary plumbing delivers the propane fuel to the distortion generator. Each tank provides fuel for two quadrants in the distortion generator. Thus, four fuel lines are connected to the distortion generator, one

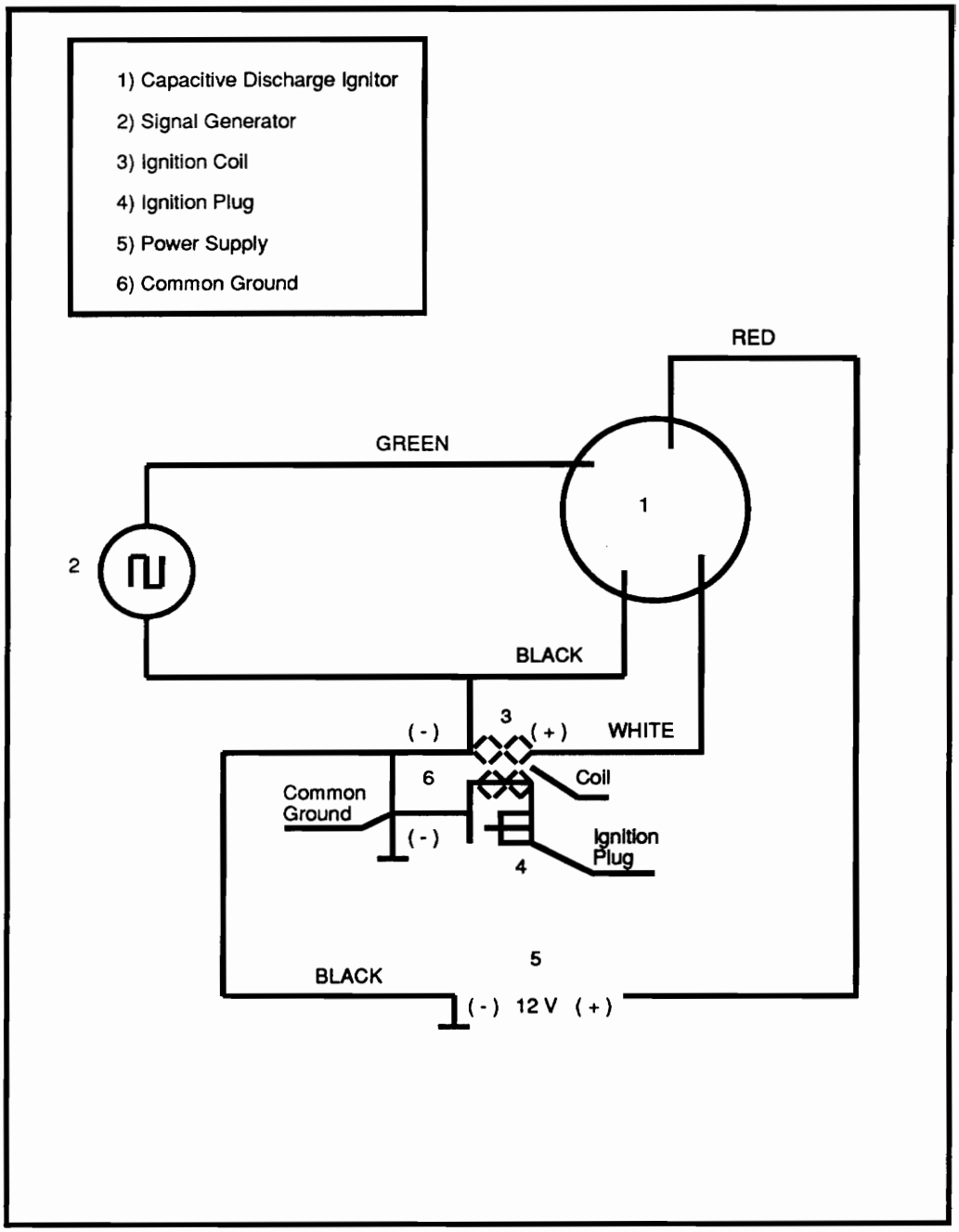

Figure 35. Ignition System Electronic Circuit

fuel line per quadrant. Each fuel line terminates with a 2 cm electronic solenoid valve just before its attachment to the distortion generator. This electronic solenoid valve opens when it is energized by an electric current. Attached directly to each solenoid valve exit, is a 2 cm regulator gate valve. The exit of each gate valve connects directly to a centerbody in the quadrants of the distortion generator with 2 cm black iron pipe. The function of the two storage tanks is to supply the fuel at a high pressure and flow rate. The black iron pipe delivers the fuel to the respective quadrants. The function of the solenoid valves are to open and close, at a specified frequency, to control the fuel discharge to their respective injector nozzles. The function of the gate valve is to regulate the amount of fuel delivered to the injector. This allows the fuel-to-air ratio to be varied and also allows control of the combustion temperature. The gate regulator valves are manually controlled by the operator. The solenoid valves are computer controlled. Special computer programs are written to send electronic signals to solid state relays. These solid state relays are connected in series with the circuit that delivers the current to the solenoid valves. These solid state relays operate by closing and completing the electronic circuit when an electric current energized them. The circuit is broken when the energizing signal disappears. This energizing signal is produced by the computer. Several computer programs are written in BASIC to energize certain solid state relays at certain frequencies and at certain times. This translates into the opening and closing of certain solenoid valves at certain frequencies and at certain times. This corresponds to the injection of fuel into particular quadrants at certain times and frequencies. Thus, the unsteady or time varying distortion pattern is produced.

XIII. DESCRIPTION OF TEST FACILITY

The test facility used for the experimental thermal distortion generator is located at the Virginia Polytechnic Institute and State University Airport. It is now part of both the Mechanical Engineering Department's Turbomachinery and Propulsion Research Laboratory and the Chemically Reacting Flow Laboratory. A special combustion test cell was designed and developed to operate and test the experimental thermal distortion generator. A basic layout of the test cell is shown in Fig. 36. The test cell is rectangular in shape, having a length of 7.6 m, a width of 3.8 m, and a height of 4.6 m. A rectangular window, made of lexane glass, is installed in the wall to allow sight into the test cell from the adjacent control room located in the Chemically Reacting Flow Laboratory. This allows remote control of the distortion generator. This window is 91 cm long, 46 cm wide, and 0.6 cm thick. It is installed such that its center is 1.2 m off of the test cell floor and 2.1 m from the cell's back wall. The lexane glass is shatter proof and can stop a 45 caliber hand gun bullet at 4.5 meters away. In addition to allowing sight into the test cell from the adjacent control room, the window provides protection against shrapnel and debris in the event of an explosion.

A General Electric, single stage, subsonic, axial flow compressor is anchored to the floor in the center of the test cell. This compressor has a diameter of 46 cm and is driven by a 50 HP General Electric electrical motor. This compressor stands such that its center is 91 cm off of the test cell floor. The top speed of this compressor is 3600 RPM which produces a blade tip speed of 86.3 m/s that equals Mach 0.25 at sea level. The axial fluid velocity, under experimental operating conditions, is 25.3 m/s at 2900 RPM. A circular exhaust duct, 46 cm in diameter and 3.6 m in length, passes through the back wall of the test cell. It is positioned such that its center is 91 cm off of the test cell floor and

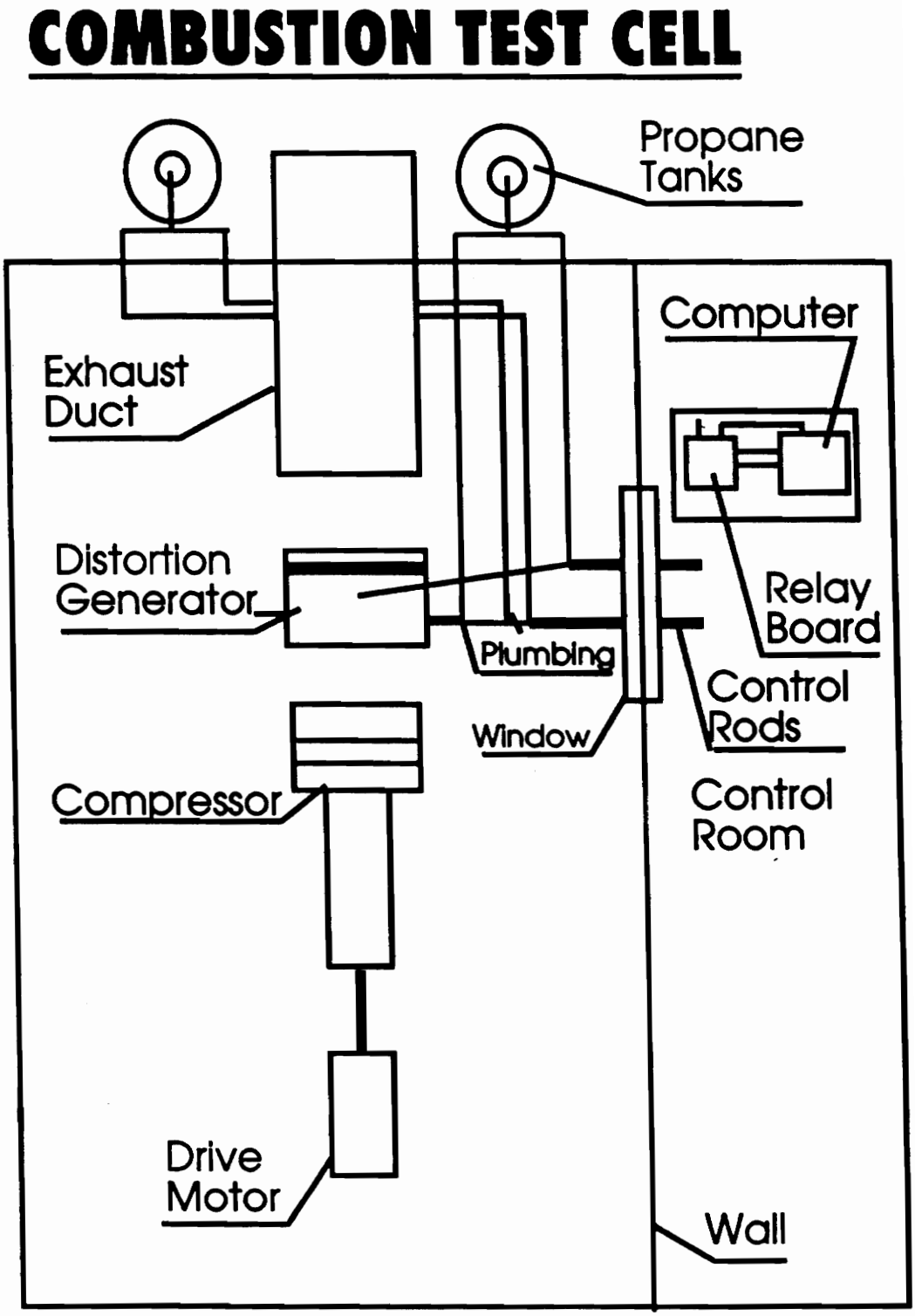

Figure 36. Combustion Test Cell

aligned with the compressor exit. This exhaust duct extends 2.1 m into the test cell and 1.2 m out the back wall outside the test cell to the atmosphere. This produces a 1.5 m test section between the compressor exit and the exhaust duct inlet. It is set up such that the test section is directly in front of the window installed in the wall. The purpose of the compressor is to serve as a blower. The distortion generator is positioned in the test section such that the compressor blows air through it. This simulates the distortion generator's attachment to the inlet of a fan or compressor. The exhaust gases exit the distortion generator and enter the exhaust duct where they discharge to the atmosphere out the rear of the duct.

Two 1.5 kg cylinders of propane, each containing 91 liters of liquid propane, sit on both sides of the exhaust duct outside the back of the test cell. Black iron pipes, all 2 cm in diameter, deliver the propane from the tanks, to the solenoid and regulator valves located in front of the window inside the test cell. Black iron pipes then deliver the propane, from the regulator valves to the respective quadrants in the distortion generator. Each tank supplies fuel for two quadrants.

The control room is located in the Chemically Reacting Flow Laboratory. Four control rods extend from the control room, through the wall, to the regulator gate valves. There is one control rod for each gate valve. These regulator gate valves are manually controlled by turning the rods that open and close the valve. Thus, the propane flow rate, fuel to air ratio, and flame temperature are all simultaneously controlled with these valves. The computer and solid state relay board, that control the solenoid valves, are also located in this room. Special computer codes are developed that send electronic signals to the solid state relays. These are the same relays that operate the solenoid valves. This allows the liberty to create any distortion pattern that is consistent with four quadrants. It also allows this pattern to be cycled at any frequency within the limits that the solenoid valve

can operate. All that is required of the operator is to alter one line in the computer code. The power supply, for all four solenoid valves, has an emergency cutoff switch so the entire fuel system can be cut off at any moment. The compressor speed is controlled by a rheostat, located in the control room. The motor, that drives the compressor, has its power supplied by a motor generator box located in the test cell. The rheostat controls the power delivered from the motor generator box to the motor that drives the compressor.

The instrumentation used in obtaining thermal distortion data consists of an Edison 286 computer and a steel thermocouple rake. A schematic of the thermocouple rake is shown in Fig. 37. The rake is 46 cm in diameter and has eight hollow spokes that are 1cm in diameter. Each spoke has two 2 mm holes drilled in its surface. The location of the centers of these holes, on all of the spokes, is 9cm and 18 cm from the center of the rake. OMEGA chromel alumel type K thermocouple wire, 0.127 mm in diameter, runs into each spoke. A thermocouple junction is formed , at each hole, on each spoke, creating a total of 16 thermocouples on the rake. The response time of each thermocouple is 0.005 seconds. The error associated with the measurements is plus or minus 2.2 degrees (C), plus or minus 75% of that error. The thermocouple rake is mounted in the exhaust duct and the wires attached to the computer's external input/output circuit board. The rake is designed so that it can be positioned at several stations in the exhaust duct. The rake is held into place, at each station, with two 6 cm bolts. The ability of the rake to be positioned at several stations in the exhaust duct allows temperature measurements to be made at various stations. This provides the opportunity to examine how thermal distortion patterns changed with distance in the exhaust duct.

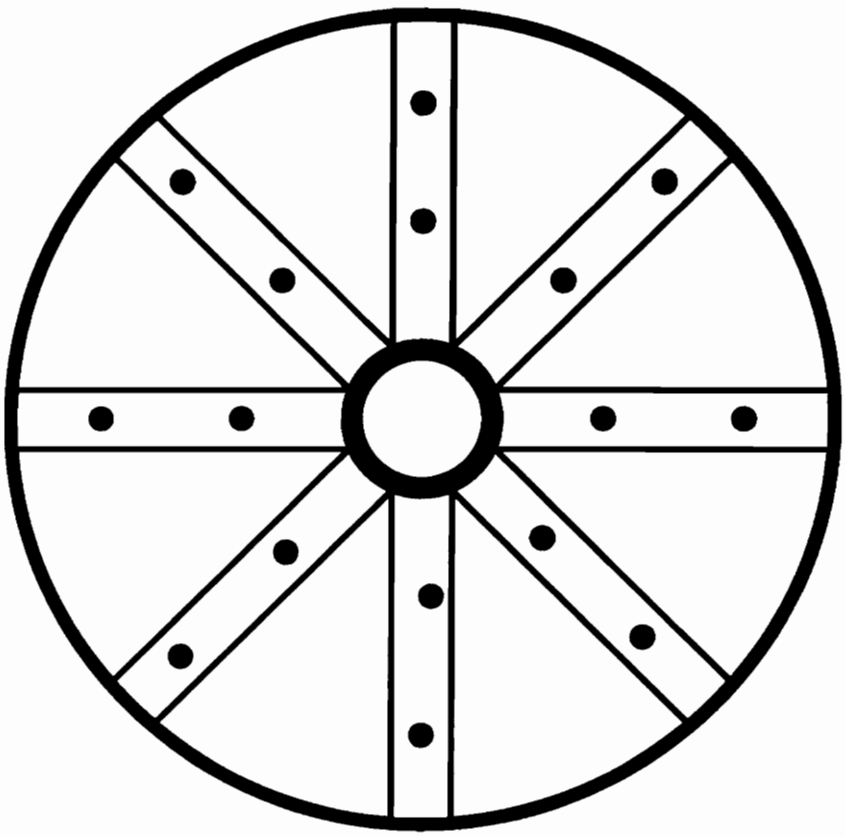

Figure 37. Thermocouple Rake

XIV. The Experimental Prototype

An experimental prototype was fabricated first to evaluate the overall performance of the design. Fig. 38 shows the experimental prototype burner. It consisted of a hollow 61 cm steel cylinder. The diameter of this cylinder was 22.8 cm. This generated a cross sectional area that was equal to the area of a circular quadrant with a radius of 23 cm. Thus, the same mass flow that traveled through this cylinder was equal to the same mass flow that traveled through a circular quadrant that had a 23 cm radius, provided that the air velocity and density remained constant. A centerbody and fuel injector nozzle, as described in the Final Design Component Design and Analysis section, was welded at one end of the cylinder with two struts. The struts were welded 180 degrees from each other. Three holes are drilled with the same dimensions and locations in the cylinder wall on one side, as described in the Complete Assembly section. The burner was mounted in the test section of the test cell where a fuel pipe, an air hose, and an ignition wire are attached. A video tape of the burner's operation indicated that the combustion reaction was very robust and stable. Based upon the promising performance displayed by the experimental prototype, the final thermal distortion generator was fabricated and operated.

Figure 38. The Experimental Prototype

XV. EXPERIMENT

An experiment was conducted to examine the dynamic distortion patterns produced by the distortion generator. The purpose of the experiment was to observe the thermal distortion patterns and how they changed with time and distance downstream of the distortion generator. The data was obtained from the thermocouple rake located in the exhaust duct. The data points that are plotted at each circumferential location represent the average temperature read by the two thermocouples on each spoke. Temperature measurements were sampled every 0.25 seconds while the distortion generator was operating. This allowed the temperature gradient to be observed at different points in time. Each quadrant produced temperature rises for 0.5 seconds and remained off for 0.5 seconds, completing the one Hz cycle. The axial fluid velocity under experimental conditions was 25.3 m/s. Temperatures were measured at three locations in the duct. These locations were six, nine, and twelve feet from the burner exit respectively. Data obtained at these locations for any particular distortion pattern gave information about how the distortion pattern was changing with time and distance for that particular pattern. It was necessary to know how the distortion pattern appeared twelve feet from the burner exit. This is typically where the burner sits from the aerodynamic interface plane (AIP), which is the engine's inlet. Static and total pressure measurements were also taken with a pitot tube, static pressure tap, and a manometer. The purpose of taking these pressure measurements was to determine the air velocity, the pressure distribution, and the loss in total pressure at the aerodynamic interface plane.

RESULTS

Pressure measurements were taken once, twelve feet from the burner exit, where the aerodynamic interface plane would be located. These measurements were taken with the burner not in operation to determine the loss in total pressure due to blockage and skin friction in the distortion generator and exhaust duct. The pitot tube was positioned at each 45 degree sector of the exhaust duct exit and extended 9.5 cm into the duct. Static pressure measurements were taken every 90 degrees around the exhaust duct exit with static pressure taps. The data are presented in graphical format to "see" the different distortion patterns and pressure profiles. Eight different dynamic thermal distortion patterns were produced by the distortion generator. Temperature data was obtained for each of these thermal distortion patterns at three locations in the exhaust duct. These locations were six, nine, and twelve feet from the burner exit. The data was plotted in three dimensions: circumferential location verses time verses the nondimensional temperature ratio. The data plotted in this format allows the dynamics of each thermal distortion pattern to be visualized. It also allows visualization of how the thermal distortion pattern is changing with time and distance through the exhaust duct. The temperature ramps associated with the peak temperature of all the thermal distortion patterns are also plotted at six, nine, and twelve feet from the burner exit. The temperature ramp data provides information about the rate of change of temperature produced by each distortion pattern. The eight dynamic thermal distortion patterns generated for this experiment are as follows :

1) One quadrant

2) Two adjacent quadrants in phase

3) Two adjacent quadrants out of phase

4) Two opposing quadrants in phase

5) Three quadrants in phase

6) Three quadrants out of phase

7) Four quadrants in phase

8) Four quadrants out of phase

Figure 39 indicates the total and static pressure distribution around the circumference of the AIP, twelve feet from the burner exit. Figure 40 through Fig. 47 indicate the temperature profiles for the unsteady temperature distortion patterns selected for the experimental demonstration. The temperature ramps associated with the peak temperatures of these distortion patterns are located in Appendix C. Measurements are taken at three different stations as indicated, six, nine, and twelve feet from the burner exit. All the unsteady distortion patterns are cycled at a frequency of one Hz. The data indicates what each distortion pattern looks like through one cycle.

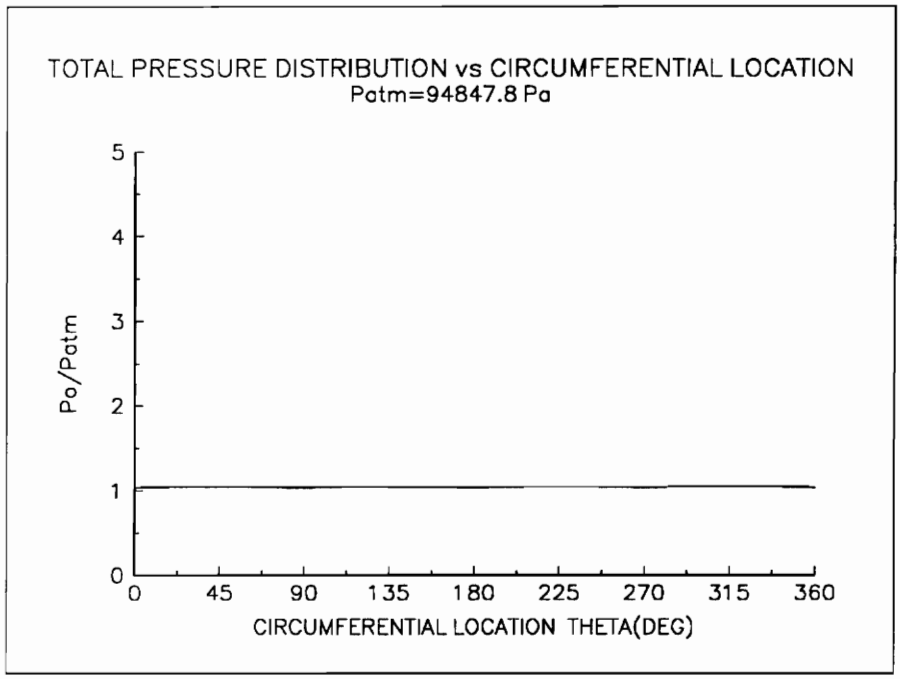

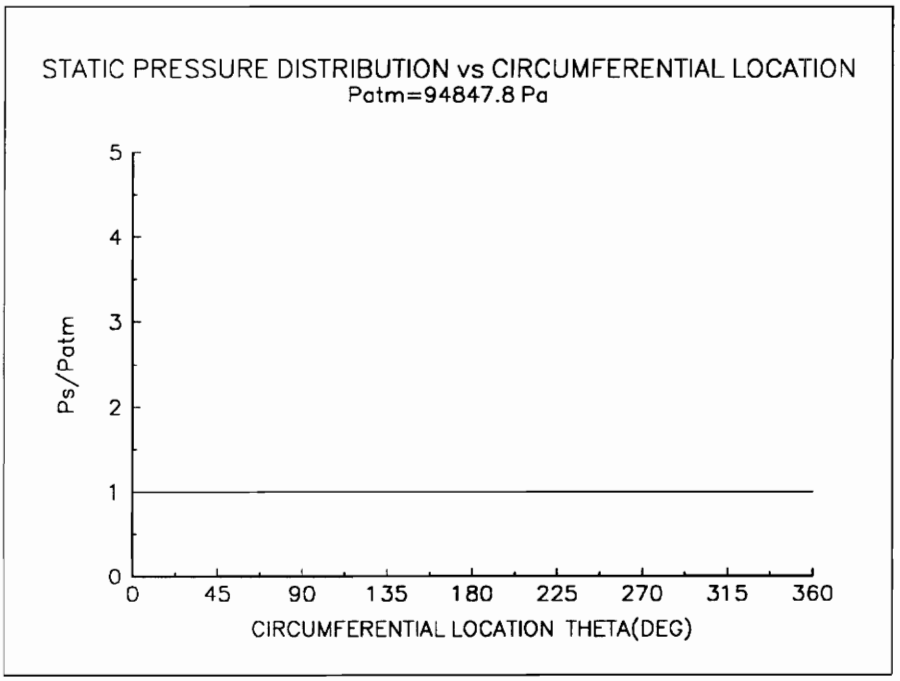

Figure 39. Total And Static Pressure Distribution

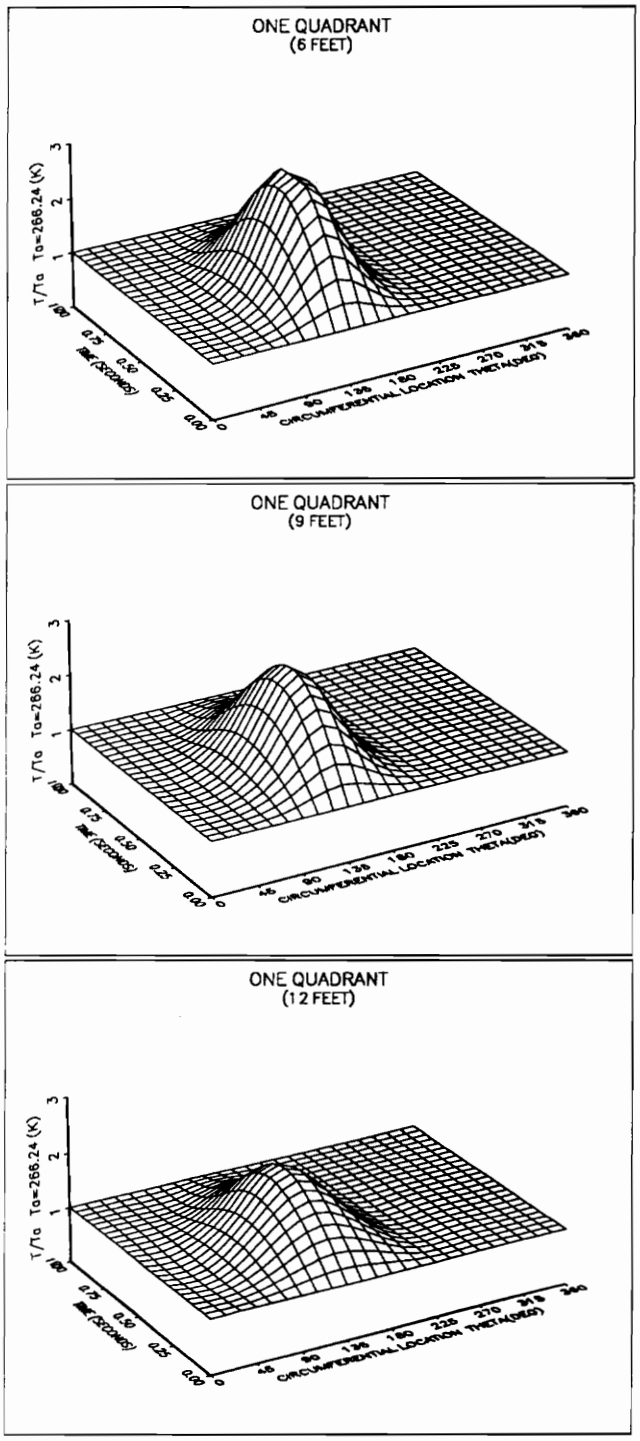

Figure 40. Temperature Distribution(One Quadrant)

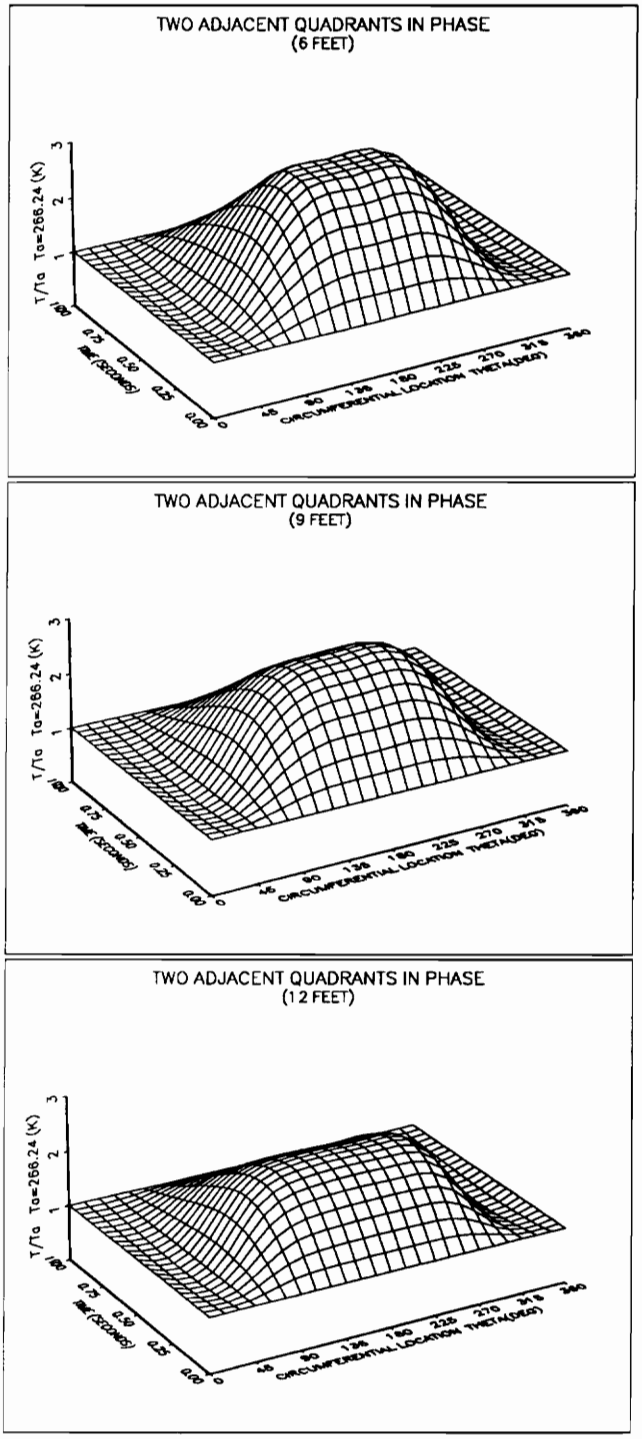

Figure 41. Temperature Distribution(Two Adjacent Quadrants In Phase)

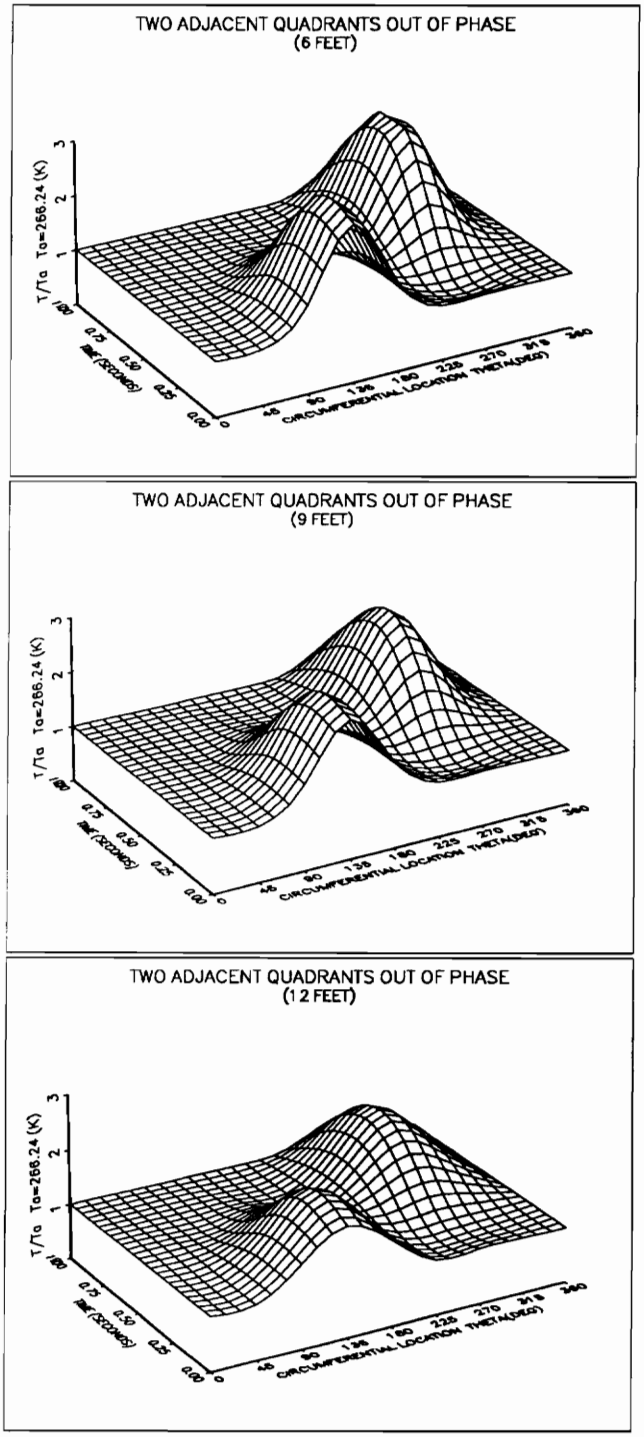

Figure 42. Temperature Distribution(Two Adjacent Quadrants Out Of Phase)

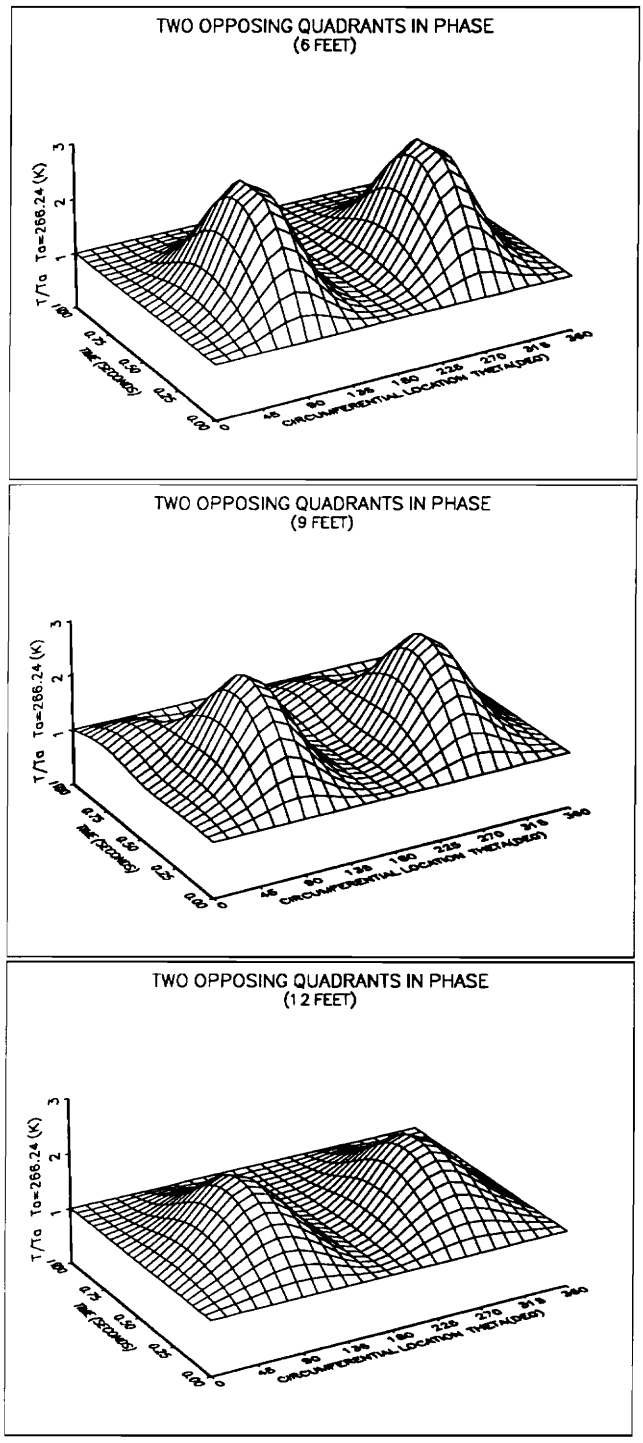

Figure 43. Temperature Distribution(Two Opposing Quadrants In Phase)

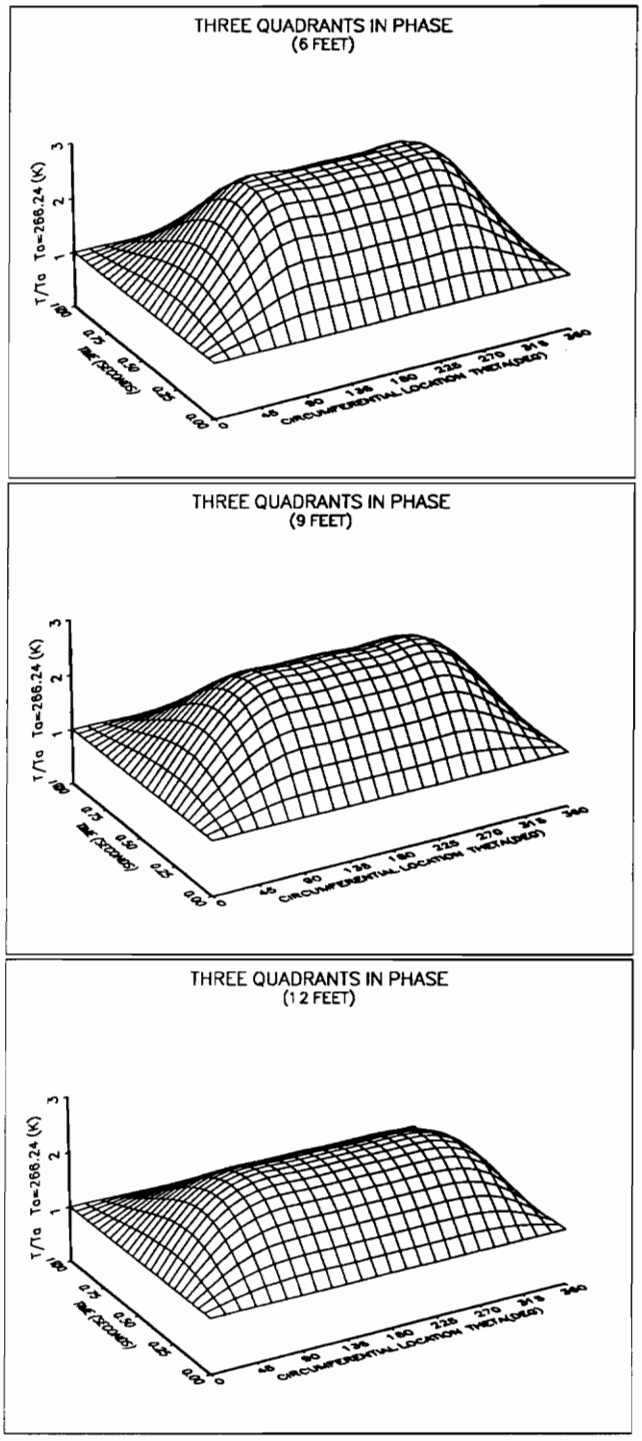

Figure 44. Temperature Distribution(Three Quadrants In Phase)

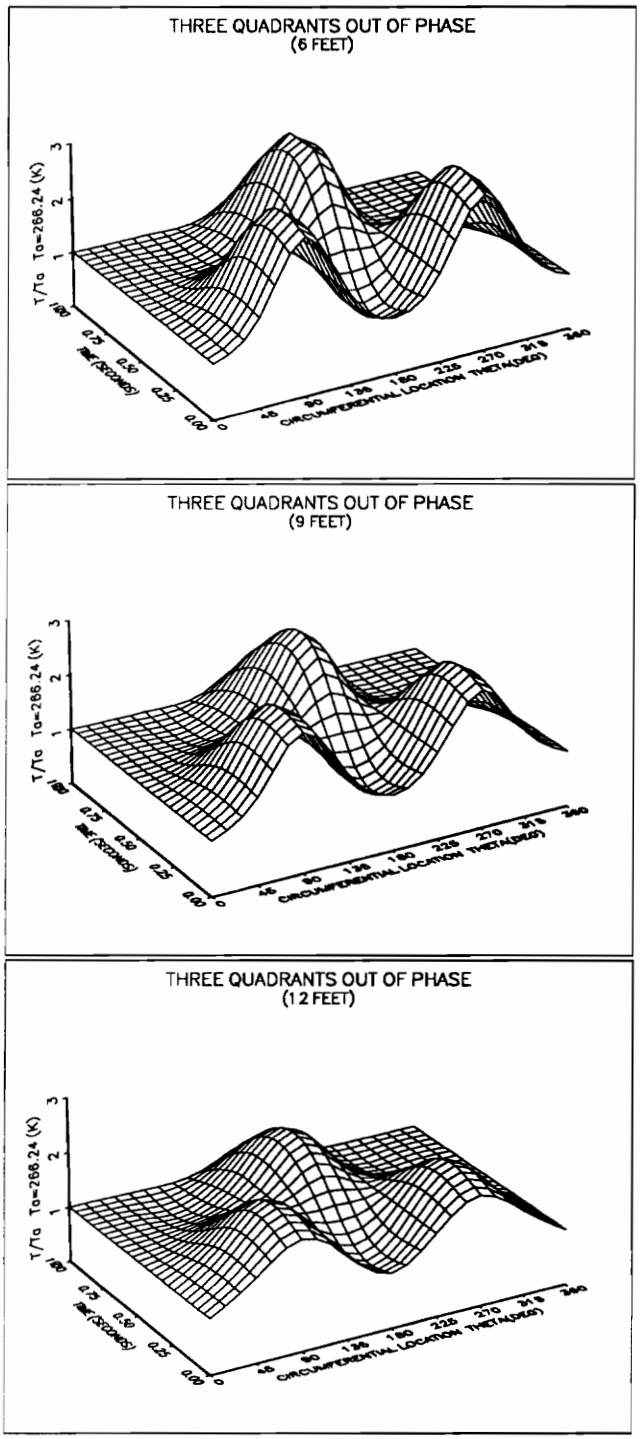

Figure 45. Temperature Distribution(Three Quadrants Out Of Phase)

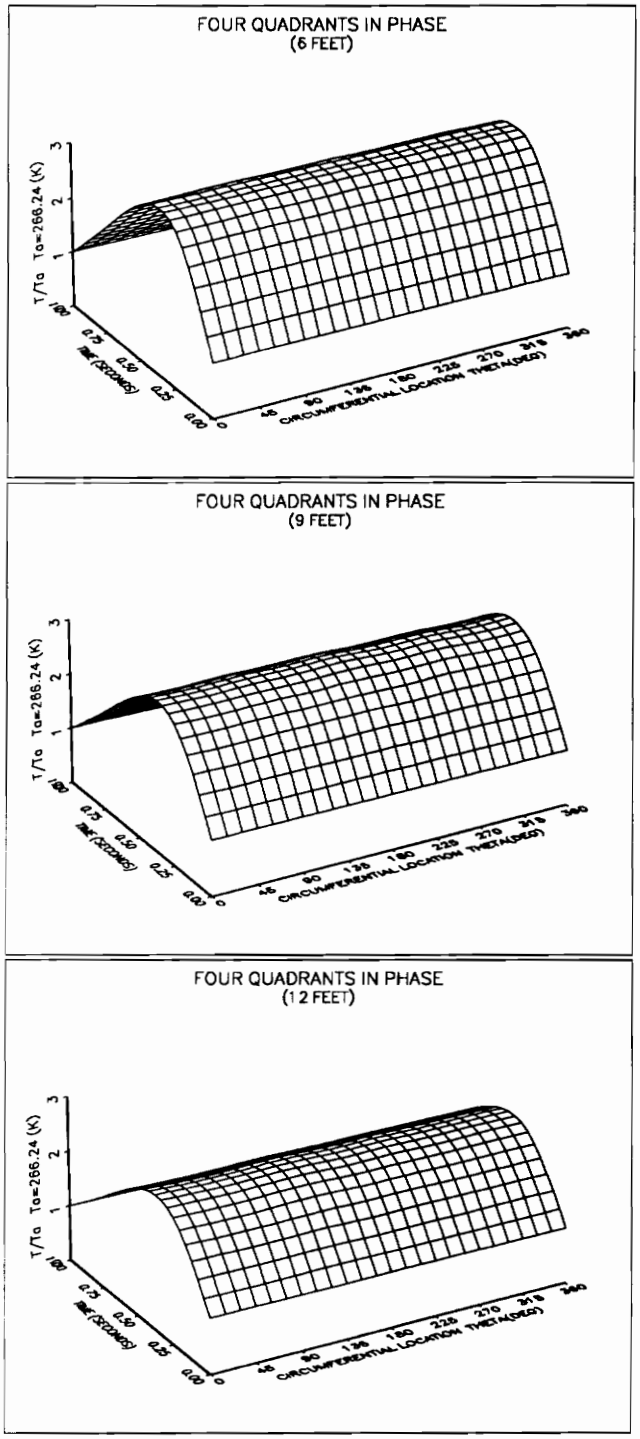

Figure 46. Temperature Distribution(Four Quadrants In Phase)

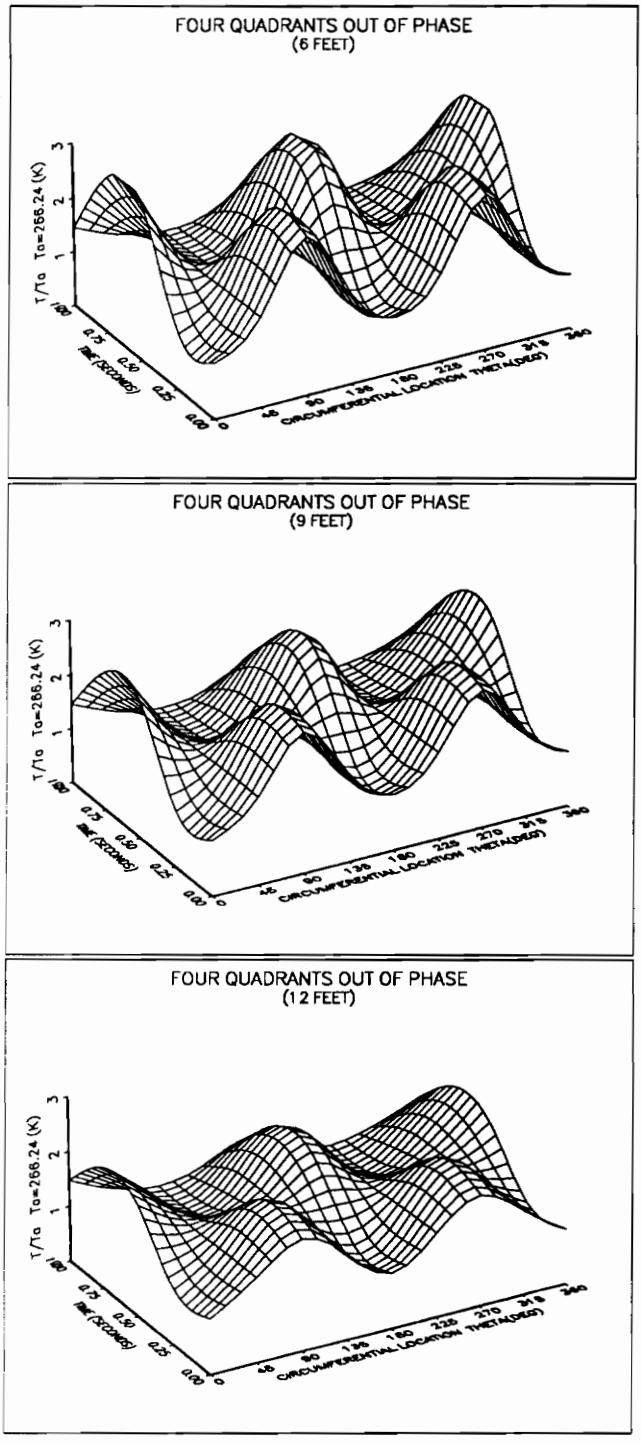

Figure 47. Temperature Distribution(Four Quadrants Out Of Phase)

XVI. DISCUSSION OF RESULTS

The thermal distortion generator was operated and data was collected for several unsteady thermal distortion patterns. The data is presented in time steps of 0.25 seconds, for one complete cycle. This indicates how the dynamic distortion pattern changes with time for each distortion pattern. During each 0.25 second time step eight thermocouple measurements were made. However, the computer did not read all eight thermocouples simutaneously. Instead, the thermocouples were read one at a time. The time step between each of the eight thermocouple measurements on each spoke of the rake was on the order of two microseconds. Therefore, a time increment of approximately 16 microseconds passed from the reading of the first thermocouple to the reading of the last thermocouple on the rake. During that 16 microsecond time interval, the distortion pattern was passing through the rake. As a result, all eight thermocouple measurements were not made in exactly the same cross section of a distortion pattern. The ideal set up would have all eight thermocouple measurements made at the same time. However, the 2 microsecond interval between each thermocouple measurement is very small and close to the ideal situation. The temperature measurements contain an error of $\pm$ 2.2 degrees (C). This error is associated with the thermocouple and is known from the OMEGA thermocouple handbook. The time constant assumed for the thermocouples used in this experiment is known and was also obtained from the OMEGA thermocouple handbook. This time constant was used in a first order time lag equation to adjust the measured temperatures and predict the actual temperatures in the duct. These manipulations must be performed on the measured data in order to account for the time response of the thermocouple. The first derivative of temperature, with respect to time, was evaluated with a second order central difference approximation. The adjustments to the data with

the time lag equation, indicate that the small necessary adjustment were within the error limits of the thermocouple for each data sample. Therefore, the profiles displayed in the Experimental section are extremely close to the actual temperature profiles in the exhaust duct. The data are presented in graphical format to "see" the different distortion patterns and pressure profiles. The temperature data was obtained at three locations in the exhaust duct : six, nine, and twelve feet from the burner exit. The data was plotted in three dimensions, circumferential location verses time verses the nondimensional temperature ratio. The presentation of the data in this format allows the dynamics of each thermal distortion pattern to be visualized. It is evident that the temperature for each distortion pattern, drops as it flows through the exhaust duct. The maximum temperature increments obtained for all the distortion patterns that were measured six feet from the burner exit were approximately 495 (K). Maximum temperature increments obtained for all the distortion patterns measured at nine and twelve feet from the burner exit were approximately 400 (K) and 350 (K) respectively. These temperatures are higher than the required temperature for distortion research stated in the assumptions of the Initial Design Concepts And Analysis section. These temperatures are higher than the design temperature because the flow rate through the distortion generator was smaller than the design flow rate. Therefore, the distortion generator was operating off design. This is not a problem because the performance of the distortion generator at low speeds must be known for testing purposes. Examination of the data plots indicate that the distortion patterns generated remained within the vicinity of their confined quadrant boundaries. There appears to be very little overlap into cold regions. This is a promising result because when a thermal distortion experiment is conducted using a complex multi quadrant pattern, little overlap will occur into cold regions. Because this overlap is small it may not have to be accounted for when interpreting the results of an experiment. This

makes the data reduction and adjustment process less complicated. Appendix C contains temperature ramp data associated with the thermal distortion patterns produced for this performance evaluating experiment. The data are plots of time verses temperature increment.The slopes of the lines on these particular plots indicate the temperature ramps produced by the distortion generator for different distortion patterns. These ramps have units of degrees per second and indicate the rate of change of temperature with respect to time. This information is important because the temperature ramp has a pronounced effect on an engine's performance and stability. These plots are the temperature ramps, at the circumferential location in the exhaust duct, where the peak temperature occurs for each distortion pattern. These plots were produced for each distortion pattern at each measuring station in the exhaust duct: six, nine, and twelve feet from the burner exit. The ramp data is also tabulated on the same page as the plot. The ideal distortion patterns, for purposes of a tightly controlled experiment, would look like a square wave or unit step input function. If this type of pattern were possible to produce then the temperature profile, at the AIP, would be precisely known. There would be no overlap of high temperature air in what was supposed to be ambient temperature air for a given distortion pattern. However, the presence of swirl in the flow, due to the rotating turbomachinery, and the fact that the temperatures at the hot and cold air boundaries cannot be discontinuous, explains why the curves have hot air overlap into cold air regions. All of the data collected display similar phenomena and is a good indication of how actual temperature profiles appear, in an engine inlet, during the ingestion of hot exhaust gases.

The data for the combustion temperature as a function of equivalence ratio plot was generated by STANJAN which is an equilibrium chemistry combustion analysis program. STANJAN also provided the chemical composition of the products for each combustion reaction which is presented in Appendix E. The temperature ramp generated

in the burner is also plotted as a function of equivalence ratio. This is the temperature ramp produced by each of the four burners directly behind their recirculation zones. The data was obtained by dividing the maximum temperature achieved, for each equivalence ratio, by the time for a combustion reaction of propane and air to occur. This reaction time was obtained from Ref(9).

The static and total pressure profiles at the AIP are uniform. There is very little pressure distortion and pressure loss associated with the geometry of the distortion generator. This is a promising result because the problem with pressure distortion and pressure loss is that it translates into a local reduction in fluid axial velocity. The reduction in fluid axial velocity causes the relative velocity angle of attack on the airfoils of the fan or compressor rotor to increase if the rotor mechanical speed is kept constant. If the angle of attack increase is significant, the flow will separate from the airfoil surface and the blade will stall. Thus a rotating stall cell will develop and propagate around the rotor; and if this stall cell is of sufficient circumferential extent, it will lead to the surging of the entire compressor.

XVII. CONCLUSIONS

A thermal distortion generator that simulates unsteady temperature distortions associated with gas turbine or rocket exhaust gas ingestion into axial flow fans and compressors was designed. The thermal distortion generator, and its associated hardware, are an original design and a first attempt to develop a device that would produce a time varying distortion pattern. The speed of the compressor in the test cell was only subsonic during the experiment. Therefore, the mass flow rates through the distortion generator were not accurately simulated for a transonic fan or compressor. This is not a problem because it is necessary to observe how the distortion generator performs at low speed. The design, fabrication, and test of a similar device that will produce a dynamic pressure distortion will be future work associated with this project. Eventually it will be necessary to observe how a low speed fan or compressor will respond to combined dynamic distortion produced by these two devices. A problem with the project was the propane cylinders were stored outside the building. The cold air during the winter time helps the tanks to freeze when they begin to drop pressure. This causes poor performance because the fuel line pressure is low.

The thermal distortion generator was operated and data collected for eight unsteady thermal distortion patterns. The data was adjusted to account for the response time of the thermocouples measuring temperatures in the exhaust duct. The data was plotted in three dimensions to allow the dynamics of each thermal distortion pattern to be visualized. The data indicated that the temperatures of thermal distortions decrease as the distortion flows through the exhaust duct. The peak temperatures and ramps produced by the thermal distortion generator will be sufficient to induce surge and rotating stall on low speed research fans and compressors. Therefore, the distortion generator is adequate

for thermal distortion research. The fact that the distortion patterns generated remained within the vicinity of their confined quadrant boundaries will make the data reduction and adjustment process less complicated. Also, the fact that there is almost no pressure distortion and pressure loss, at low speed, associated with the geometry of the distortion generator will make it a valuable research tool. This fact will also make the data reduction and adjustment process less complicated because the fan or compressor rotor will not stall or surge due to a pressure distortion produced by the distortion generator's geometry. Therefore, any fan or compressor dynamic event that occurs will not be induced by inlet blockage or the distortion generator geometry.

Initial design concepts were conceived and analyzed on the basis of first principles. A final design was selected based upon the preliminary design analysis. Details of the final design's geometry, aerothermodynamics, and performance were determined. A special combustion test cell was designed, developed, and operated. Special fuel control, ignition, and data acquisition systems were also designed, developed, and implemented. An experimental prototype burner was designed, fabricated and operated. The final design concept was also fabricated and operated. Static and total pressure measurements were performed at the AIP and plotted. Combustion experiments were performed with the fabricated design and temperature data obtained for different unsteady distortion patterns at different measuring stations. Data was plotted at various time steps throughout one complete cycle. Propane and air combustion reactions, for different equivalence ratios, were developed and analyzed with STANJAN. These STANJAN outputs for propane and air are located in the Appendix section. Temperatures and temperature ramps were predicted in the distortion generator and plotted as a function of equivalence ratio. The Appendix provides various data regarding the performance of different fuels and oxidizers used in liquid and solid rocket motors.

This information allows a comparison to be made between a combustion reaction of propane and air, and a combustion reaction involving different fuels and oxidizers. This information will be necessary if an extension of this work is conducted with some exotic rocket fuel and oxidizer, to study the effects of rocket exhaust gas composition on the fan or compressor rotor aerodynamics. Test cell start up and shut down safety procedures were determined and incorporated in the Appendix. A trouble shooting section, indicating some potential operation problems and their causes, was also developed and incorporated in the Appendix section.

XVIII. RECOMMENDATIONS

Further research may be conducted with this unsteady thermal distortion generator. Research can be conducted on the effects of different unsteady distortion patterns on fan or compressor rotor stall and surge margins. Research may also be conducted to investigate the effects of high temperature foreign gas on the compressible aerodynamics, boundary layer separation, and tip vortex shedding of the fan or compressor blades. Modifications can be made to the distortion generator to burn different fuels, possibly jet fuel, whose combustion with air, or some other oxidizer, would produce actual combustion products that might be ingested from gas turbine or rocket engine exhaust gases. Finally, research could be conducted on the effects of combined unsteady pressure and temperature distortion on the performance of axial flow fans and compressors. This would require the fabrication of a device that could produce unsteady pressure distortion patterns. This device, along with the thermal distortion generator, could be attached to the inlet of a transonic fan or compressor in order to produce combined distortion.

Therefore, some future recommendations are:

1. Design, fabricate and test a device that will produce an unsteady pressure distortion.
2. Use the two devices in combination on a low speed fan and investigate the fan response to combined dynamic distortion.
3. Test the distortion generators on a multi-stage transonic fan or compressor.
4. Obtain pressure and temperature data at various measuring stations in the duct.

5. Investigate multi-stage transonic fan or compressor response to combined dynamic distortion.
6. Use four propane cylinders, one per quadrant, and maintain cylinders at room temperature.

XIX. BIBLIOGRAPHY

Cited References

1. Wells, H.S., " A Study Of Rocket Exhaust Gas Ingestion Simulation Techniques For The AEDC", ARO ENGR RPT 77-3, March 1977.

2. Childs, J.H., Kochendorfer, F.D., Lubick, R.J., and Friedman, R., " Stall And Flame-Out Resulting From Firing Of Armament", NACA RM E55E25, 1955.

3. Walter, W.A. and Shaw, M.,"Predicted F100 Engine Response To Circumferential Pressure And Temperature Distortion", 1979.

4 Braithwaite, W.M., Garber Jr., E.J., and Mehalic, C.M., " The Effect Of Inlet Temperature And Pressure Distortion On Turbojet Performance", AIAA Paper No. 73-1316, 1973.

5. Society of Automotive Engineers, Inc.,"Aerospace Recommended Practice 1420 Gas Turbine Engine Inlet Flow Distortion Guildlines", ARP 1420, 1979.

6. Society of Automotive Engineers, "A Current Assessment Of The Inlet/Engine Temperature Distortion Problem", Aerospace Resource Document ARD50015, 1991-01-22

Uncited References

7. Seddon, J. and Goldsmith, E.L., " Intake Aerodynamics", AIAA Educational Series, Published by American Institute of Aeronautics and Astronautics, Inc 1985.

8. Oates, G.C., " Aerothermodynamics of Gas Turbine and Rocket Propulsion", AIAA Educational Series , Published by American Institute of Aeronautics and Astronautics, Inc, 1988, pp.19-62

9. Oates, G.C., " Aerothermodynamics of Aircraft Engine Components", AIAA Educational Series, Published by American Institute of Aeronautics and Astronautics, Inc., 1985.

10. Cohen, H., Rogers, G.F.C., Saravanamuttoo, H.I.H., "Gas Turbine Theory", Third Edition, John Wiley& Sons, Inc., New York, 1978.

BIBLIOGRAPHY(continued)

11. Hill, P.G., Peterson, C.R., " Mechanics And Thermodynamics Of Propulsion", Addison Wesley Publishing Company, Inc., 1965.

12. Kuo, K.K., "Principles Of Combustion", John Wiley&Sons, Inc. 1986

13. Van Wylen, G.J., Sonntag, R.E., " Fundamentals Of Classical Thermodynamics", Third Edition, John Wiley& Sons, Inc., New York, 1986.

14. Schetz, J.A., "Foundations of Boundary Layer Theory For Momentum, Heat, and Mass Transfer", Prentice Hall, Inc., New Jersey, 1984.

15. Anderson, J.D., " Modern Compressible Flow With Historic Perspective", second edition, McGraw Hill Publishing Company, 1982.

16. Bertin, J.J., Smith, M.L., " Aerodynamics For Engineers", second edition, Prentice Hall, Inc., New Jersey, 1979.

17. Brady, J.E., Humiston, G.E., " General Chemistry Principles And Structure", forth edition, John Wiley& Sons, Inc., 1986.

18. Vincenti, W.G., Kruger Jr. C.H., " Introduction To Physical Gas Dynamics", Robert E. Krieger Publishing Co., Inc., Florida, 1986.

19. Wilkins, Roger Lawrence, "Theoretical Evaluation Of Chemical Propellants", Prentice-Hall Space Technology Series, Prentice Hall, Inc., New Jersey, 1963.

20. Adams, G.K., "The Chemistry Of Solid Propellant Combustion" Symposium Publications Division, Pergamon Press, 1965.

21. Jane's " All the World's Aircraft", 1991-1992

XX. APPENDICES

A- Performance Problems(Problems Associated with Operation)

B- Starting and Shutdown Procedures(Safety Procedures)

C- Data(Temperature Ramps)

D- Photographs(Facility/Hardware/Distortion Generator)

E- Performance Data For Liquid and Solid Rocket Propellants

F- Instrumentation/Hardware(Instrumentation/Hardware Data and Experimental Operating Conditions)

G- Calibration(Calibration of Equipment)

Appendix A

Performance Problems

No Combustion :

- Propane tanks empty.
- Propane tank valves not open.
- Regulator valve not open.
- Solenoid valve not opening.
- Ignition system not functioning.
- Ignition system malfunction.
- Ignition plug oxidized or worn.
- Compressed air not flowing.
- Fuel/Air ratio incorrect.
- Solid state relay defective.
- Nozzle clogged

Smoke or Soot :

- Fuel/Air ratio incorrect.
- Insufficient air for combustion.
- Lack of air velocity and turbulence.
- Ignition plug malfunction.
- Ignition system malfunction.
- Incomplete combustion.
- Nozzles partially blocked.

- Compressor not operating.
- Fuel pressure to low.
- Flame striking the duct walls.

Delayed Ignition :

- Fuel pressure to low.
- Fuel leaks.
- Fuel tank valve not opened sufficiently.
- Fuel/Air ratio incorrect.
- Solenoid valve sticking.
- Lack of air velocity and turbulence.

Odors :

- Fuel leak.
- Poor seals around pipes and valves.
- Incomplete combustion.
- Fuel/Air ratio incorrect.
- Ignition system malfunction.
- Electric motor hot.
- Motor/Generator box hot.
- Compressor not operating.

No Spark :

- Burners not grounded properly.
- Ignition wires not connected to ignition plugs.
- Ignition system not plugged in to wall.
- Ignition plug oxidized or worn.
- Faulty component in the electronic ignition circuit.
- Faulty ignition wire.

Appendix B

Starting and Shutdown Procedures

A. Examine the following items before operating the distortion generator :

1. The distortion generator is securely mounted.
2. The compressor and drive motor are securely anchored.
3. All the regulator valves are closed.
4. Determine if there are any strange odors.-(like fuel)
5. The thermocouples are securely mounted.
6. The condition of all wires and power cables.
7. The condition of the ignition plugs.- (any carbon deposits)
8. The combustion chambers are free of foreign materials.
9. All air hoses are attached.
10. All ignition wires are attached.
11. The blades on the compressor rotor are all present and secure.

B. Start-Up Procedure :

1. Open test cell door all the way.
2. Open the compressed air valves.
3. Turn on the computer and load in the appropriate program.
4. Turn on the motor/generator box.
5. Turn on ignition box.
6. Bring the compressor up to idle speed.
7. Open the valves on the propane tanks.
8. Bring compressor up to appropriate speed.

9. Turn on the power to the solenoid valves.
10. Activate the solenoid valve.
11. Open each regulator valve slowly and one at a time.
12. Observe thermocouple readings.

Note: For complex distortion patterns, involving 3 or 4 quadrants, it is necessary to keep all regulator valves open very little to allow each combustion reaction to stabilize behind each burner initially. Once combustion has been stabilized, on all desired burners, then the regulator valves may be opened to achieve desired temperatures.

CAUTION ! : Do Not Attempt To Open Regulator Valves To Fast. Also, Do Not Attempt To Open More Than One Regulator Valve At A Time.

C. Shutdown Procedures :

1. Turn off solenoid power switch.
2. Close all regulator valves.
3. Bring compressor speed back to idle.
4. Close valves on propane tanks.
5. Turn off ignition system.
6. Stop the compressor.
7. Stop motor/generator box.

8. Close compressed air valves.
9. Turn off computer.
10. Leave all equipment unplugged.
11. Do not leave facility for at least ten minutes to allow burner to cool off.
12. Close and lock test cell door.

Appendix C

Data (Temperature Ramps)

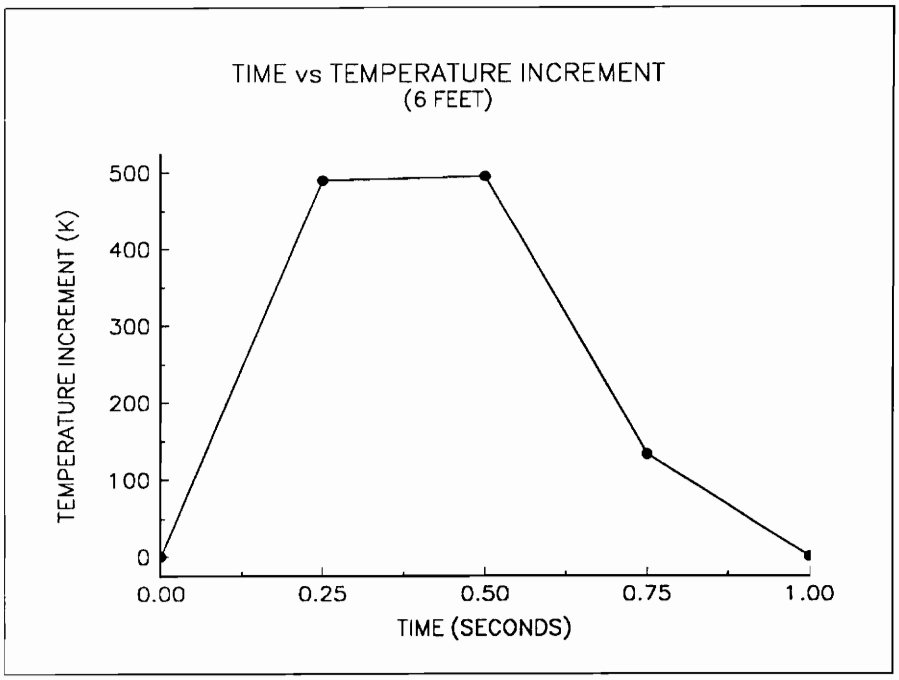

TIME (sec.)	ΔT (K)	RAMP (K/sec)
0.0-0.25	0.0-489.9	1959.6
0.25-0.5	489.9-495.2	21.2
0.5-0.75	495.2-133.1	-1448.30
0.75-1.0	133.1-0.0	-532.5

Figure 48. Time vs Maximum Temperature Increment Per Quadrant
(One Quadrant, 6 Feet)

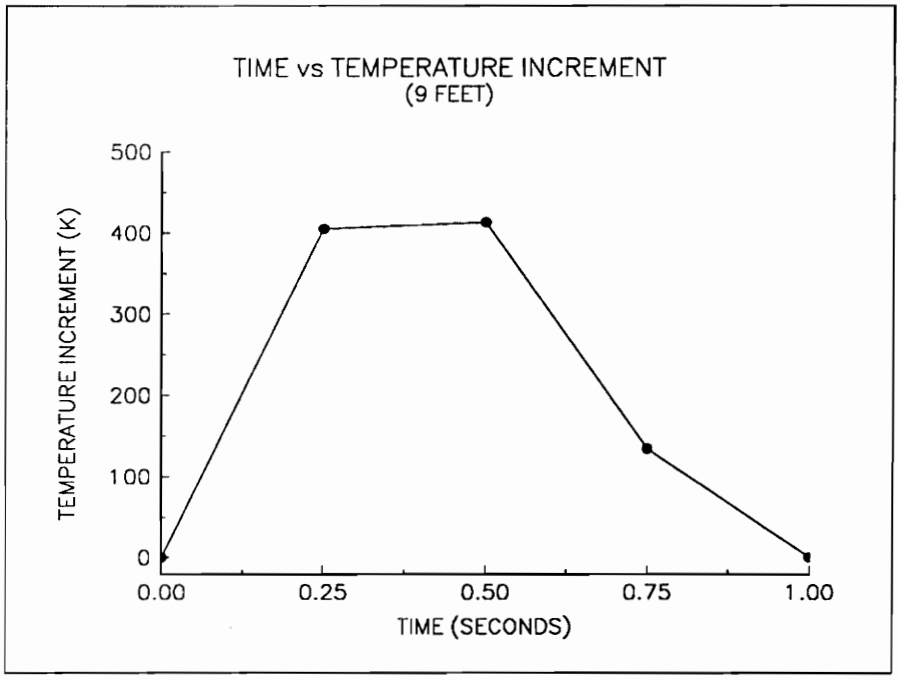

TIME (sec.)	ΔT (K)	RAMP (K/sec)
0.0-0.25	0.0-405.1	1620.4
0.25-0.5	405.1-413.2	32.4
0.5-0.75	413.2-134.1	-1116.4
0.75-1.0	134.1-0.0	-536.4

Figure 49. Time vs Maximum Temperature Increment Per Quadrant (One Quadrant, 9 Feet)

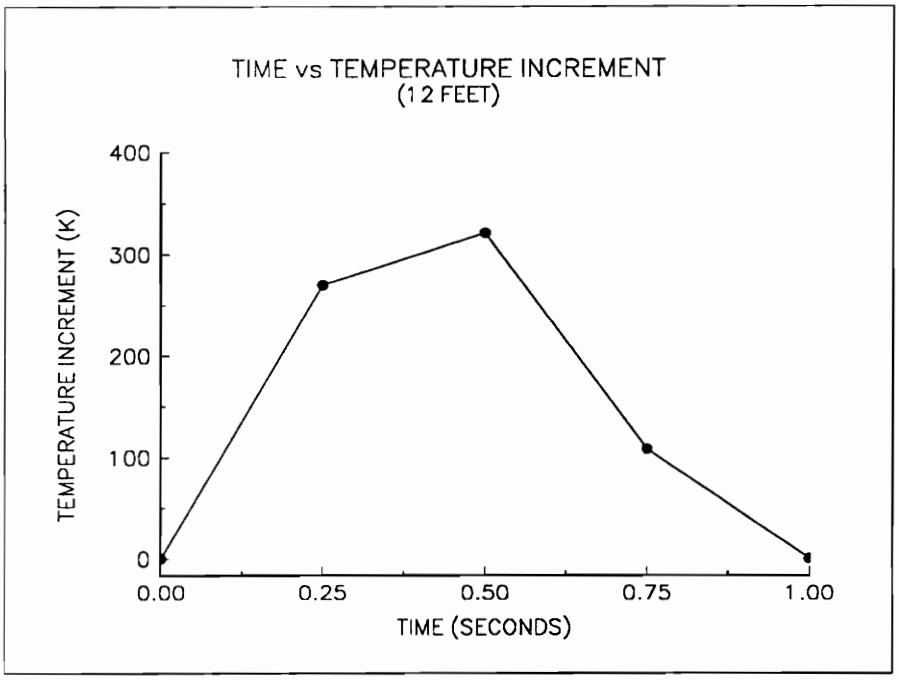

TIME (sec.)	ΔT (K)	RAMP (K/sec)
0.0-0.25	0.0-270.0	1078.8
0.25-0.5	270.0-320.9	204.8
0.5-0.75	320.9-107.9	-852.0
0.75-1.0	107.9-0.0	-431.6

Figure 50. Time vs Maximum Temperature Increment Per Quadrant
(One Quadrant, 12 Feet)

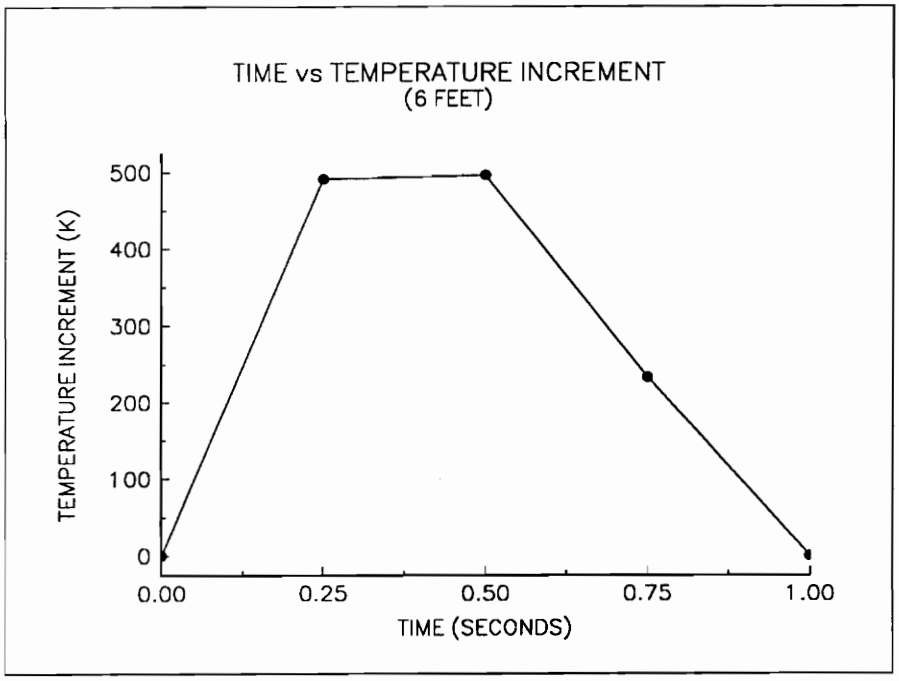

TIME (sec.)	ΔT (K)	RAMP (K/sec)
0.0-0.25	0.0-490.7	1962.8
0.25-0.5	490.7-496.1	21.6
0.5-0.75	496.1-232.0	-1056.4
0.75-1.0	232.0-0.0	-928.0

Figure 51. Time vs Maximum Temperature Increment Per Quadrant
(Two Adjacent Quadrants In Phase, 6 Feet)

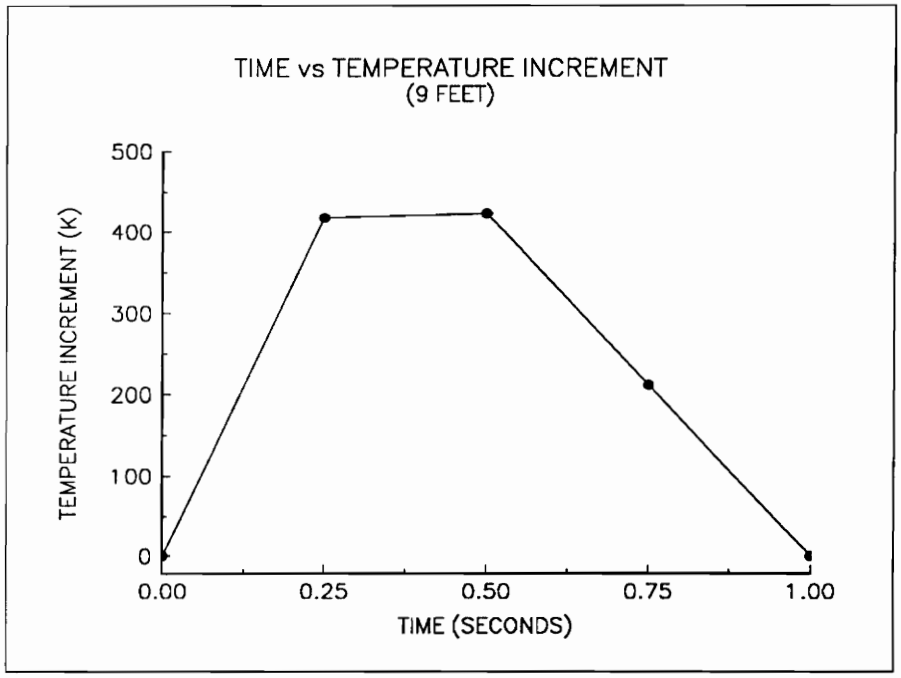

TIME (sec.)	ΔT (K)	RAMP (K/sec)
0.0-0.25	0.0-417.9	1671.6
0.25-0.5	417.9-423.3	21.6
0.5-0.75	423.3-211.6	-846.8
0.75-1.0	211.6-0.0	-846.4

Figure 52. Time vs Maximum Temperature Increment Per Quadrant
(Two Adjacent Quadrants In Phase, 9 Feet)

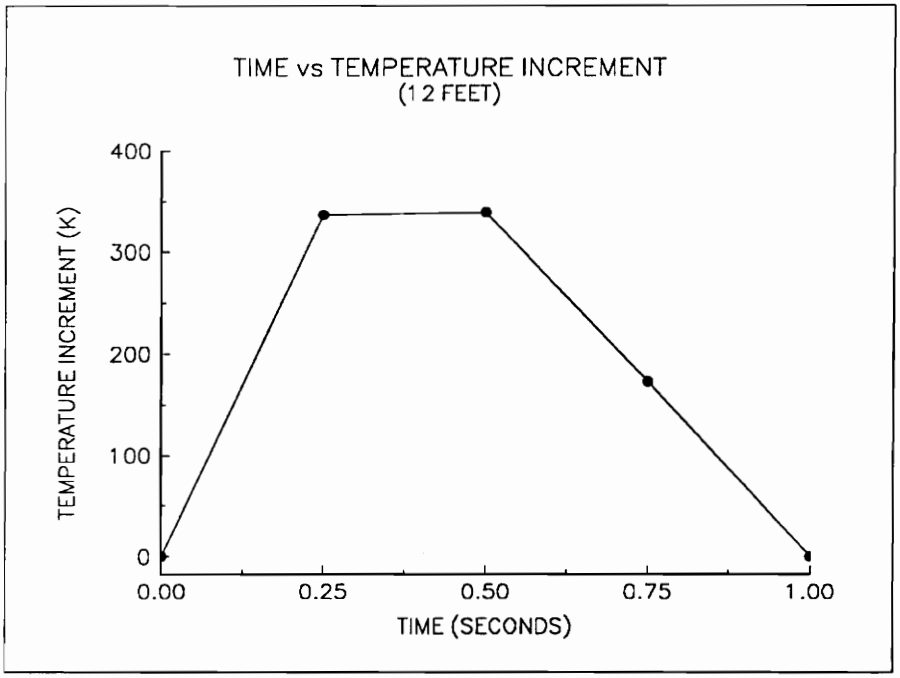

TIME (sec.)	ΔT (K)	RAMP (K/sec)
0.0-0.25	0.0-336.7	1346.8
0.25-0.5	336.7-339.4	10.8
0.5-0.75	339.4-172.4	-668.0
0.75-1.0	172.4-0.0	-689.6

Figure 53. Time vs Maximum Temperature Increment Per Quadrant
(Two Adjacent Quadrants In Phase, 12 Feet)

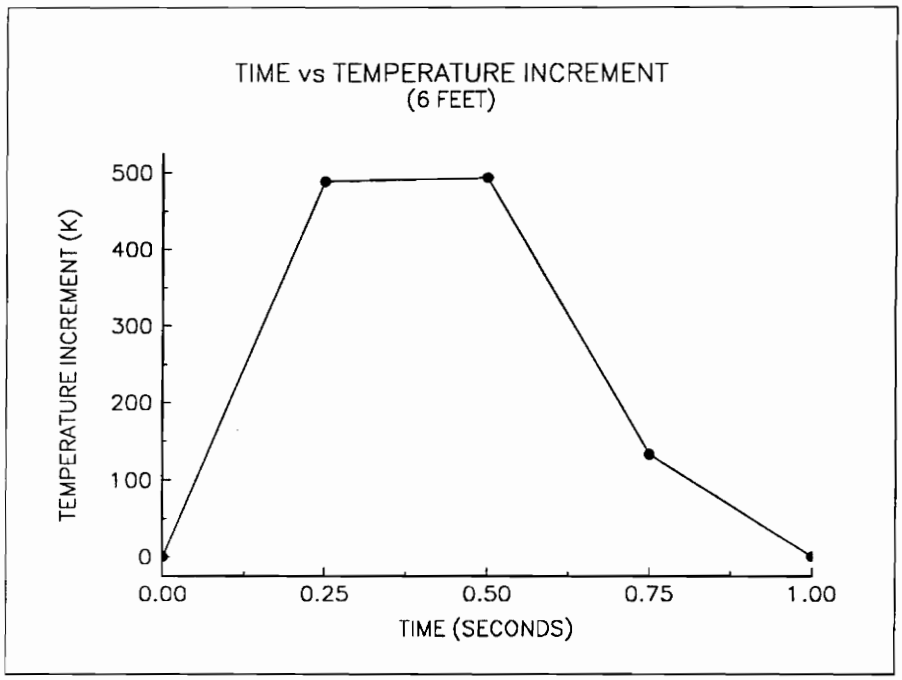

TIME (sec.)	ΔT (K)	RAMP (K/sec)
0.0-0.25	0.0-488.4	1953.6
0.25-0.5	488.4-493.7	21.2
0.5-0.75	493.7-132.7	-1444.0
0.75-1.0	132.7-0.0	-530.8

Figure 54. Time vs Maximum Temperature Increment Per Quadrant
(Two Adjacent Quadrants Out Of Phase, 6 Feet)

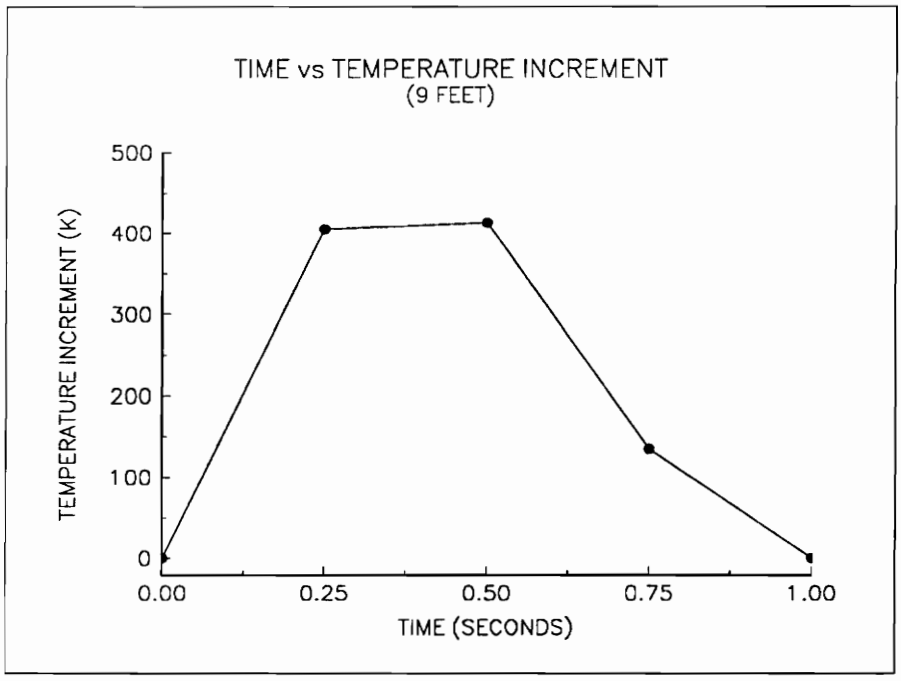

TIME (sec.)	ΔT (K)	RAMP (K/sec)
0.0-0.25	0.0-405.2	1620.8
0.25-0.5	405.2-413.2	32.0
0.5-0.75	413.2-134.2	-1116.0
0.75-1.0	134.2-0.0	-536.8

Figure 55. Time vs Maximum Temperature Increment Per Quadrant
(Two Adjacent Quadrants Out Of Phase, 9 Feet)

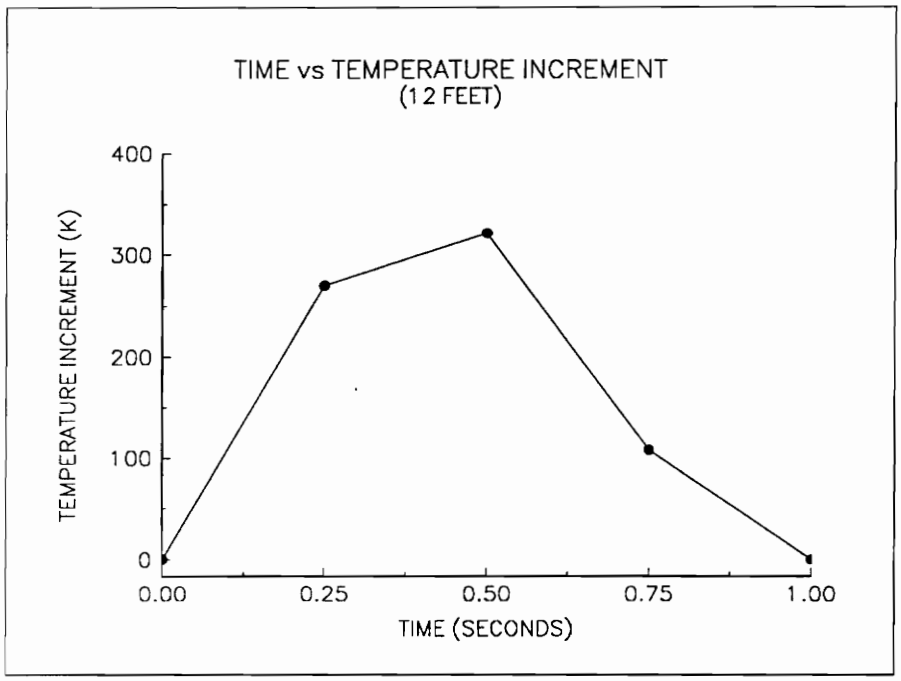

TIME (sec.)	ΔT (K)	RAMP (K/sec)
0.0-0.25	0.0-270.2	1080.1
0.25-0.5	270.2-321.3	205.1
0.5-0.75	321.3-108.0	-853.2
0.75-1.0	108.0-0.0	-432.0

Figure 56. Time vs Maximum Temperature Increment Per Quadrant
(Two Adjacent Quadrants Out Of Phase, 12 Feet)

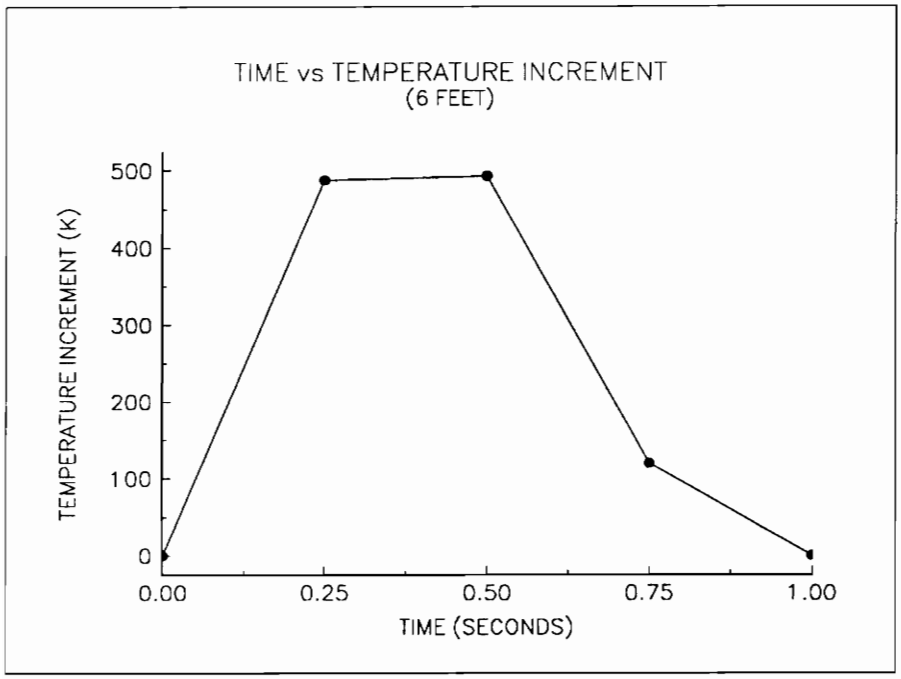

TIME (sec.)	ΔT (K)	RAMP (K/sec)
0.0-0.25	0.0-487.7	1950.8
0.25-0.5	487.7-493.0	21.0
0.5-0.75	493.0-119.9	-1492.4
0.75-1.0	119.9-0.0	-479.6

Figure 57. Time vs Maximum Temperature Increment Per Quadrant
(Two Opposing Quadrants In Phase, 6 Feet)

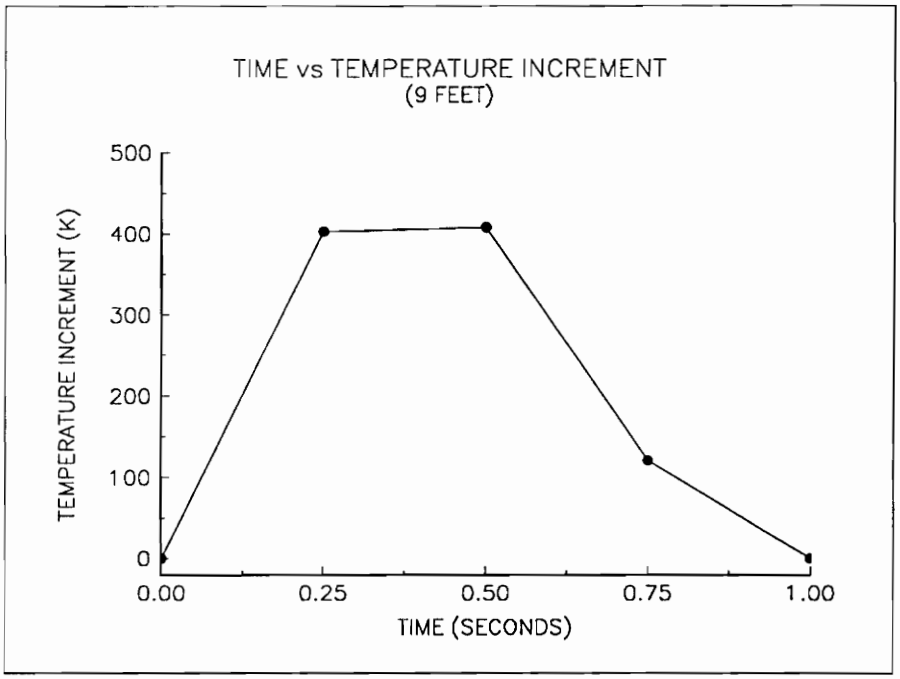

TIME (sec.)	ΔT (K)	RAMP (K/sec)
0.0-0.25	0.0-402.4	1609.6
0.25-0.5	402.4-407.8	21.6
0.5-0.75	407.8-120.7	-1148.4
0.75-1.0	120.7-0.0	-482.8

Figure 58. Time vs Maximum Temperature Increment Per Quadrant
(Two Opposing Quadrants In Phase, 9 Feet)

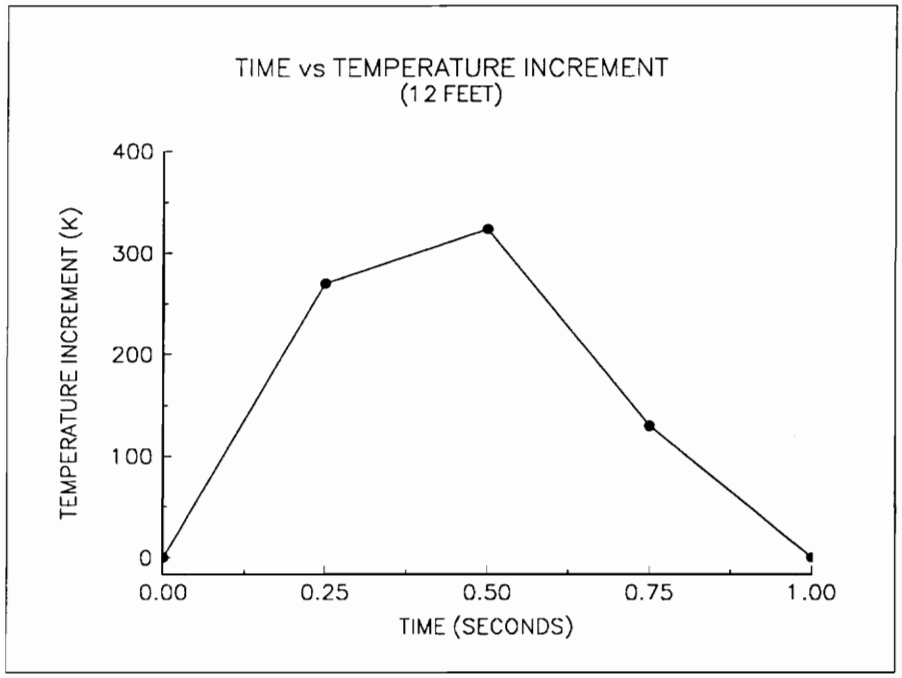

TIME (sec.)	ΔT (K)	RAMP (K/sec)
0.0-0.25	0.0-269.8	1079.4
0.25-0.5	269.8-323.8	215.8
0.5-0.75	323.8-129.5	-777.2
0.75-1.0	129.5-0.0	-518.1

Figure 59. Time vs Maximum Temperature Increment Per Quadrant
(Two Opposing Quadrants In Phase, 12 Feet)

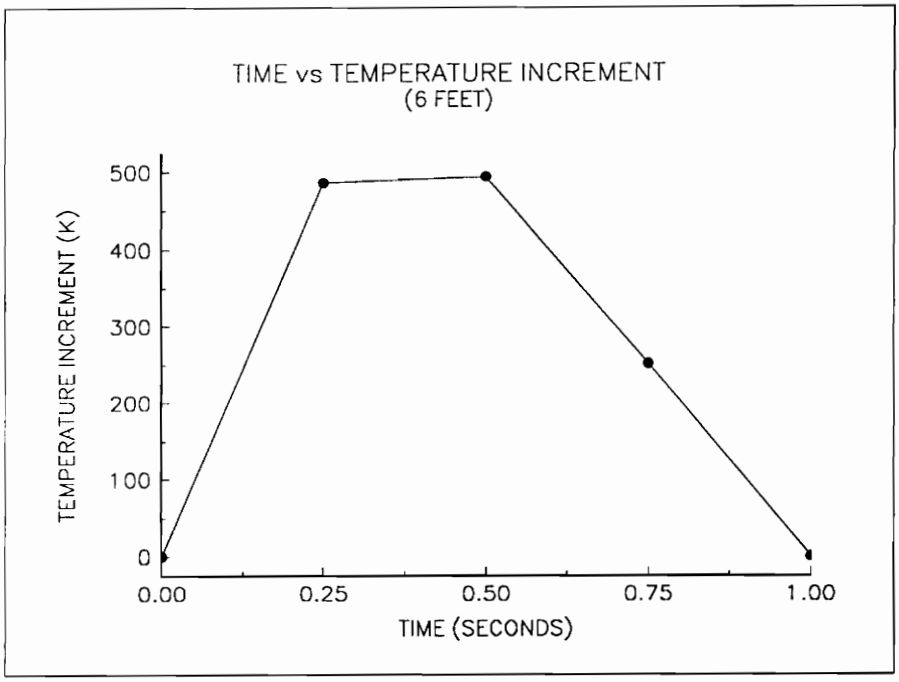

TIME (sec.)	ΔT (K)	RAMP (K/sec)
0.0-0.25	0.0-486.2	1944.8
0.25-0.5	486.2-494.2	32.1
0.5-0.75	494.2-251.1	-972.4
0.75-1.0	251.1-0.0	-1004.4

Figure 60. Time vs Maximum Temperature Increment Per Quadrant
(Three Quadrants In Phase, 6 Feet)

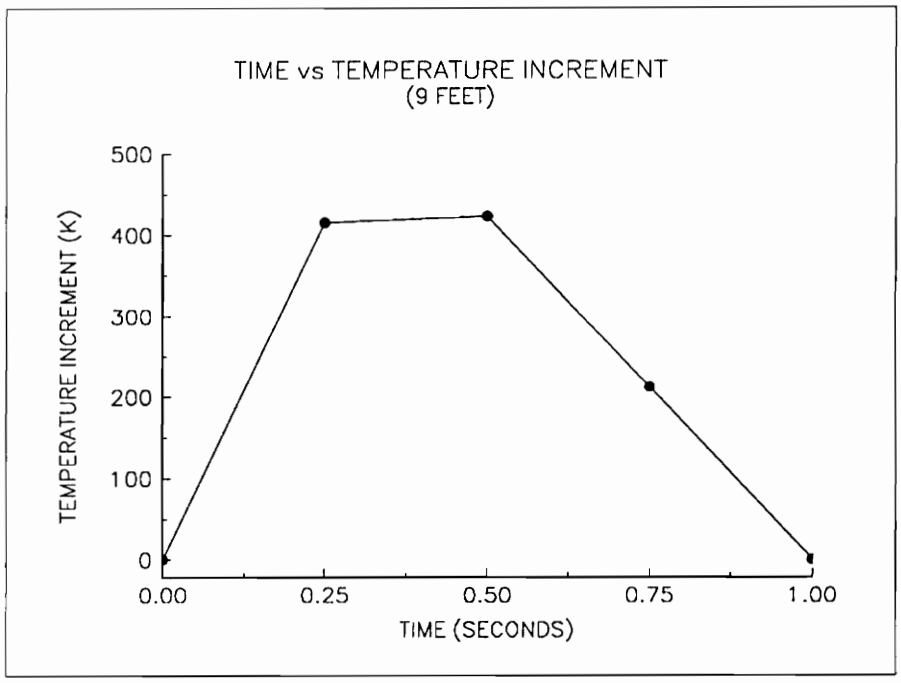

TIME (sec.)	ΔT (K)	RAMP (K/sec)
0.0-0.25	0.0-415.0	1660.0
0.25-0.5	415.0-423.1	32.4
0.5-0.75	423.1-211.5	-846.4
0.75-1.0	211.5-0.0	-846.0

Figure 61. Time vs Maximum Temperature Increment Per Quadrant
(Three Quadrants In Phase, 9 Feet)

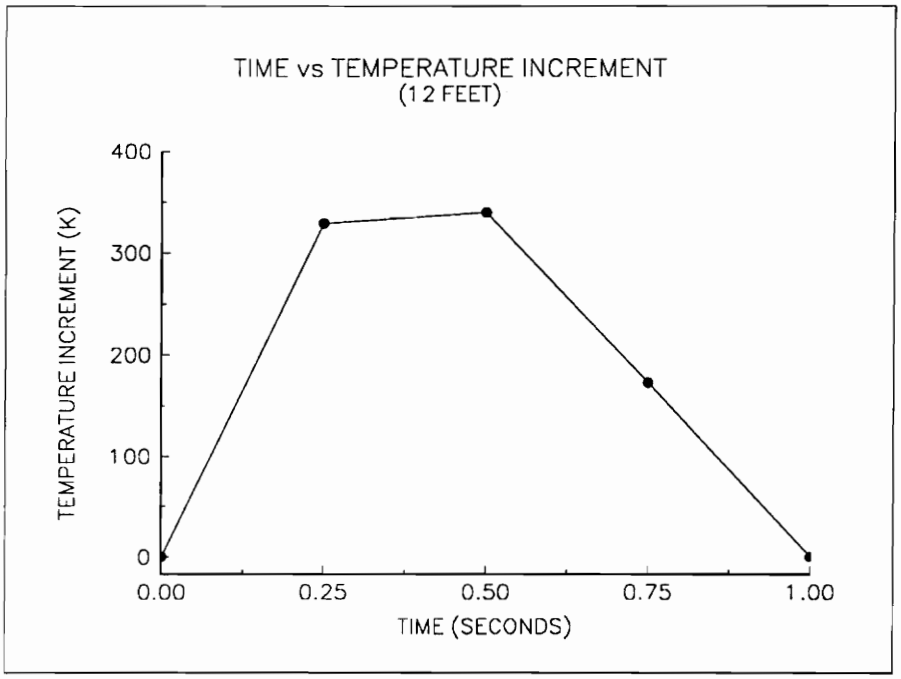

TIME (sec.)	ΔT (K)	RAMP (K/sec)
0.0-0.25	0.0-328.7	1314.8
0.25-0.5	328.7-339.5	43.2
0.5-0.75	339.5-172.5	-668.1
0.75-1.0	172.5-0.0	-690.3

Figure 62. Time vs Maximum Temperature Increment Per Quadrant
(Three Quadrants In Phase, 12 Feet)

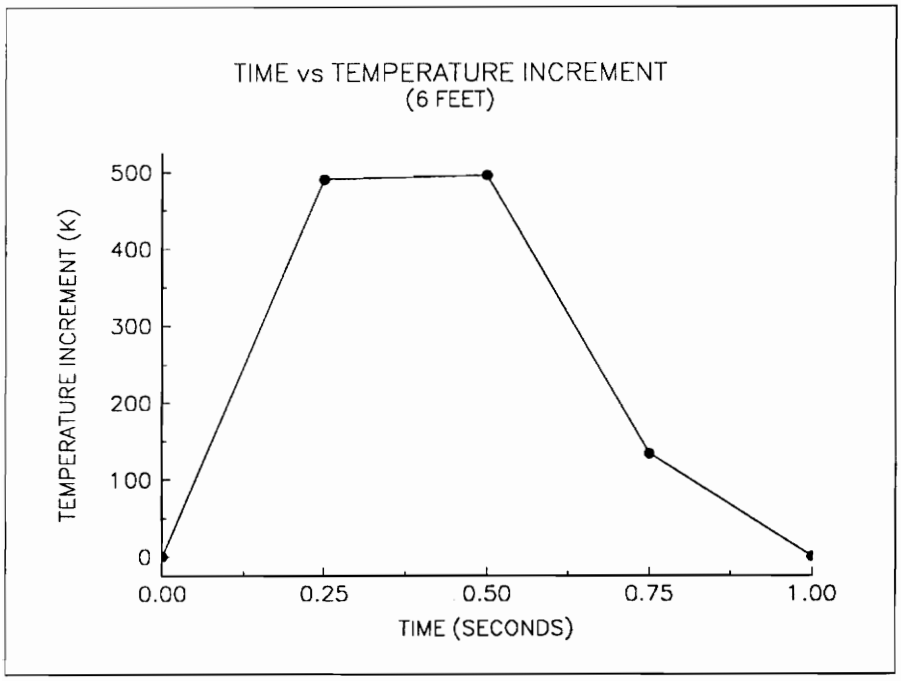

TIME (sec.)	ΔT (K)	RAMP (K/sec)
0.0-0.25	0.0-490.3	1961.2
0.25-0.5	490.3-495.7	21.6
0.5-0.75	495.7-133.2	-1450.4
0.75-1.0	133.2-0.0	-532.8

Figure 63. Time vs Maximum Temperature Increment Per Quadrant
(Three Quadrants Out Of Phase, 6 Feet)

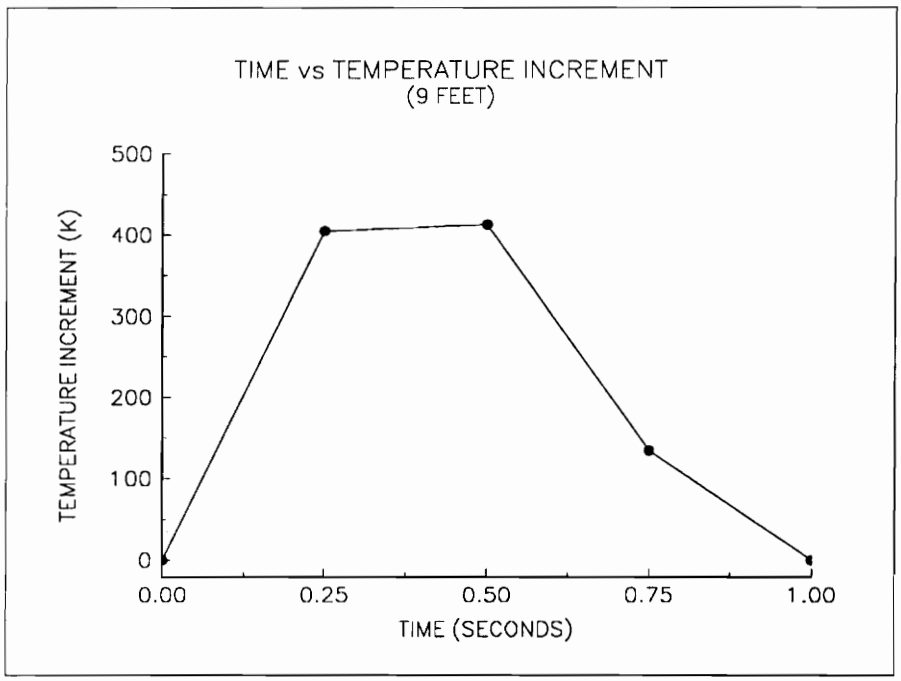

TIME (sec.)	ΔT (K)	RAMP (K/sec)
0.0-0.25	0.0-404.7	1618.8
0.25-0.5	404.7-412.8	32.8
0.5-0.75	412.8-134.7	-1115.1
0.75-1.0	134.7-0.0	-536.1

Figure 64. Time vs Maximum Temperature Increment Per Quadrant
(Three Quadrants Out Of Phase, 9 Feet)

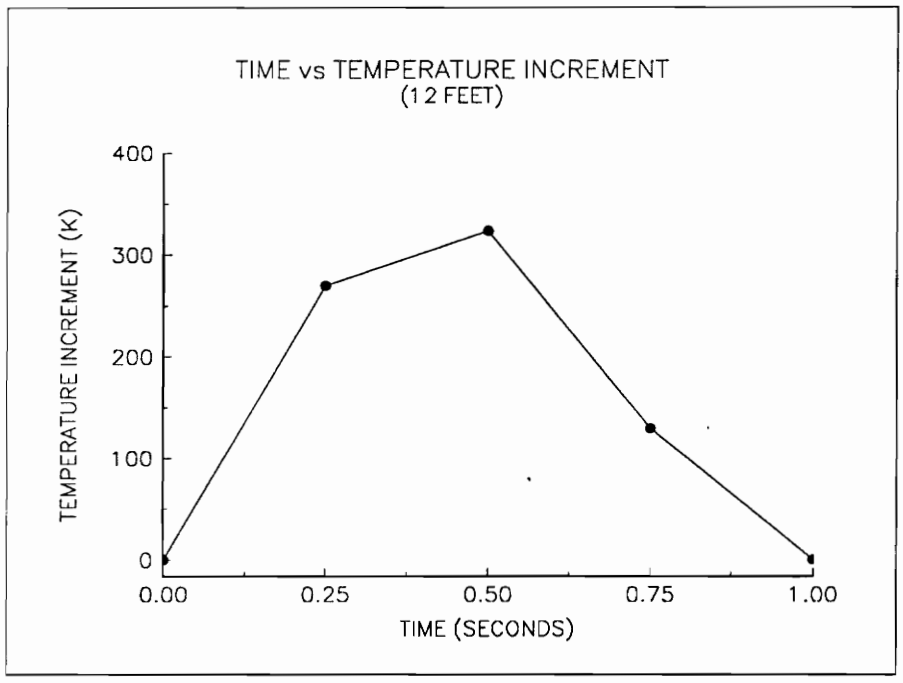

TIME (sec.)	ΔT (K)	RAMP (K/sec)
0.0-0.25	0.0-269.4	1077.5
0.25-0.5	269.4-323.2	215.3
0.5-0.75	323.2-129.4	-775.6
0.75-1.0	129.4-0.0	-517.2

Figure 65. Time vs Maximum Temperature Increment Per Quadrant
(Three Quadrants Out Of Phase, 12 Feet)

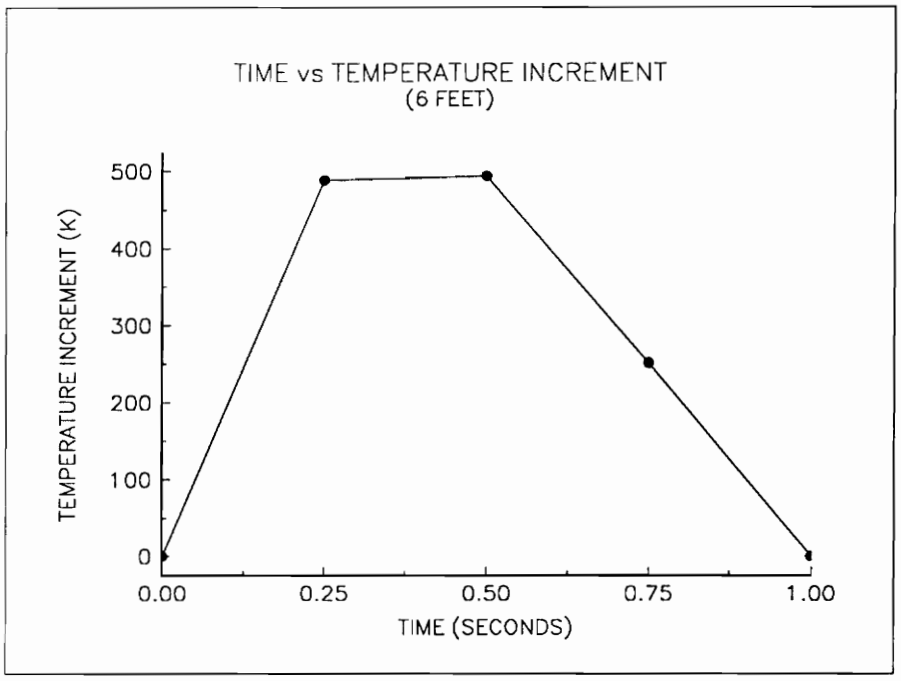

TIME (sec.)	ΔT (K)	RAMP (K/sec)
0.0-0.25	0.0-488.3	1953.2
0.25-0.5	488.3-493.7	21.6
0.5-0.75	493.7-250.8	-971.6
0.75-1.0	250.8-0.0	-1003.2

Figure 66. Time vs Maximum Temperature Increment Per Quadrant
(Four Quadrants In Phase, 6 Feet)

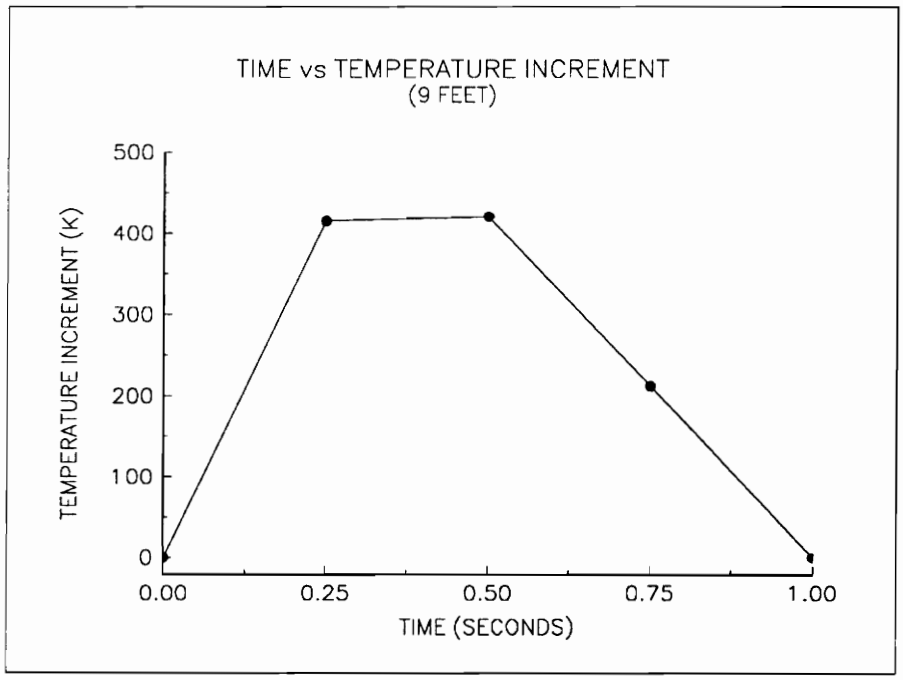

TIME (sec.)	ΔT (K)	RAMP (K/sec)
0.0-0.25	0.0-415.1	1660.4
0.25-0.5	415.1-420.4	21.2
0.5-0.75	420.4-211.5	-835.6
0.75-1.0	211.5-0.0	-846.6

Figure 67. Time vs Maximum Temperature Increment Per Quadrant
(Four Quadrants In Phase, 9 Feet)

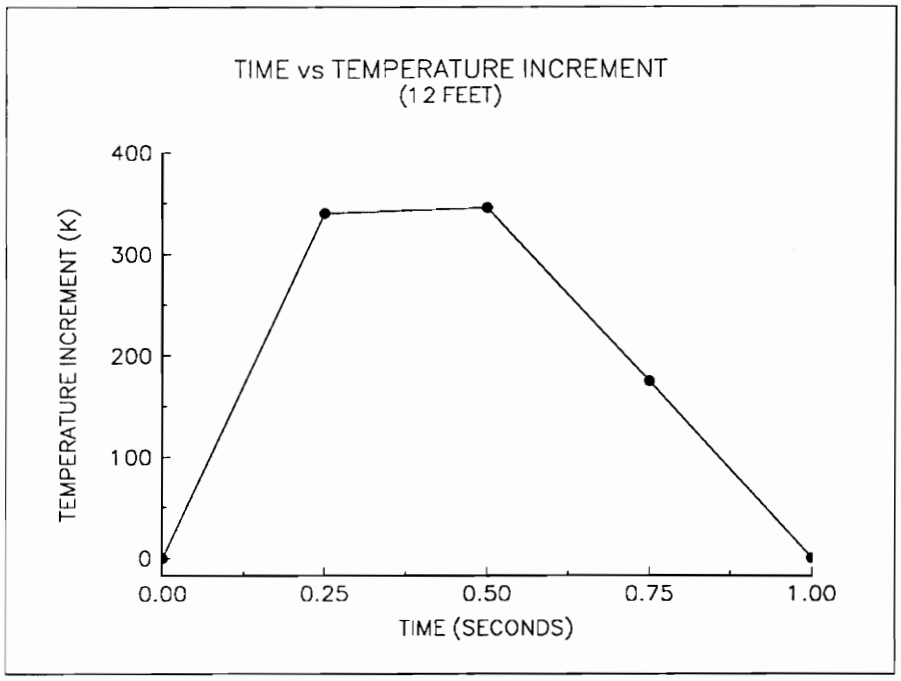

TIME (sec.)	ΔT (K)	RAMP (K/sec)
0.0-0.25	0.0-339.8	1359.2
0.25-0.5	339.8-345.2	21.6
0.5-0.75	345.2-173.9	-685.2
0.75-1.0	173.9-0.0	-695.6

Figure 68. Time vs Maximum Temperature Increment Per Quadrant
(Four Quadrants In Phase, 12 Feet)

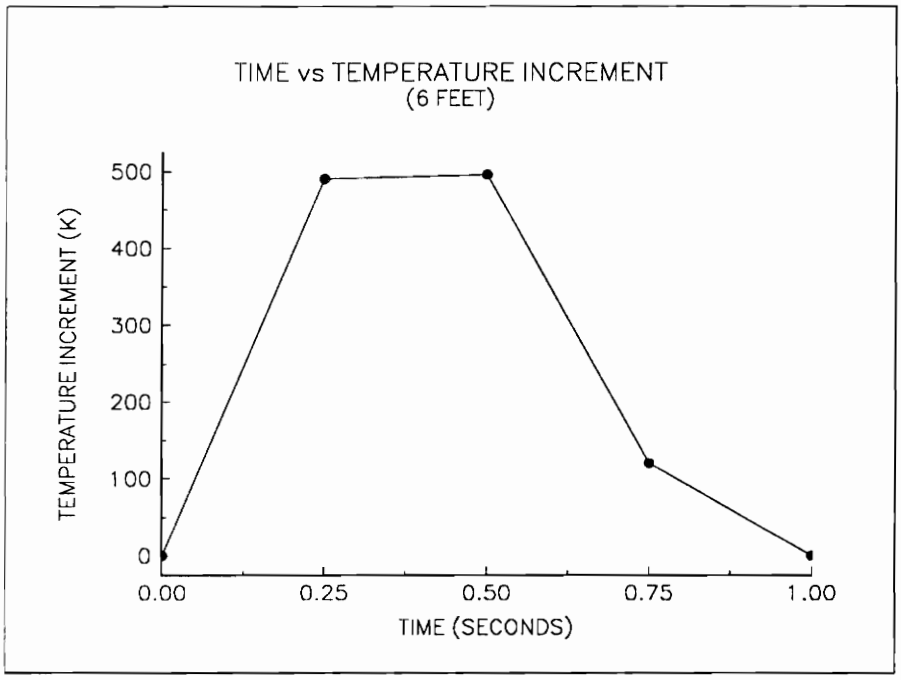

TIME (sec.)	ΔT (K)	RAMP (K/sec)
0.0-0.25	0.0-490.3	1961.2
0.25-0.5	490.3-495.6	21.2
0.5-0.75	495.6-120.6	-1500.0
0.75-1.0	120.6-0.0	-482.4

Figure 69. Time vs Maximum Temperature Increment Per Quadrant
(Four Quadrants Out Of Phase, 6 Feet)

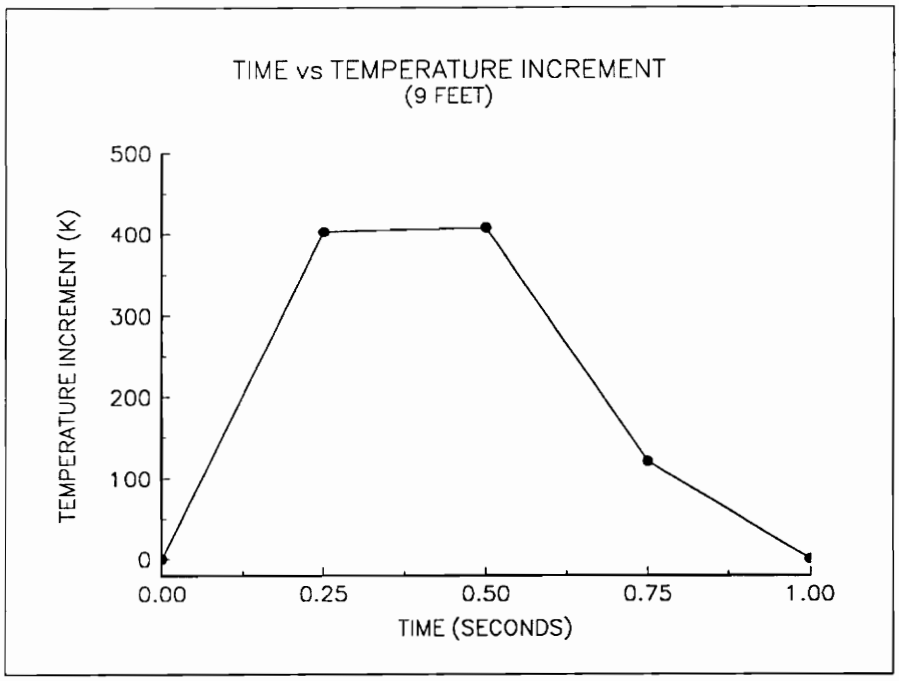

TIME (sec.)	ΔT (K)	RAMP (K/sec)
0.0-0.25	0.0-402.3	1609.2
0.25-0.5	402.3-407.7	21.5
0.5-0.75	407.7-120.7	-1148.2
0.75-1.0	120.7-0.0	-482.8

Figure 70. Time vs Maximum Temperature Increment Per Quadrant
(Four Quadrants Out Of Phase, 9 Feet)

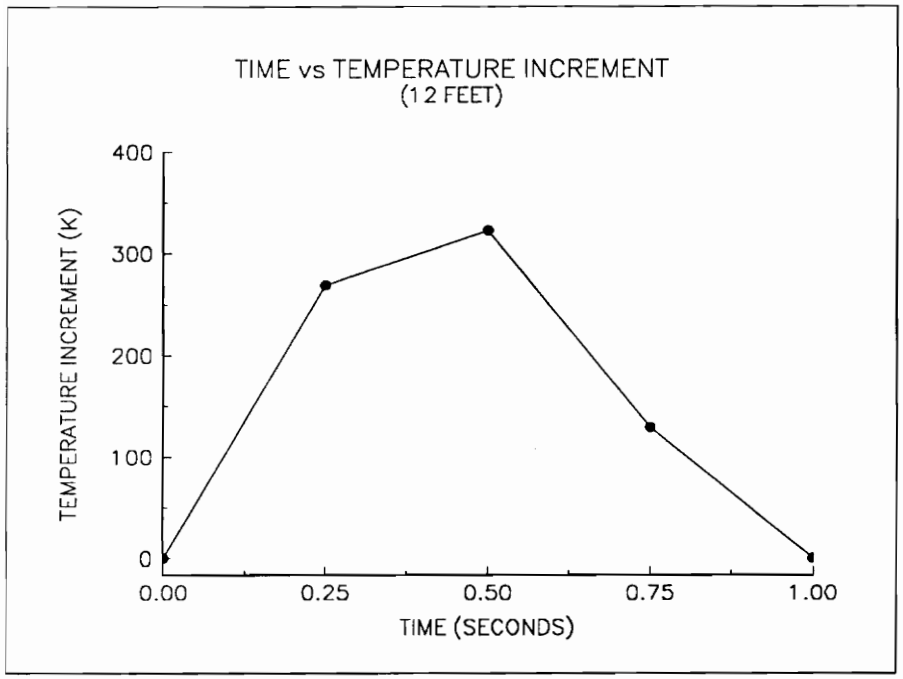

TIME (sec.)	ΔT (K)	RAMP (K/sec)
0.0-0.25	0.0-268.7	1074.6
0.25-0.5	268.7-322.4	214.9
0.5-0.75	322.4-128.9	-774.1
0.75-1.0	128.9-0.0	-515.6

Figure 71. Time vs Maximum Temperature Increment Per Quadrant
(Four Quadrants Out Of Phase, 12 Feet)

Appendix D

Photographs

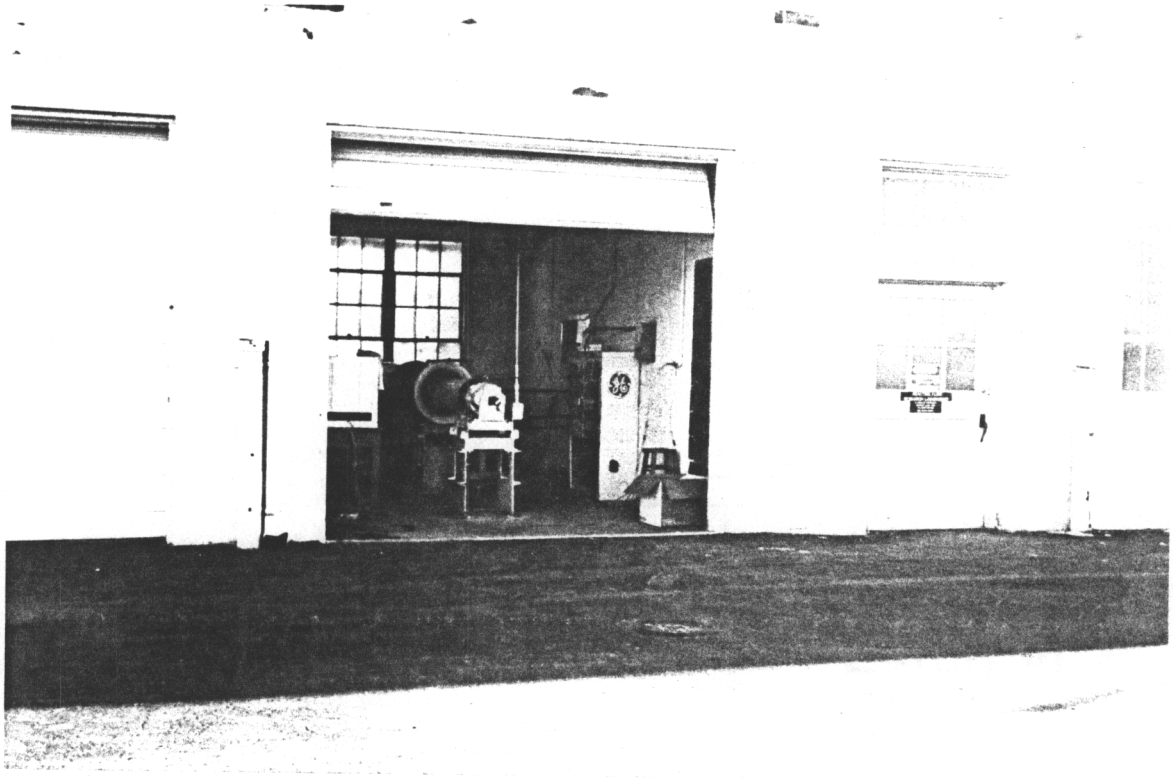

Figure 72. Outside The Test Facility

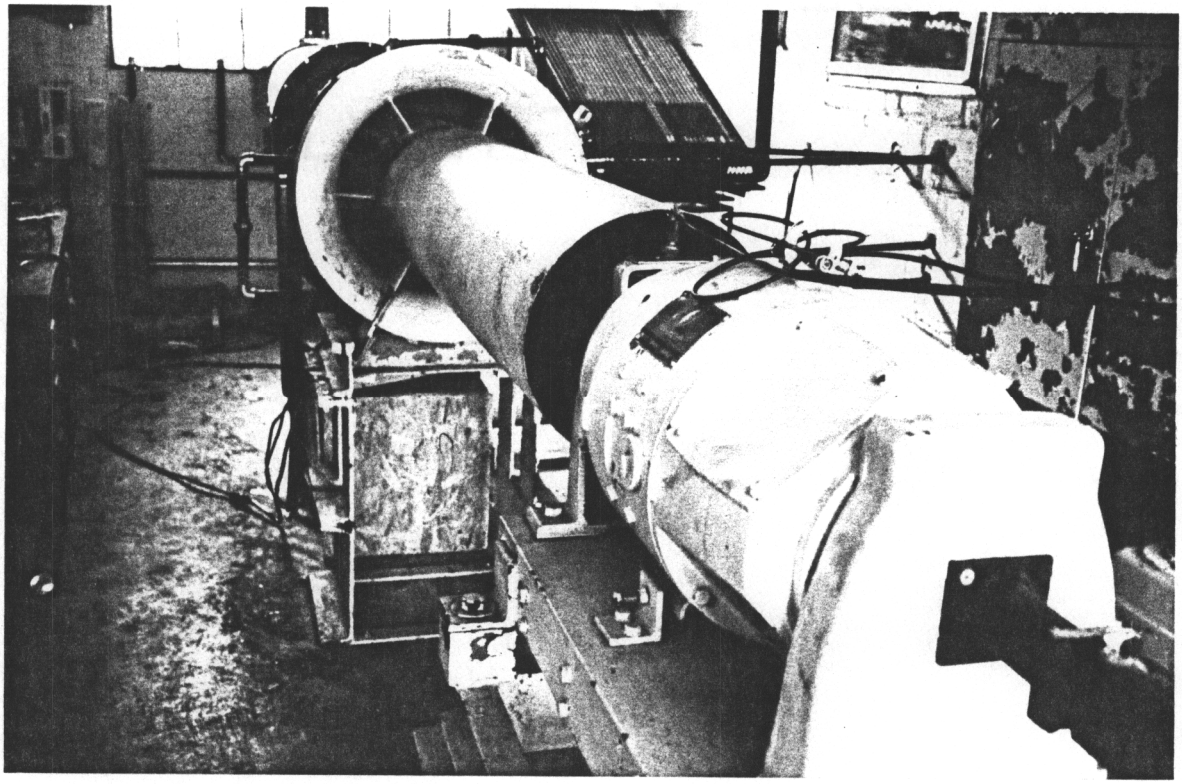

Figure 73. Inside The Test Cell (Front)

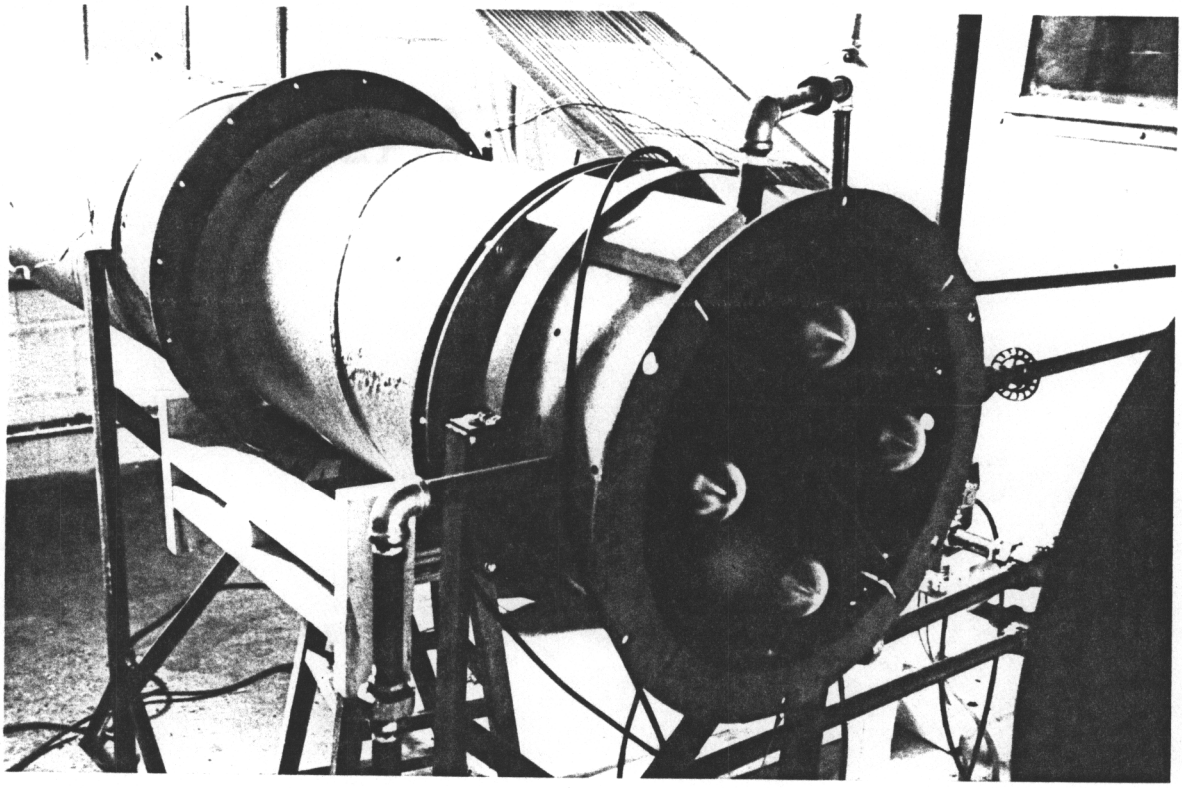

Figure 74. The Thermal Distortion Generator (Left/Front View)

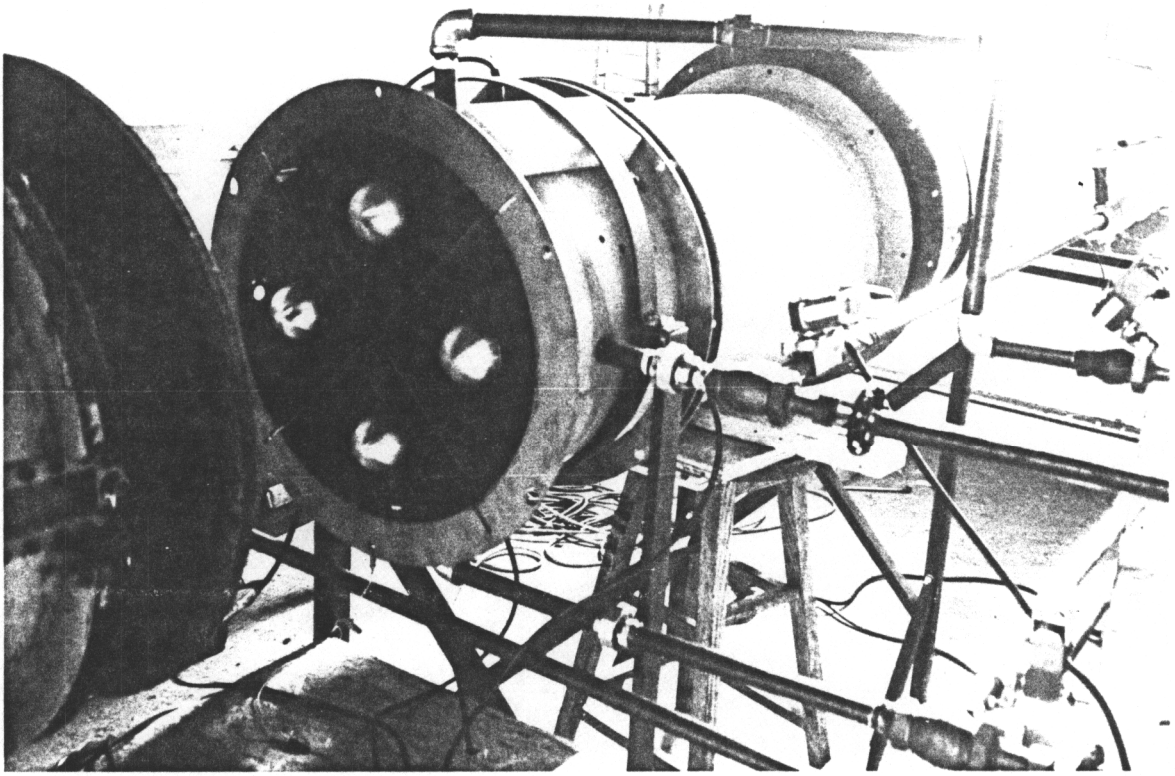

Figure 75. The Thermal Distortion Generator (Right/Front View)

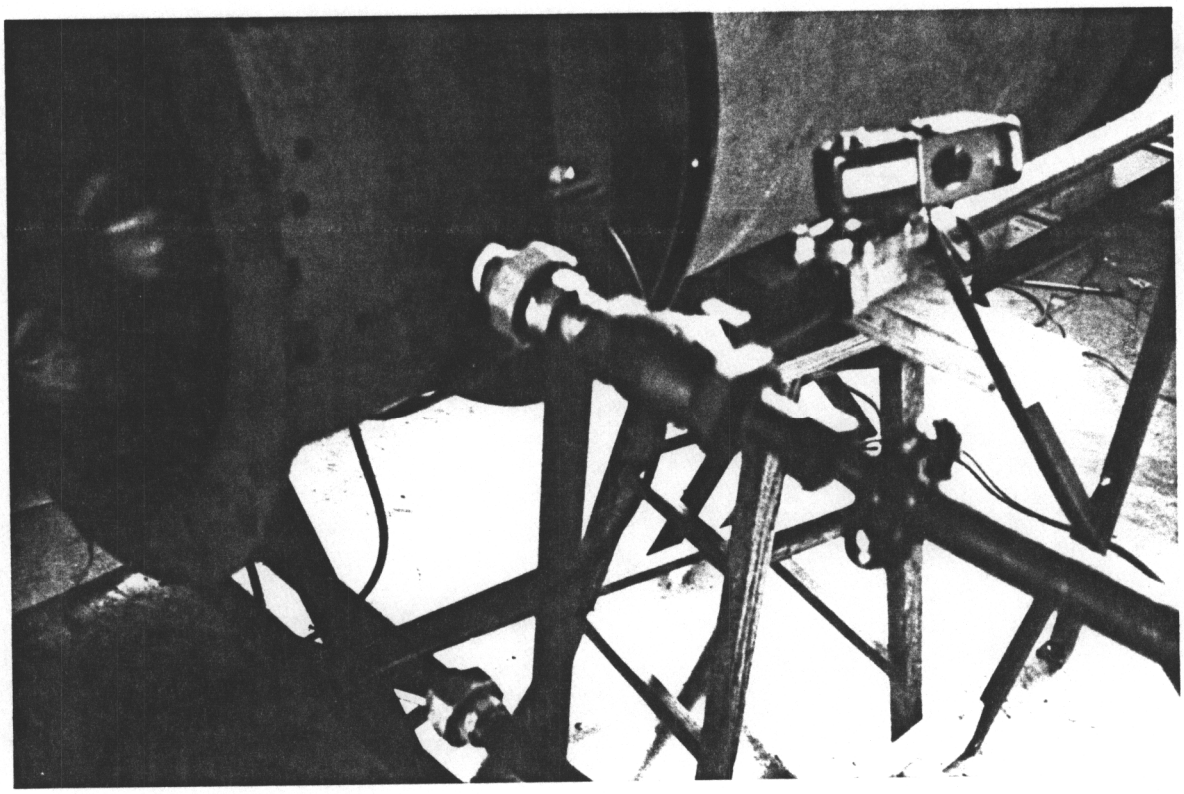

Figure 76. Solenoid And Regulator Valve

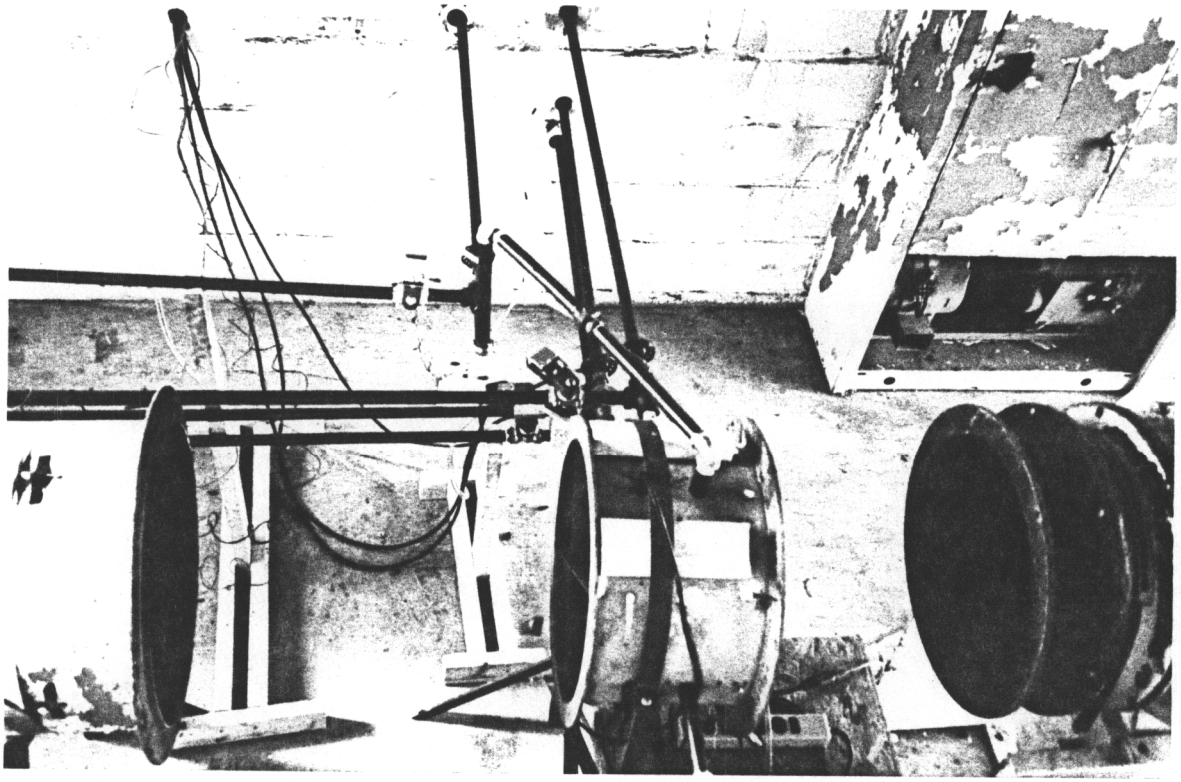

Figure 77. Compressor Exit/Burner Section/Exhaust Duct Inlet (Top View)

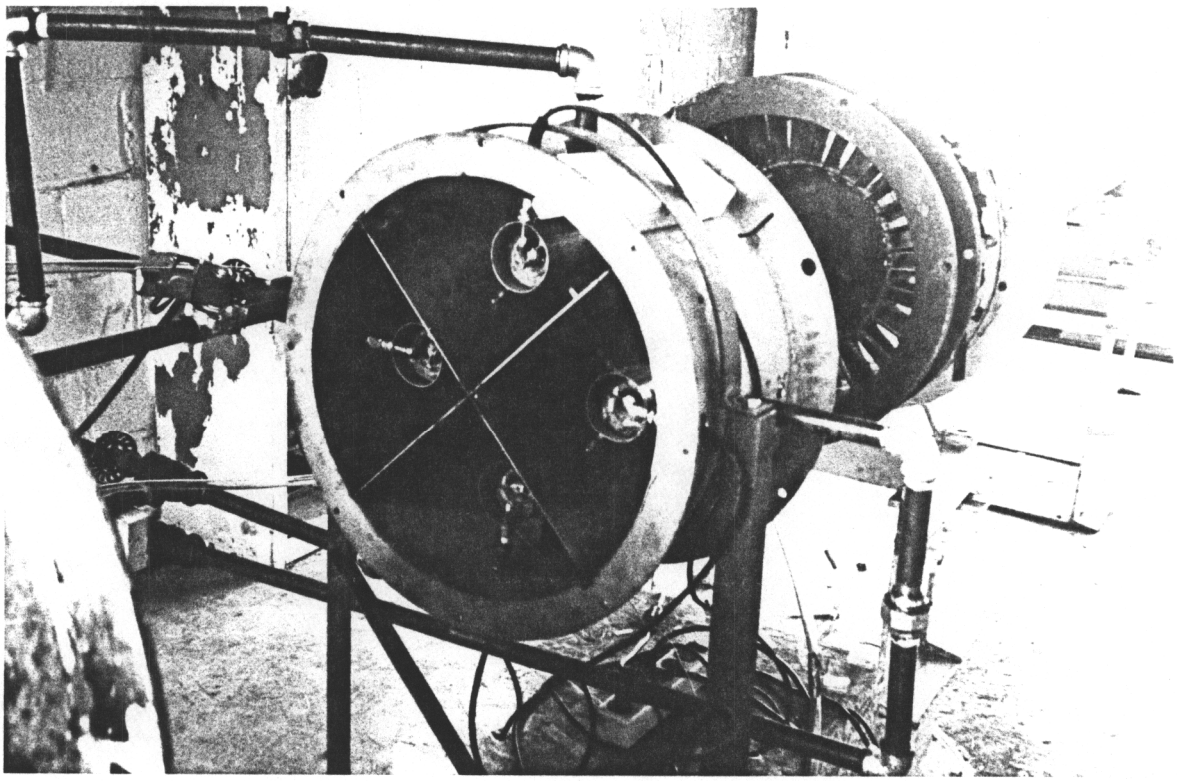

Figure 78. Compressor Exit/Burner Section Exit (Rear View)

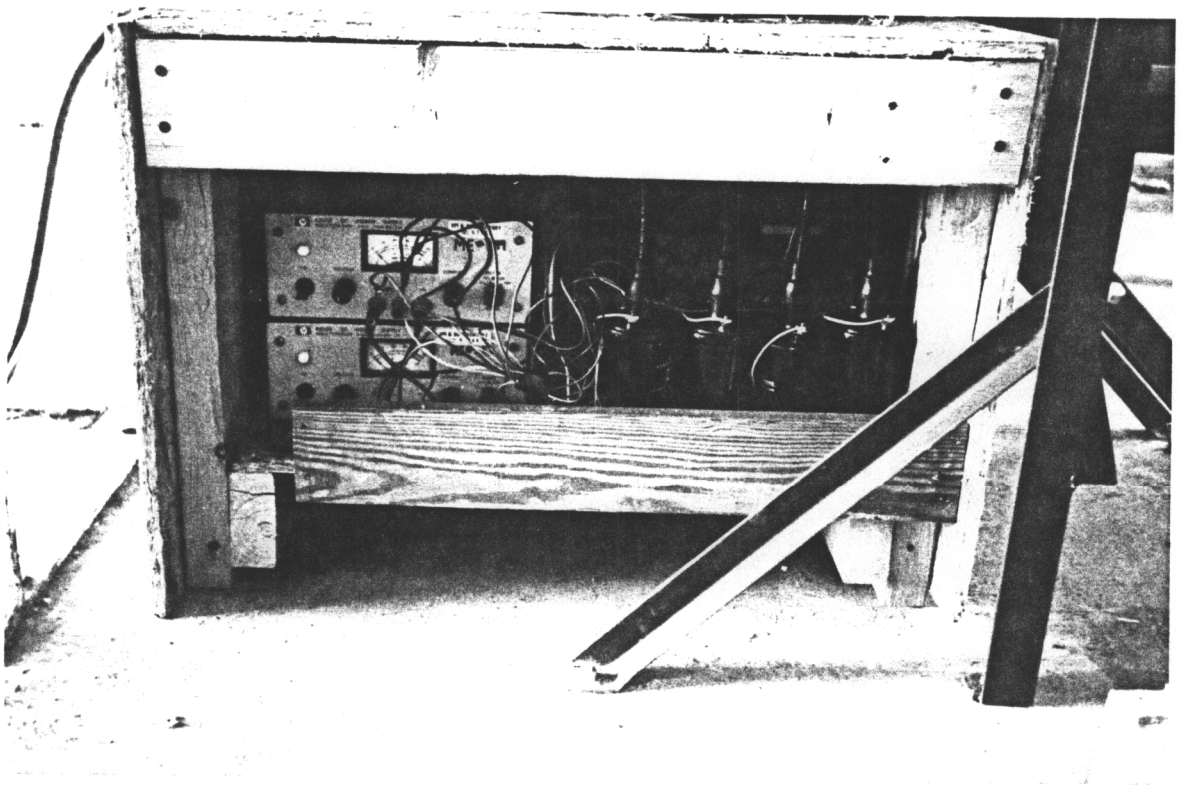

Figure 79. The Ignition System

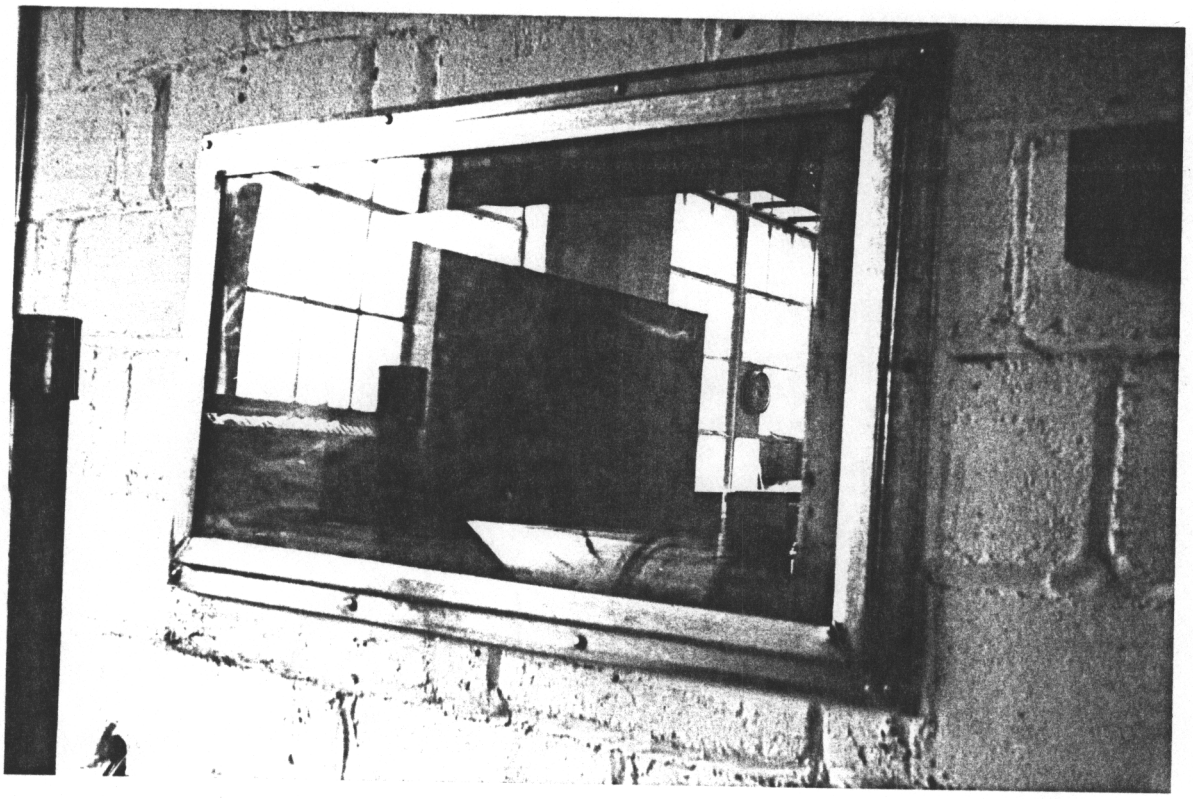

Figure 80. The Installed Window

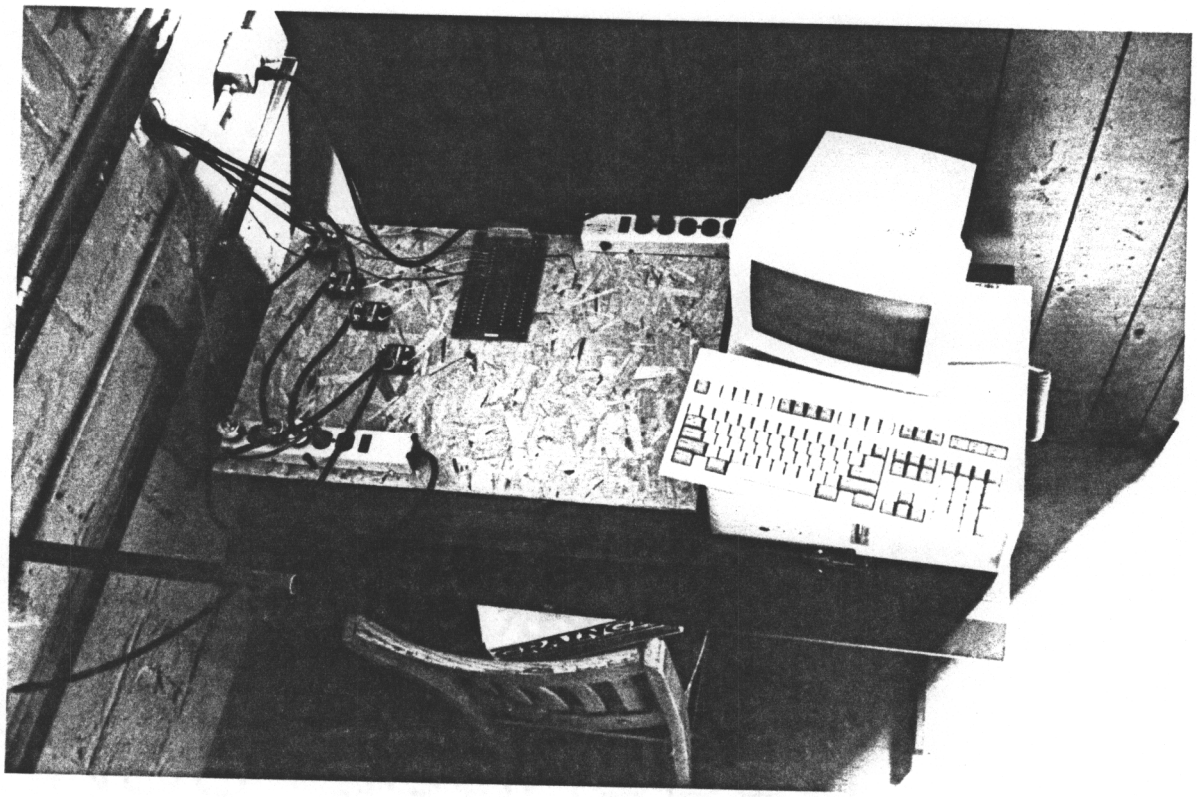

Figure 81. The Control Room

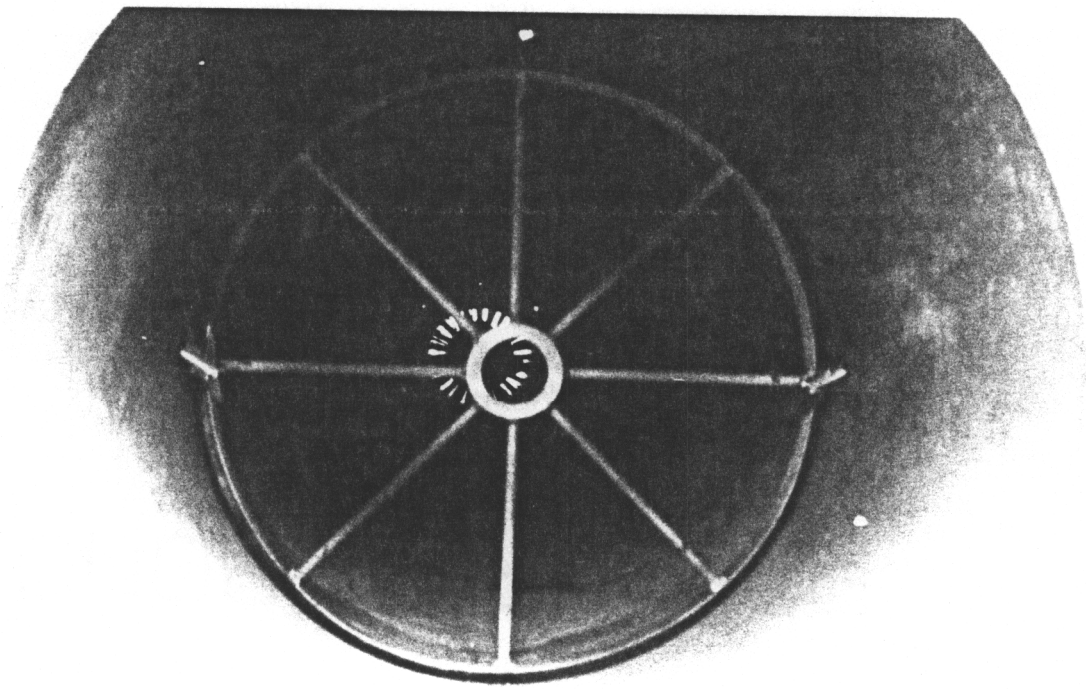

Figure 82. The Thermocouple Rake (Looking Upstream The Exhaust Duct)

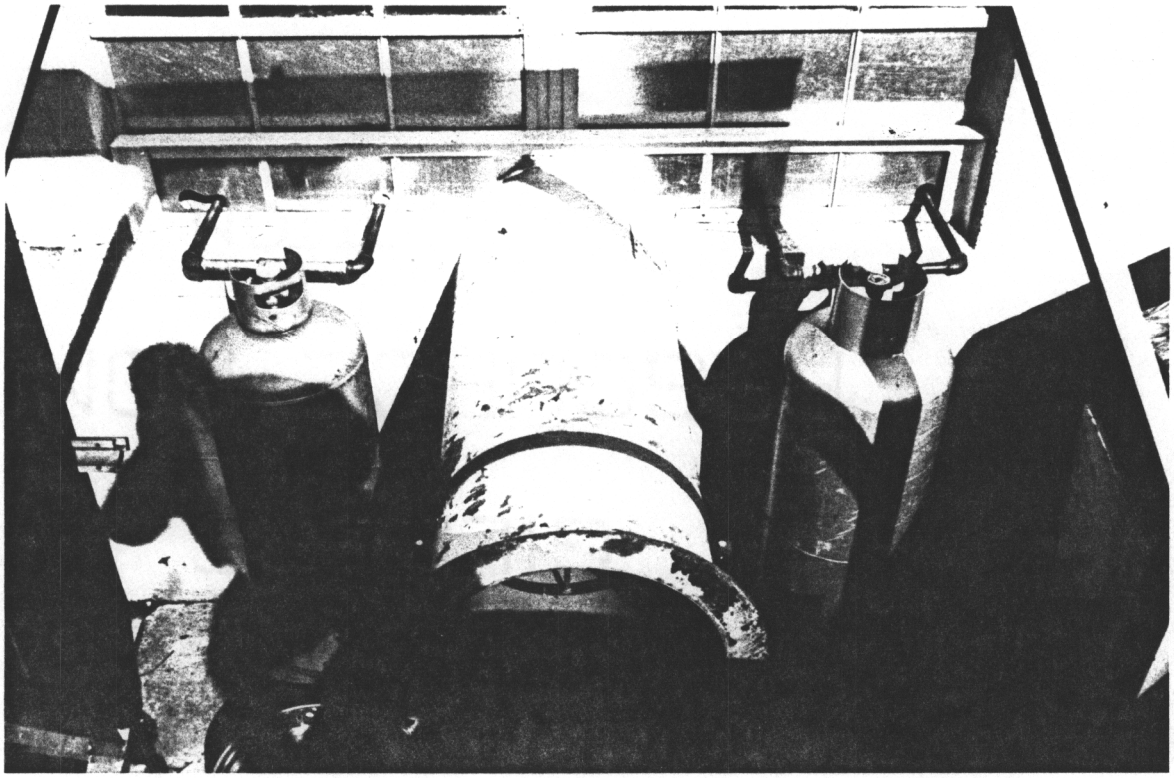

Figure 83. Propane Tanks And Exhaust Duct Exit

Appendix E

Performance Data For Liquid and Solid Rocket Propellants

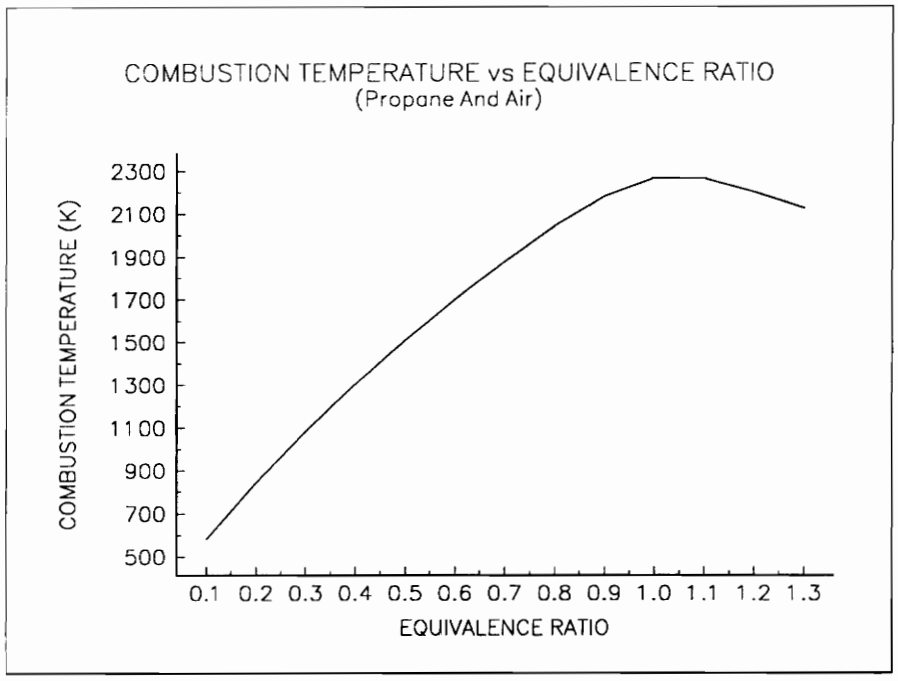

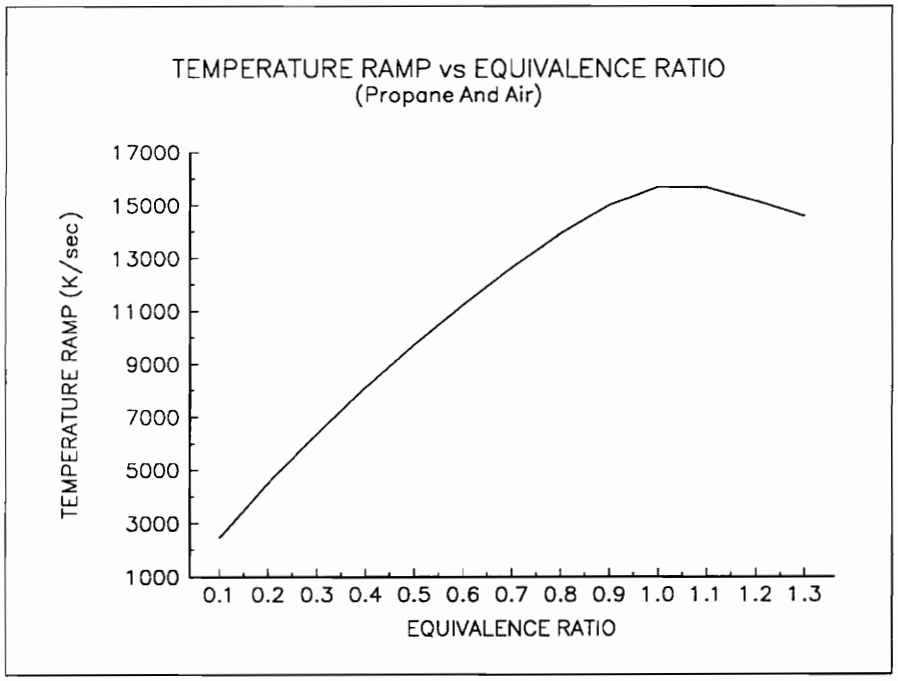

Figure 84. Combustion Temperature/Temperature Ramp vs Equivalence Ratio

Table 1.

Propane/Air Combustion Reaction (Equivalence Ratio=0.1)

Computed properties

Independent atom	population	element potential
C	3.00000000E-01	-8.5145E+01
H	8.00000000E-01	-3.1961E+01
O	1.00000000E+01	-1.3496E+01
N	3.76000000E+01	-1.1959E+01

Products at T = 583.14 K P = 1.000E+00 atmospheres

species	mol fraction in the phase	mol fraction in mixture	mass fraction in mixture	mols*
phase 1: molal mass = 28.794 kg/kmol				
C	.88712E-89	.88712E-89	.37005E-89	2.12908E-88
CH4	.14648E-74	.14648E-74	.81612E-75	3.51547E-74
CO	.45753E-22	.45753E-22	.44508E-22	1.09806E-21
CO2	.12500E-01	.12500E-01	.19106E-01	3.00000E-01
C3H8	.84344-186	.84344-186	.12917-185	2.02426-185
H	.59946E-27	.59946E-27	.20985E-28	1.43871E-26
HO	.39467E-13	.39467E-13	.23312E-13	9.47210E-13
H2	.21670E-20	.21670E-20	.15172E-21	5.20085E-20
H2O	.16667E-01	.16667E-01	.10428E-01	4.00000E-01
N	.45617E-39	.45617E-39	.22192E-39	1.09480E-38
NO	.13984E-07	.13984E-07	.14574E-07	3.35627E-07
NO2	.10667E-06	.10667E-06	.17044E-06	2.56012E-06
N2	.78333E+00	.78333E+00	.76210E+00	1.88000E+01
O	.26700E-19	.26700E-19	.14836E-19	6.40789E-19
O2	.18750E+00	.18750E+00	.20837E+00	4.50000E+00

* Species mols for the atom populations in mols.

Mixture properties: molal mass = 28.794 kg/kmol
T = 583.14 K P = 1.0133E+05 Pa V = 1.6618E+00 m**3/kg
U = -.1834E+06 J/kg H = -.1502E+05 J/kg S = .7623E+04 J/kg-K

Made 7 (T,P) iterations; 16 equilibrium iterations; v 3.89 IBM-PC

Sound speed (isentropic) = 480.9 m/s

Table 2.

Propane/Air Combustion Reaction (Equivalence Ratio=0.2)

Computed properties

Independent atom	population	element potential
C	6.00000000E-01	-5.9609E+01
H	1.60000000E+00	-2.4139E+01
O	1.00000000E+01	-1.3955E+01
N	3.76000000E+01	-1.2341E+01

Products at T = 843.60 K P = 1.000E+00 atmospheres

species	mol fraction in the phase	mol fraction in mixture	mass fraction in mixture	mols*
phase 1: molal mass = 28.738 kg/kmol				
C	.33080E-61	.33080E-61	.13826E-61	8.00531E-61
CH4	.26977E-52	.26977E-52	.15060E-52	6.52840E-52
CO	.66808E-14	.66808E-14	.65116E-14	1.61674E-13
CO2	.24793E-01	.24793E-01	.37969E-01	6.00000E-01
C3H8	.46812-137	.46812-137	.71830-137	1.13285-136
H	.27091E-17	.27091E-17	.95020E-19	6.55603E-17
HO	.16310E-08	.16310E-08	.96524E-09	3.94707E-08
H2	.28376E-13	.28376E-13	.19906E-14	6.86701E-13
H2O	.33058E-01	.33058E-01	.20724E-01	8.00000E-01
N	.62290E-26	.62290E-26	.30362E-26	1.50742E-25
NO	.41343E-05	.41343E-05	.43170E-05	1.00050E-04
NO2	.71470E-06	.71470E-06	.11442E-05	1.72958E-05
N2	.77686E+00	.77686E+00	.75726E+00	1.87999E+01
O	.22780E-12	.22780E-12	.12683E-12	5.51272E-12
O2	.16529E+00	.16529E+00	.18404E+00	3.99993E+00

* Species mols for the atom populations in mols.

Mixture properties: molal mass = 28.738 kg/kmol
T = 843.60 K P = 1.0133E+05 Pa V = 2.4087E+00 m**3/kg
U = -.2739E+06 J/kg H = -.2985E+05 J/kg S = .8070E+04 J/kg-K

Made 6 (T,P) iterations; 15 equilibrium iterations; v 3.89 IBM-PC

Sound speed (isentropic) = 571.6 m/s

Table 3.

Propane/Air Combustion Reaction (Equivalence Ratio=0.3)

Computed properties

Independent atom	population	element potential
C	9.00000000E-01	-4.7018E+01
H	2.40000000E+00	-2.0320E+01
O	1.00000000E+01	-1.4357E+01
N	3.76000000E+01	-1.2658E+01

Products at T = 1081.94 K P = 1.000E+00 atmospheres

species	mol fraction in the phase	mol fraction in mixture	mass fraction in mixture	mols*
phase 1: molal mass = 28.683 kg/kmol				
C	.84728E-46	.84728E-46	.35479E-46	2.06737E-45
CH4	.97472E-41	.97472E-41	.54517E-41	2.37832E-40
CO	.76759E-10	.76759E-10	.74958E-10	1.87291E-09
CO2	.36885E-01	.36885E-01	.56594E-01	9.00000E-01
C3H8	.41887-109	.41887-109	.64396-109	1.02205-108
H	.17800E-12	.17800E-12	.62551E-14	4.34319E-12
HO	.31675E-06	.31675E-06	.18781E-06	7.72871E-06
H2	.10793E-09	.10793E-09	.75855E-11	2.63338E-09
H2O	.49180E-01	.49180E-01	.30890E-01	1.20000E+00
N	.19578E-19	.19578E-19	.95613E-20	4.77709E-19
NO	.65661E-04	.65661E-04	.68693E-04	1.60214E-03
NO2	.16852E-05	.16852E-05	.27030E-05	4.11181E-05
N2	.77046E+00	.77046E+00	.75246E+00	1.87992E+01
O	.59071E-09	.59071E-09	.32950E-09	1.44132E-08
O2	.14341E+00	.14341E+00	.15998E+00	3.49916E+00

* Species mols for the atom populations in mols.

Mixture properties: molal mass = 28.683 kg/kmol
T = 1081.94 K P = 1.0133E+05 Pa V = 3.0952E+00 m**3/kg
U = -.3581E+06 J/kg H = -.4450E+05 J/kg S = .8401E+04 J/kg-K

Made 5 (T,P) iterations; 15 equilibrium iterations; v 3.89 IBM-PC

Sound speed (isentropic) = 642.0 m/s

Table 4.

Propane/Air Combustion Reaction (Equivalence Ratio=0.4)

Computed properties

Independent atom	population	element potential
C	1.20000000E+00	-3.9441E+01
H	3.20000000E+00	-1.8045E+01
O	1.00000000E+01	-1.4714E+01
N	3.76000000E+01	-1.2922E+01

Products at T = 1302.41 K P = 1.000E+00 atmospheres

species	mol fraction in the phase	mol fraction in mixture	mass fraction in mixture	mols*
phase 1: molal mass = 28.629 kg/kmol				
C	.16993E-36	.16993E-36	.71289E-37	4.18018E-36
CH4	.11141E-33	.11141E-33	.62430E-34	2.74067E-33
CO	.22172E-07	.22172E-07	.21693E-07	5.45443E-07
CO2	.48780E-01	.48780E-01	.74986E-01	1.20000E+00
C3H8	.92743E-89	.92743E-89	.14285E-88	2.28147E-88
H	.14817E-09	.14817E-09	.52165E-11	3.64486E-09
HO	.74865E-05	.74865E-05	.44473E-05	1.84167E-04
H2	.16766E-07	.16766E-07	.11806E-08	4.12455E-07
H2O	.65037E-01	.65037E-01	.40926E-01	1.59991E+00
N	.15362E-15	.15362E-15	.75164E-16	3.77907E-15
NO	.33049E-03	.33049E-03	.34640E-03	8.12999E-03
NO2	.26118E-05	.26118E-05	.41972E-05	6.42508E-05
N2	.76406E+00	.76406E+00	.74762E+00	1.87959E+01
O	.63946E-07	.63946E-07	.35737E-07	1.57307E-06
O2	.12178E+00	.12178E+00	.13611E+00	2.99582E+00

* Species mols for the atom populations in mols.

Mixture properties: molal mass = 28.629 kg/kmol
T = 1302.41 K P = 1.0133E+05 Pa V = 3.7329E+00 m**3/kg
U = -.4372E+06 J/kg H = -.5896E+05 J/kg S = .8668E+04 J/kg-K

Made 6 (T,P) iterations; 18 equilibrium iterations; v 3.89 IBM-PC

Sound speed (isentropic) = 700.1 m/s

Table 5.

Propane/Air Combustion Reaction (Equivalence Ratio=0.5)

Computed properties

Independent atom	population	element potential
C	1.50000000E+00	-3.4317E+01
H	4.00000000E+00	-1.6525E+01
O	1.00000000E+01	-1.5044E+01
N	3.76000000E+01	-1.3147E+01

Products at T = 1507.94 K P = 1.000E+00 atmospheres

species	mol fraction in the phase	mol fraction in mixture	mass fraction in mixture	mols*
phase 1: molal mass = 28.576 kg/kmol				
C	.29714E-30	.29714E-30	.12489E-30	7.36915E-30
CH4	.76597E-29	.76597E-29	.43003E-29	1.89964E-28
CO	.10391E-05	.10391E-05	.10186E-05	2.57712E-05
CO2	.60482E-01	.60482E-01	.93148E-01	1.49997E+00
C3H8	.47361E-78	.47361E-78	.73085E-78	1.17457E-77
H	.14054E-07	.14054E-07	.49575E-09	3.48555E-07
HO	.61769E-04	.61769E-04	.36763E-04	1.53189E-03
H2	.53222E-06	.53222E-06	.37547E-07	1.31991E-05
H2O	.80613E-01	.80613E-01	.50823E-01	1.99922E+00
N	.64437E-13	.64437E-13	.31587E-13	1.59806E-12
NO	.93336E-03	.93336E-03	.98014E-03	2.31478E-02
NO2	.32241E-05	.32241E-05	.51908E-05	7.99577E-05
N2	.75758E+00	.75758E+00	.74267E+00	1.87884E+01
O	.14186E-05	.14186E-05	.79431E-06	3.51828E-05
O2	.10032E+00	.10032E+00	.11234E+00	2.48797E+00

* Species mols for the atom populations in mols.

Mixture properties: molal mass = 28.576 kg/kmol
T = 1507.94 K P = 1.0133E+05 Pa V = 4.3300E+00 m**3/kg
U = -.5120E+06 J/kg H = -.7324E+05 J/kg S = .8895E+04 J/kg-K

Made 7 (T,P) iterations; 22 equilibrium iterations; v 3.89 IBM-PC

Sound speed (isentropic) = 749.5 m/s

Table 6.

Propane/Air Combustion Reaction (Equivalence Ratio=0.6)

Computed properties

Independent atom	population	element potential
C	1.80000000E+00	-3.0567E+01
H	4.80000000E+00	-1.5427E+01
O	1.00000000E+01	-1.5363E+01
N	3.76000000E+01	-1.3340E+01

Products at T = 1700.09 K P = 1.000E+00 atmospheres

species	mol fraction in the phase	mol fraction in mixture	mass fraction in mixture	mols*
phase 1: molal mass = 28.522 kg/kmol				
C	.10126E-25	.10126E-25	.42642E-26	2.53169E-25
CH4	.29329E-25	.29329E-25	.16497E-25	7.33300E-25
CO	.17390E-04	.17390E-04	.17078E-04	4.34785E-04
CO2	.71976E-01	.71976E-01	.11106E+00	1.79957E+00
C3H8	.63873E-70	.63873E-70	.98753E-70	1.59697E-69
H	.38373E-06	.38373E-06	.13561E-07	9.59401E-06
HO	.27748E-03	.27748E-03	.16546E-03	6.93749E-03
H2	.68300E-05	.68300E-05	.48276E-06	1.70764E-04
H2O	.95846E-01	.95846E-01	.60542E-01	2.39636E+00
N	.47539E-11	.47539E-11	.23348E-11	1.18858E-10
NO	.18647E-02	.18647E-02	.19618E-02	4.66208E-02
NO2	.33942E-05	.33942E-05	.54752E-05	8.48627E-05
N2	.75100E+00	.75100E+00	.73762E+00	1.87766E+01
O	.12475E-04	.12475E-04	.69981E-05	3.11899E-04
O2	.78994E-01	.78994E-01	.88624E-01	1.97502E+00

* Species mols for the atom populations in mols.

Mixture properties: molal mass = 28.522 kg/kmol
T = 1700.09 K P = 1.0133E+05 Pa V = 4.8911E+00 m**3/kg
U = -.5829E+06 J/kg H = -.8734E+05 J/kg S = .9093E+04 J/kg-K

Made 7 (T,P) iterations; 23 equilibrium iterations; v 3.89 IBM-PC

Sound speed (isentropic) = 792.3 m/s

Table 7.

Propane/Air Combustion Reaction (Equivalence Ratio=0.7)

Computed properties

Independent atom	population	element potential
C	2.10000000E+00	-2.7645E+01
H	5.60000000E+00	-1.4585E+01
O	1.00000000E+01	-1.5691E+01
N	3.76000000E+01	-1.3508E+01

Products at T = 1879.10 K P = 1.000E+00 atmospheres

species	mol fraction in the phase	mol fraction in mixture	mass fraction in mixture	mols*
phase 1: molal mass = 28.463 kg/kmol				
C	.28767E-22	.28767E-22	.12139E-22	7.25173E-22
CH4	.19187E-22	.19187E-22	.10815E-22	4.83681E-22
CO	.15368E-03	.15368E-03	.15124E-03	3.87407E-03
CO2	.83151E-01	.83151E-01	.12857E+00	2.09613E+00
C3H8	.24209E-62	.24209E-62	.37506E-62	6.10277E-62
H	.47657E-05	.47657E-05	.16877E-06	1.20136E-04
HO	.82286E-03	.82286E-03	.49168E-03	2.07431E-02
H2	.50025E-04	.50025E-04	.35432E-05	1.26107E-03
H2O	.11061E+00	.11061E+00	.70011E-01	2.78831E+00
N	.11980E-09	.11980E-09	.58957E-10	3.01991E-09
NO	.28978E-02	.28978E-02	.30550E-02	7.30483E-02
NO2	.30928E-05	.30928E-05	.49992E-05	7.79643E-05
N2	.74433E+00	.74433E+00	.73257E+00	1.87634E+01
O	.59519E-04	.59519E-04	.33458E-04	1.50040E-03
O2	.57919E-01	.57919E-01	.65114E-01	1.46006E+00

* Species mols for the atom populations in mols.

Mixture properties: molal mass = 28.463 kg/kmol
T = 1879.10 K P = 1.0133E+05 Pa V = 5.4172E+00 m**3/kg
U = -.6502E+06 J/kg H = -.1013E+06 J/kg S = .9269E+04 J/kg-K

Made 9 (T,P) iterations; 30 equilibrium iterations; v 3.89 IBM-PC

Sound speed (isentropic) = 828.9 m/s

Table 8.

Propane/Air Combustion Reaction (Equivalence Ratio=0.8)

Computed properties

Independent atom	population	element potential
C	2.40000000E+00	-2.5243E+01
H	6.40000000E+00	-1.3906E+01
O	1.00000000E+01	-1.6055E+01
N	3.76000000E+01	-1.3652E+01

Products at T = 2042.12 K P = 1.000E+00 atmospheres

species	mol fraction in the phase	mol fraction in mixture	mass fraction in mixture	mols*
phase 1: molal mass = 28.390 kg/kmol				
C	.14597E-19	.14597E-19	.61756E-20	3.71189E-19
CH4	.40380E-20	.40380E-20	.22819E-20	1.02682E-19
CO	.88941E-03	.88941E-03	.87752E-03	2.26167E-02
CO2	.93492E-01	.93492E-01	.14493E+00	2.37738E+00
C3H8	.71945E-57	.71945E-57	.11175E-56	1.82947E-56
H	.34156E-04	.34156E-04	.12127E-05	8.68550E-04
HO	.18032E-02	.18032E-02	.10803E-02	4.58546E-02
H2	.25336E-03	.25336E-03	.17991E-04	6.44258E-03
H2O	.12467E+00	.12467E+00	.79114E-01	3.17020E+00
N	.13854E-08	.13854E-08	.68356E-09	3.52284E-08
NO	.37239E-02	.37239E-02	.39361E-02	9.46935E-02
NO2	.23608E-05	.23608E-05	.38259E-05	6.00332E-05
N2	.73745E+00	.73745E+00	.72767E+00	1.87526E+01
O	.17643E-03	.17643E-03	.99430E-04	4.48631E-03
O2	.37502E-01	.37502E-01	.42269E-01	9.53633E-01

* Species mols for the atom populations in mols.

Mixture properties: molal mass = 28.390 kg/kmol
T = 2042.12 K P = 1.0133E+05 Pa V = 5.9023E+00 m**3/kg
U = -.7131E+06 J/kg H = -.1150E+06 J/kg S = .9427E+04 J/kg-K

Made 9 (T,P) iterations; 30 equilibrium iterations; v 3.89 IBM-PC

Sound speed (isentropic) = 858.4 m/s

Table 9.

Propane/Air Combustion Reaction (Equivalence Ratio=0.9)

Computed properties

Independent atom	population	element potential
C	2.70000000E+00	-2.3157E+01
H	7.20000000E+00	-1.3326E+01
O	1.00000000E+01	-1.6509E+01
N	3.76000000E+01	-1.3769E+01

Products at T = 2179.62 K P = 1.000E+00 atmospheres

species	mol fraction in the phase	mol fraction in mixture	mass fraction in mixture	mols*
phase 1: molal mass = 28.276 kg/kmol				
C	.19386E-17	.19386E-17	.82348E-18	4.97977E-17
CH4	.41252E-18	.41252E-18	.23405E-18	1.05965E-17
CO	.37785E-02	.37785E-02	.37430E-02	9.70595E-02
CO2	.10133E+00	.10133E+00	.15772E+00	2.60294E+00
C3H8	.20079E-51	.20079E-51	.31314E-51	5.15781E-51
H	.15777E-03	.15777E-03	.56240E-05	4.05259E-03
HO	.29326E-02	.29326E-02	.17639E-02	7.53321E-02
H2	.99800E-03	.99800E-03	.71155E-04	2.56361E-02
H2O	.13760E+00	.13760E+00	.87674E-01	3.53467E+00
N	.82153E-08	.82153E-08	.40699E-08	2.11029E-07
NO	.37011E-02	.37011E-02	.39278E-02	9.50705E-02
NO2	.13563E-05	.13563E-05	.22069E-05	3.48402E-05
N2	.73003E+00	.73003E+00	.72325E+00	1.87524E+01
O	.32578E-03	.32578E-03	.18434E-03	8.36839E-03
O2	.19145E-01	.19145E-01	.21665E-01	4.91774E-01

* Species mols for the atom populations in mols.

Mixture properties: molal mass = 28.276 kg/kmol
T = 2179.62 K P = 1.0133E+05 Pa V = 6.3252E+00 m**3/kg
U = -.7695E+06 J/kg H = -.1286E+06 J/kg S = .9571E+04 J/kg-K

Made 13 (T,P) iterations; 43 equilibrium iterations; v 3.89 IBM-PC

Sound speed (isentropic) = 878.2 m/s

Table 10.

Propane/Air Combustion Reaction (Equivalence Ratio=1.0)

Computed properties

Independent atom	population	element potential
C	3.00000000E+00	-2.1198E+01
H	8.00000000E+00	-1.2787E+01
O	1.00000000E+01	-1.7174E+01
N	3.76000000E+01	-1.3843E+01

Products at T = 2267.09 K P = 1.000E+00 atmospheres

species	mol fraction in the phase	mol fraction in mixture	mass fraction in mixture	mols*
phase 1: molal mass = 28.062 kg/kmol				
C	.68200E-16	.68200E-16	.29190E-16	1.77594E-15
CH4	.29223E-16	.29223E-16	.16707E-16	7.60984E-16
CO	.12498E-01	.12498E-01	.12475E-01	3.25447E-01
CO2	.10271E+00	.10271E+00	.16108E+00	2.67455E+00
C3H8	.38905E-47	.38905E-47	.61135E-47	1.01309E-46
H	.46807E-03	.46807E-03	.16813E-04	1.21885E-02
HO	.32037E-02	.32037E-02	.19416E-02	8.34247E-02
H2	.33326E-02	.33326E-02	.23942E-03	8.67815E-02
H2O	.14844E+00	.14844E+00	.95299E-01	3.86541E+00
N	.22715E-07	.22715E-07	.11339E-07	5.91510E-07
NO	.24630E-02	.24630E-02	.26338E-02	6.41378E-02
NO2	.44149E-06	.44149E-06	.72383E-06	1.14966E-05
N2	.72073E+00	.72073E+00	.71948E+00	1.87679E+01
O	.31029E-03	.31029E-03	.17691E-03	8.07996E-03
O2	.58442E-02	.58442E-02	.66641E-02	1.52185E-01

* Species mols for the atom populations in mols.

Mixture properties: molal mass = 28.062 kg/kmol
T = 2267.09 K P = 1.0133E+05 Pa V = 6.6291E+00 m**3/kg
U = -.8138E+06 J/kg H = -.1421E+06 J/kg S = .9701E+04 J/kg-K

Made 7 (T,P) iterations; 28 equilibrium iterations; v 3.89 IBM-PC

Sound speed (isentropic) = 889.8 m/s

Table 11.

Propane/Air Combustion Reaction (Equivalence Ratio=1.1)

Computed properties

Independent atom	population	element potential
C	3.30000000E+00	-1.9265E+01
H	8.80000000E+00	-1.2259E+01
O	1.00000000E+01	-1.8196E+01
N	3.76000000E+01	-1.3852E+01

Products at T = 2265.45 K P = 1.000E+00 atmospheres

species	mol fraction in the phase	mol fraction in mixture	mass fraction in mixture	mols*
phase 1: molal mass = 27.668 kg/kmol				
C	.45782E-15	.45782E-15	.19875E-15	1.21648E-14
CH4	.16658E-14	.16658E-14	.96588E-15	4.42607E-14
CO	.31151E-01	.31151E-01	.31537E-01	8.27702E-01
CO2	.93045E-01	.93045E-01	.14800E+00	2.47230E+00
C3H8	.86955E-43	.86955E-43	.13859E-42	2.31048E-42
H	.78599E-03	.78599E-03	.28635E-04	2.08845E-02
HO	.19489E-02	.19489E-02	.11980E-02	5.17838E-02
H2	.95626E-02	.95626E-02	.69678E-03	2.54087E-01
H2O	.15466E+00	.15466E+00	.10071E+00	4.10958E+00
N	.22090E-07	.22090E-07	.11184E-07	5.86943E-07
NO	.87433E-03	.87433E-03	.94829E-03	2.32319E-02
NO2	.56487E-07	.56487E-07	.93931E-07	1.50091E-06
N2	.70710E+00	.70710E+00	.71594E+00	1.87884E+01
O	.11050E-03	.11050E-03	.63904E-04	2.93619E-03
O2	.75586E-03	.75586E-03	.87419E-03	2.00841E-02

* Species mols for the atom populations in mols.

Mixture properties: molal mass = 27.668 kg/kmol
T = 2265.45 K P = 1.0133E+05 Pa V = 6.7188E+00 m**3/kg
U = -.8361E+06 J/kg H = -.1553E+06 J/kg S = .9819E+04 J/kg-K

Made 13 (T,P) iterations; 57 equilibrium iterations; v 3.89 IBM-PC

Sound speed (isentropic) = 905.3 m/s

Table 12.

Propane/Air Combustion Reaction (Equivalence Ratio=1.2)

Computed properties

Independent atom	population	element potential
C	3.60000000E+00	-1.7705E+01
H	9.60000000E+00	-1.1835E+01
O	1.00000000E+01	-1.9284E+01
N	3.76000000E+01	-1.3814E+01

Products at T = 2201.12 K P = 1.000E+00 atmospheres

species	mol fraction in the phase	mol fraction in mixture	mass fraction in mixture	mols*
phase 1: molal mass = 27.161 kg/kmol				
C	.67535E-15	.67535E-15	.29865E-15	1.83888E-14
CH4	.38689E-13	.38689E-13	.22852E-13	1.05344E-12
CO	.53595E-01	.53595E-01	.55271E-01	1.45933E+00
CO2	.78618E-01	.78618E-01	.12739E+00	2.14067E+00
C3H8	.18980E-39	.18980E-39	.30814E-39	5.16800E-39
H	.80450E-03	.80450E-03	.29856E-04	2.19055E-02
HO	.85686E-03	.85686E-03	.53653E-03	2.33311E-02
H2	.20301E-01	.20301E-01	.15068E-02	5.52767E-01
H2O	.15515E+00	.15515E+00	.10291E+00	4.22461E+00
N	.10353E-07	.10353E-07	.53394E-08	2.81899E-07
NO	.23996E-03	.23996E-03	.26511E-03	6.53382E-03
NO2	.54161E-08	.54161E-08	.91742E-08	1.47473E-07
N2	.69033E+00	.69033E+00	.71199E+00	1.87967E+01
O	.23752E-04	.23752E-04	.13991E-04	6.46724E-04
O2	.77216E-04	.77216E-04	.90968E-04	2.10248E-03

* Species mols for the atom populations in mols.

Mixture properties: molal mass = 27.161 kg/kmol
T = 2201.12 K P = 1.0133E+05 Pa V = 6.6497E+00 m**3/kg
U = -.8422E+06 J/kg H = -.1685E+06 J/kg S = .9924E+04 J/kg-K

Made 12 (T,P) iterations; 129 equilibrium iterations; v 3.89 IBM-PC

Sound speed (isentropic) = 912.0 m/s

Table 13.

Propane/Air Combustion Reaction (Equivalence Ratio=1.3)

Computed properties

Independent atom	population	element potential
C	3.90000000E+00	-1.6516E+01
H	1.04000000E+01	-1.1521E+01
O	1.00000000E+01	-2.0251E+01
N	3.76000000E+01	-1.3765E+01

Products at T = 2124.64 K P = 1.000E+00 atmospheres

species	mol fraction in the phase	mol fraction in mixture	mass fraction in mixture	mols*
phase 1: molal mass = 26.651 kg/kmol				
C	.50286E-15	.50286E-15	.22663E-15	1.40377E-14
CH4	.39386E-12	.39386E-12	.23709E-12	1.09948E-11
CO	.73473E-01	.73473E-01	.77222E-01	2.05106E+00
CO2	.66233E-01	.66233E-01	.10937E+00	1.84894E+00
C3H8	.52839E-37	.52839E-37	.87429E-37	1.47505E-36
H	.66473E-03	.66473E-03	.25141E-04	1.85564E-02
HO	.36723E-03	.36723E-03	.23435E-03	1.02516E-02
H2	.33940E-01	.33940E-01	.25674E-02	9.47452E-01
H2O	.15182E+00	.15182E+00	.10263E+00	4.23814E+00
N	.39729E-08	.39729E-08	.20882E-08	1.10907E-07
NO	.70730E-04	.70730E-04	.79641E-04	1.97449E-03
NO2	.63651E-09	.63651E-09	.10988E-08	1.77687E-08
N2	.67342E+00	.67342E+00	.70785E+00	1.87990E+01
O	.51185E-05	.51185E-05	.30729E-05	1.42887E-04
O2	.98091E-05	.98091E-05	.11778E-04	2.73829E-04

* Species mols for the atom populations in mols.

Mixture properties: molal mass = 26.651 kg/kmol
T = 2124.64 K P = 1.0133E+05 Pa V = 6.5416E+00 m**3/kg
U = -.8442E+06 J/kg H = -.1814E+06 J/kg S = .1002E+05 J/kg-K

Made 10 (T,P) iterations; 269 equilibrium iterations; v 3.89 IBM-PC

Sound speed (isentropic) = 909.5 m/s

Table 14.

CALCULATED PERFORMANCE OF LIQUID FLUORINE/LIQUID HYDROGEN (FROZEN EQUILIBRIUM)

P_c = 500 psia, O/F = 5.665, per cent fuel = 15.00, c^* = 8210 ft/sec

P_c/P_e	1.0	1.8342†	34.023	100	200	400	600	800
T(°K)	3371	2932	1423.0	1061	874	716.8	637.9	587.1
γ	1.294	1.303	1.361	1.385	1.396	1.403	1.405	1.406
ϵ		1.000	4.384	8.904	14.159	22.626	29.821	36.301
C_f		0.711	1.459	1.575	1.630	1.674	1.696	1.709
$I_{sp,sec}$		181.3	372.3	401.9	416.0	427.2	432.7	436.2

† Throat conditions.

CALCULATED PERFORMANCE OF SOME LIQUID PROPELLANTS (FROZEN EQUILIBRIUM)

F_2/H_2

P_c = 500 psia, O/F = 4.712, per cent fuel = 17.51, c^* = 8276 ft/sec

P_c/P_e	1.0	1.835†	34.022	100	200	400	800
T, °K	3097	2694	1302	970	798	655	537
γ	1.295	1.304	1.364	1.386	1.395	1.399	1.402
ϵ		1.000	4.368	8.860	14.092	22.532	36.194
C_f		0.711	1.458	1.574	1.628	1.672	1.707
$I_{sp,sec}$		182.8	375.1	404.8	418.9	430.1	439.2

O_2/H_2

P_c = 500 psia, O/F = 3.175, per cent fuel = 23.95, c^* = 7976 ft/sec

P_c/P_e	1.0	1.802†	34.022	100	200	400	800
T, °K	2580	2297	1227	951	802	673	562
γ	1.242	1.249	1.299	1.321	1.334	1.344	1.353
ϵ		1.000	4.743	9.941	16.137	26.283	42.906
C_f		0.693	1.475	1.602	1.664	1.715	1.756
$I_{sp,sec}$		171.9	365.6	397.2	412.6	425.2	435.4

Table 14. (continued)

90% H_2O_2—10% $H_2O/CH_{1.953}$

P_c = 500 psia, O/F = 6.462, per cent fuel = 13.40, c^* = 5242 ft/sec

P_c/P_e	1.0	1.767†	34.022	100	200	400	800
T, °K	2735	2496	1514	1242	1087	947	821
γ	1.189	1.192	1.218	1.232	1.242	1.254	1.266
ϵ		1.000	5.263	11.574	19.401	32.614	54.939
C_F		0.675	1.497	1.642	1.715	1.777	1.829
$I_{opt,sec}$		110.0	243.9	267.5	279.5	289.6	298.1

F_2/NH_3

P_c = 500 psia, O/F = 3.012, per cent fuel = 24.93, c^* = 6808 ft/sec

P_c/P_e	1.0	1.840†	34.022	100	200	400	800
T, °K	4354	3770	1825	1367	1128	925	756
γ	1.306	1.313	1.354	1.377	1.392	1.405	1.415
ϵ		1.000	4.378	8.930	14.229	22.737	36.401
C_F		0.713	1.458	1.574	1.630	1.674	1.709
$I_{opt,sec}$		151.0	308.6	333.1	344.8	354.2	361.7

F_2/N_2H_4

P_c = 500 psia, O/F = 1.897, per cent fuel = 34.52, c^* = 6899 ft/sec

P_c/P_e	1.0	1.842†	34.022	100	200	400	800
T, °K	4401	3807	1840	1380	1138	935	764
γ	1.308	1.314	1.354	1.376	1.391	1.404	1.414
ϵ		1.000	4.373	8.926	14.230	22.748	36.427
C_F		0.714	1.458	1.574	1.630	1.674	1.709
$I_{opt,sec}$		153.1	312.7	337.6	349.4	358.9	366.5

F_2/H_2O

P_c = 500 psia, O/F = 2.1, per cent fuel = 32.26, c^* = 5186 ft/sec

P_c/P_e	1.0	1.833†	34.022	100	200	400	800
T, °K	2967	2583	1264	950	786	649	534
γ	1.292	1.300	1.351	1.371	1.380	1.387	1.393
ϵ		1.000	4.415	9.024	14.425	23.165	37.337
C_F		0.710	1.460	1.577	1.633	1.678	1.714
$I_{opt,sec}$		114.4	235.3	254.2	263.3	270.5	276.3

Table 14. (continued)

80% F_2—20% O_2/80% $C_2N_2H_8$—20% $CH_{1.953}$

P_c = 500 psia, O/F = 3.11, per cent fuel = 24.33, c^* = 6655 ft/sec

P_c/P_e	1.0	1.842†	34.022	100	200	400	800
T, °K	4472	3867	1872	1406	1163	956	783
γ	1.310	1.315	1.351	1.371	1.385	1.399	1.410
ϵ		1.000	4.378	8.957	14.302	22.906	36.743
C_F		0.714	1.458	1.575	1.630	1.675	1.710
$I_{spt,sec}$		147.8	301.7	325.7	337.2	346.4	353.8

80% F_2—20% O_2/$C_2N_2H_8$

P_c = 500 psia, O/F = 2.78, per cent fuel = 26.46, c^* = 6723 ft/sec

P_c/P_e	1.0	1.841†	34.022	100	200	400	800
T, °K	4450	3849	1866	1403	1160	954	782
γ	1.308	1.314	1.350	1.371	1.385	1.398	1.409
ϵ		1.000	4.385	8.971	14.328	22.950	36.825
C_F		0.714	1.459	1.575	1.631	1.675	1.711
$I_{spt,sec}$		149.2	304.8	329.1	340.7	350.0	357.5

70% F_2—30% O_2/$CH_{1.953}$

P_c = 500 psia, O/F = 4.01, per cent fuel = 19.96, c^* = 6482 ft/sec

P_c/P_e	1.0	1.841†	34.022	100	200	400	800
T, °K	4433	3834	1860	1399	1158	954	783
γ	1.309	1.315	1.348	1.368	1.382	1.395	1.406
ϵ		1.000	4.387	8.984	14.363	23.030	37.005
C_F		0.714	1.459	1.575	1.631	1.676	1.711
$I_{spt,sec}$		143.9	293.9	317.3	328.6	337.6	344.8

40% F_2—60% O_2/$C_2N_2H_8$

P_c = 500 psia, O/F = 1.663, per cent fuel = 37.55, c^* = 6285 ft/sec

P_c/P_e	1.0	1.813†	34.022	100	200	400	800
T, °K	3645	3217	1686	1306	1102	924	771
γ	1.264	1.268	1.301	1.319	1.333	1.347	1.359
ϵ		1.000	4.676	9.813	15.938	25.951	42.324
C_F		0.700	1.471	1.596	1.658	1.708	1.748
$I_{spt,sec}$		136.7	287.4	311.9	323.9	333.7	341.6

Table 14. (continued)

PROPERTIES OF AVAILABLE OXIDIZERS

Oxidizer	Available oxygen wt.%	Density lb/in³	Heat of formation kcal/100g	*Moles of gas per 100g
$KClO_4$	46.0	0.090	−32	0
KNO_3	39.5	0.076	−118	0.495
NH_4ClO_4	34.0	0.070	−59	2.55
NH_4NO_3	20.0	0.061	−110	3.75
$LiClO_4$	60.6	0.087	−86.5	0

* Gas produced by the oxidizer other than that formed by the reaction of oxygen with fuel components.

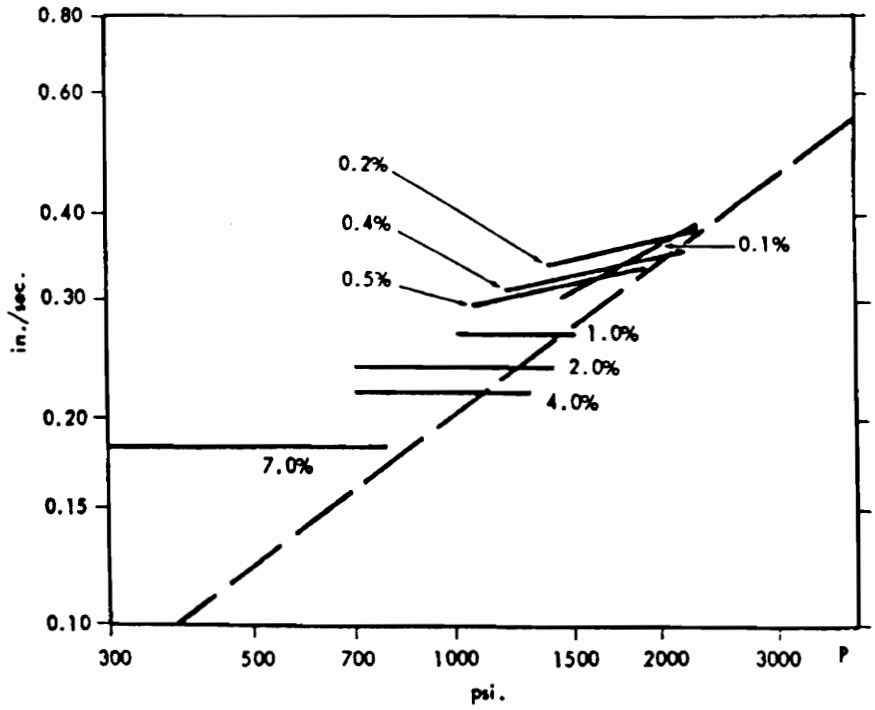

Burning rate as a function of pressure for double base propellants containing x wt.% of lead stearate. Dashed curve is the unmodified propellant cal. val. = 800 cal/g.

Ref. (19)

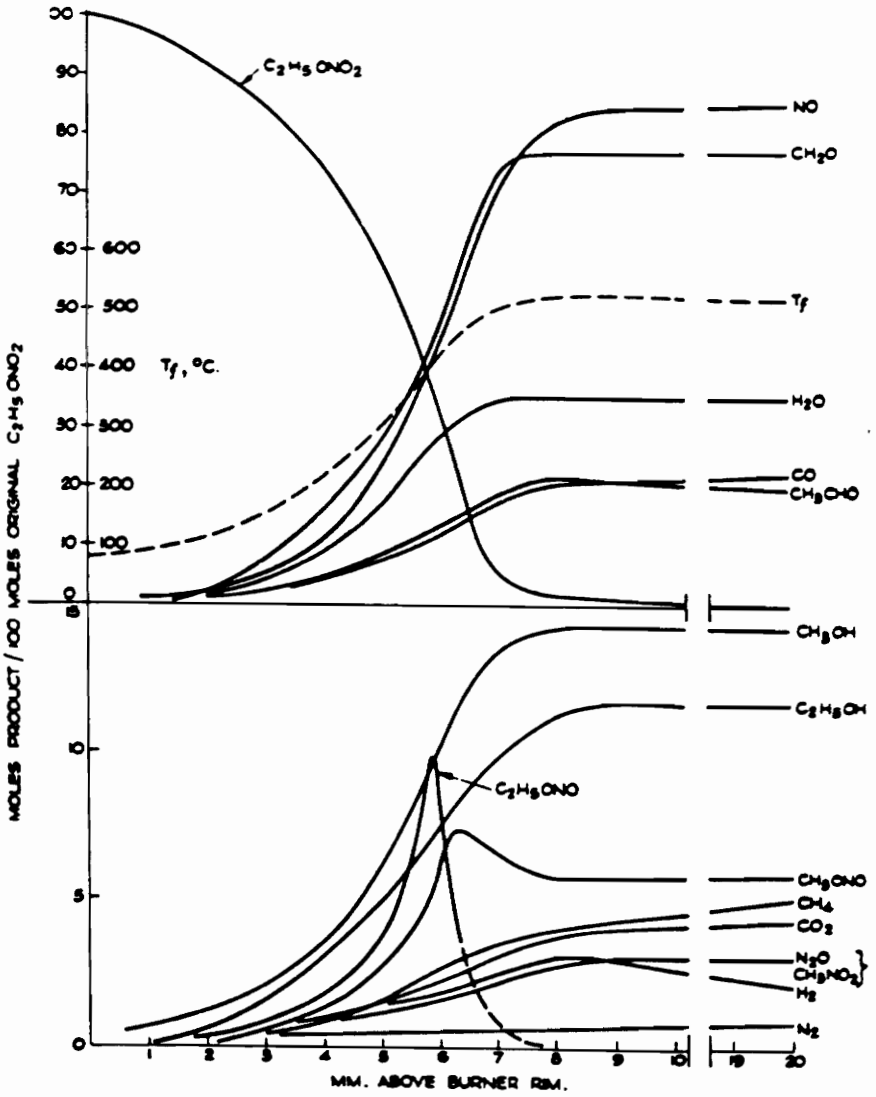

Spatial variation of composition and temperature through ethyl nitrate flame at 35 mm Hg.

Figure 85. Spatial Variation Of Composition And Temperature Through Ethyl Nitrate Flame At 35 mm Hg Ref. (20)

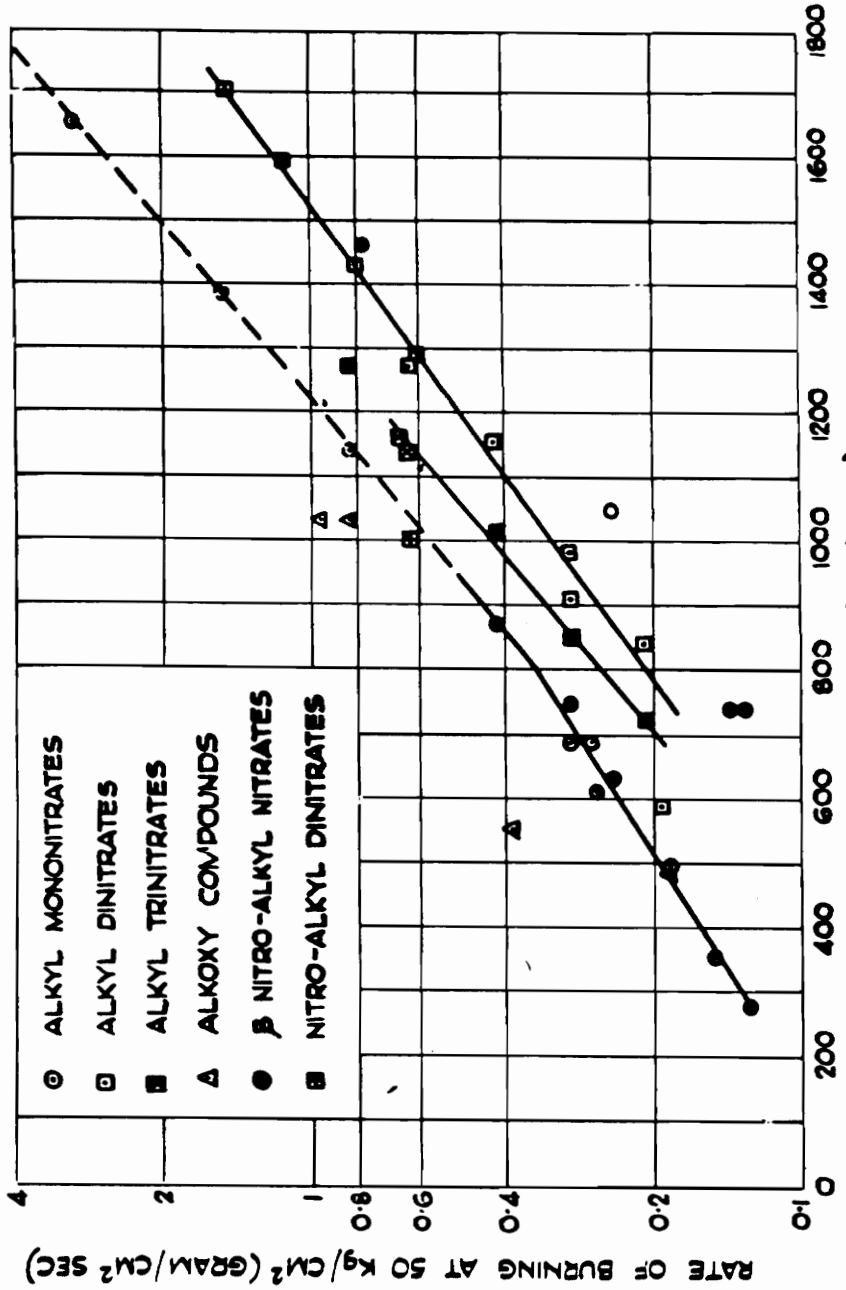

Burning rate at 50 kg/cm² for nitrate esters as a function of calorimetric value.

Figure 86. Burning Rate At 50 kg/cm^2 For Nitrate Esters As A Function Of Calorimetric Value Ref. (20)

Appendix F

Instrumentation/Hardware

Edison 286 computer: A, B, and C drives

Data Translation board : DT5712-PGL

Relay Card : DT752

3M Ribbon cable : 3426

CRYDOM Electronic Solid State Relay TD1210 120V-10 A

Ignition Coil : Standard 12 volts 197U

Ignition Wire : Standard Metallic Core : 3402

Power Supply :Hewlett Packard 6200 B DC power supply, No.67744

Signal Generator: Hewlett Packard 200 S signal generator, No.325

Spark Plug : RFN16LY

Solenoid Coil : Dayton 120 volts, 50/60 Hz 6X543

Thermocouple Wire : OMEGA Chromel Alumel Type K 0.127 mm

Capacitive Discharge Ignitor : Tiger SST 123172

Solenoid Valve : Dayton 2cm 1A578

Wire : Archer 18-GA (polarized)

Rheostat: General Electric 5748472G130

Drive Motor: General Electric KINEMATIC Direct Current Generator 5CD256G38

Compressor: General Electric Fan Unit 7A5-A1

Experimental Operating Conditions

Barometric Pressure : 28 in Hg= 94847.8 (Pa)

Temperature : 277 (K)

Density : 1.1931 (kg/m^3)

Axial Fluid Velocity Under Experimental Operating Conditions : 25.3 (m/s)

Volumetric Flow Rate : 252 (m^3/min)

Mass Flow Rate : 5 (kg/s)

Compressor Rotor RPM : 2900

Thermocouple : Chromel/Alumel, Type K, 0.127mm diameter,

Thermocouple Response Time : 0.005 (s)

Thermocouple Measurement Error : $\pm$ 2.2 (C) $\pm$ 75%

Time Between Thermocouple Measurements : (on the order of 2 microseconds)

Number Of Thermocouples Measuring : 8

Distortion Pattern Frequency : 1Hz

Regulator Valves Open : 90 Degrees Of A Turn

Appendix G

CALIBRATION

The only instruments used in this experiment, were OMEGA chromel alumel type K thermocouples and a pitot tube with a manometer. Details of this instrumentation are listed in the Appendix E section. Pressure measurements were nondimensionalized with the standard sea level atmospheric pressure. Temperature measurements were nondimensionalized with the ambient temperature. The pitot tube and manometer were issued and calibrated by the Mechanical Engineering Department's Instrument Shop. The manometer contained a gravity fluid of known specific gravity. Thus, velocity and pressure measurements, in the exhaust duct, could be measured with the manometer by using the hydrostatic equation and application of Bernoulli's equation. The thermocouples were read by a computer, the same computer that controlled the solenoid valves. A thermocouple normally requires a cold ice bath for its calibration. The ice bath serves as a known reference temperature for the thermocouple to be calibrated against with a known temperature. The thermocouples, used in this experiment, were read by a computer circuit board. The program, that operated the thermocouples, contained line statements to input information about the thermocouple that was being used. This information told the computer the two different metals that composed the thermocouple. This information allowed the computer to automatically calibrate the thermocouples as they read temperatures. The circuitry, on the circuit board, functioned as an electronic ice bath. Therefore, the temperatures displayed on the monitor screen were actual temperatures. This set up was checked and verified with actual thermometers. The response time of the thermocouples was not instantaneous. There is a response time or "time lag" associated with the thermocouples. Therefore, the temperatures read by the thermocouples may

actually be higher. The smaller the diameter of the wire being used for the thermocouple, the smaller the time lag. The time constant for the thermocouple wire used in this experiment was known from the thermocouple manufacturer's handbook. This time constant was used in a first order time lag equation to adjust the data to account for the response time. The first derivative of temperature with respect to time was evaluated using a second order central difference approximation to the first derivative. However, the adjustments made were small and within the error limits of the thermocouples being used. The adjustments were small because the time constant of the thermocouples was small. Examination of the data indicates that the peaks of all the plots appear to be flat. This is a good indication that the steady state temperature was achieved for a small time step during the cycle.

XXI. VITA

The author, Anthony L. DiPietro Jr., was born on September 7, 1968 in Salem Massachusetts. He attended Herndon High School and graduated with honors in June of 1986. Entering Virginia Polytechnic Institute and State University in the fall of 1986, he graduated with a Bachelor of Science Degree in Aerospace Engineering in May of 1991. He began graduate studies at Virginia Polytechnic Institute and State University in the fall of 1991 enrolled in the Master of Science program in Aerospace Engineering. He plans to graduate in the spring of 1993 and attend graduate school in the fall of 1993 to pursue a Doctorate Degree.

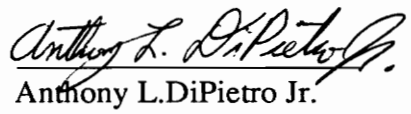

Anthony L.DiPietro Jr.